

University of Alberta

**ENGINEERED NANOSTRUCTURED THIN FILMS FOR ENHANCED
SURFACE ACOUSTIC WAVE SENSORS**

by

Jonathan Kwok Wah Kwan

A thesis submitted to the Faculty of Graduate Studies and Research
in partial fulfillment of the requirements for the degree of

Doctor of Philosophy

in

Microsystems and Nanodevices

Department of Electrical and Computer Engineering

©Jonathan Kwok Wah Kwan

Spring 2013

Edmonton, Alberta

Permission is hereby granted to the University of Alberta Libraries to reproduce single copies of this thesis and to lend or sell such copies for private, scholarly or scientific research purposes only. Where the thesis is converted to, or otherwise made available in digital form, the University of Alberta will advise potential users of the thesis of these terms.

The author reserves all other publication and other rights in association with the copyright in the thesis and, except as herein before provided, neither the thesis nor any substantial portion thereof may be printed or otherwise reproduced in any material form whatsoever without the author's prior written permission.

Dedicated to my parents.

Abstract

Sensor technologies profoundly impact all aspects of our everyday lives. Advances have led to smaller devices, faster response times, reduced costs, higher specificity and sensitivity, and even new sensing technologies. Surface acoustic wave (SAW) technology, which has been around for many decades already, is an example of a newer sensing technology that has begun to be studied for sensing applications. Many advantages of SAW sensors have been identified, in particular the high sensitivity, low cost and wireless capability. However, as the technology is still in its infancy for sensing applications, many improvements and refinements on the platform have yet to be explored.

With the arrival of nanotechnology, many existing technologies have benefited from integrating with the new findings that nanotechnology has brought forth. This thesis investigates the enhancement of existing SAW sensors using nanostructured films fabricated by a thin film deposition process known as glancing angle deposition (GLAD). The GLAD technique is a highly flexible and precise thin film fabrication method that is able to create high-surface-area thin films. This high-surface-area characteristic of these films is the driving motivation in their utilization to enhance the performance of SAW sensors.

This thesis first demonstrates that dense, extremely high surface area films can be deposited on SAW sensors without adversely affecting device perfor-

mance. These modified sensors were then studied as humidity sensors to demonstrate improved sensitivity with the addition of the GLAD films. Before the sensors with GLAD films could be tested in a liquid environment, ion-milling was investigated as a method of eliminating the clustering of the individual structures typically seen after exposure to liquids. These modified films were extended for use on the SAW sensors to investigate liquid sensing performance. The performance of SAW devices with clustered films was also studied for comparison. Both types of films were shown to increase sensitivity greatly over the reference SAW device. The success of these results validates the ability of GLAD films to enhance the sensitivity of not only SAW devices, but potentially other sensing technologies as well.

Acknowledgements

I owe a great amount of thanks to my parents who have supported me throughout my entire time at the U of A, and especially during my grad studies. Without their support it would have been very difficult to achieve all this. I am truly thankful for having such great parents. Thank you to my sister for always encouraging me, as well as My Tran for pushing me through the last stages of this degree.

Thank you to Dr. Jeremy Sit for taking me on as a grad student, as well as supporting and putting up with me all these years. It took a little longer than we would like for me to graduate, but I finally made it! I would also like to extend thanks to Dr. Michael Brett who has also been a huge help with getting me to this point. Thank you to all the post docs who have helped me along the way as well, in particular Mike Taschuk, Mike Flesichauer, Nathan Gerein, Jeff Huang, and Jane Wang. I can't tell you how much I appreciate the help, advice and support given over the years.

I would also like to give a big thanks to all the GLAD group members who have helped me throughout the years. I'm not going to name everyone just because I don't want to forget anyone, but you know who you are!

Thanks to the Nanofab staff, machine shop staff, George Braybrook, Deann Rollings, and the people at ACSES who have helped me with characterization, fabrication and equipment support. I greatly appreciate the effort put into helping me get things I needed ASAP.

Thanks also to those who have helped me immensely with the SAW stuff: Kent Pfeifer, Wei-Shan Wang, Michael Newton, and Glen McHale.

Finally I would like to thank the funding agencies who have supported me through the years: NSERC, ATIF, iCORE.

Contents

1	Introduction	1
1.1	Sensors and Transducers	1
1.1.1	Surface acoustic wave sensors	3
1.2	Glancing angle deposition	5
1.3	Motivation and scope of thesis research	6
2	Background Material	9
2.1	Introduction	9
2.2	Surface acoustic waves	9
2.2.1	Elasticity	9
2.2.2	The piezoelectric effect	12
2.2.3	Acoustic waves	13
2.2.4	Surface acoustic waves	15
2.2.5	Delay-line SAW devices	19
2.2.6	SAW sensors	21
2.3	Glancing angle deposition (GLAD)	24
2.3.1	Physical vapor deposition	24
2.3.2	Glancing angle deposition	27
2.4	Summary	29

3	Experimental methods	31
3.1	Introduction	31
3.2	Design and fabrication of SAW devices	32
3.2.1	SAW substrates	32
3.2.2	IDT design	33
3.2.3	Fabrication details	35
3.2.4	Waveguide layer	38
3.3	Fabrication of GLAD thin films	40
3.3.1	Deposition systems	40
3.3.2	General deposition method	42
3.4	Sample characterization	43
3.4.1	Film structure	43
3.4.2	SAW device measurement	44
3.5	Summary	48
4	Love wave humidity sensors using nanostructured films grown by GLAD	50
4.1	Introduction	50
4.2	Experimental	52
4.2.1	Film fabrication	52
4.2.2	SAW measurement setup	53
4.3	Results and discussion	56
4.4	Summary	68
5	Development of GLAD nanostructures suitable for use in liq- uid environments	70
5.1	Introduction	70

5.2	Fourier transform image analysis	72
5.3	Tailoring the chemistry of surfaces	73
5.4	Experimental	75
5.4.1	Sample fabrication	75
5.4.2	Chemical functionalization	76
5.4.3	Characterization	78
5.5	Results and discussion	80
5.6	Summary	93
6	SAW liquid sensors enhanced with GLAD films	94
6.1	Introduction	94
6.2	Experimental	96
6.2.1	Film preparation	96
6.2.2	Measurement setup	97
6.3	Results and discussion	98
6.4	Summary	110
7	Conclusion	112
7.1	Concluding remarks	112
7.2	Future work	116
7.3	Final remarks	118
	Bibliography	118

List of Tables

4.1	Fit parameters for data set from Fig. 4.8, following the fit $a_1x + a_3x^3 + a_5x^5$. The frequency unit used in the fit is MHz and the RH is expressed as a fraction rather than a percentage. Reprinted from [95] with permission from Elsevier.	63
4.2	Response times for the adsorption and desorption of humidity of SAW devices with GLAD films.	67

List of Figures

1.1	Schematic drawing of a SAW sensor. An input oscillating electric field is applied at the input to create a surface acoustic wave, which propagates along the device and is altered by the adsorbed mass. The wave is then reconverted into an electric field for measurement at the output.	4
2.1	Uniformly stretched bar by an applied force in the x-direction.	10
2.2	Arbitrary coordinate axes for SAW analysis. The sagittal plane shown is defined by the x_1 and x_3 axes.	16
2.3	Schematic examples of the displacement of particle elements for: a) Rayleigh wave and b) Love wave. Arrows show the direction of wave propagation. The triangular shape of the Love wave is a result of the large particle sizes used to depict it. Reprinted from [25] with permission from Wiley.	17
2.4	Schematic representation of a two port delay-line SAW device.	19
2.5	IDT consisting of an infinite number of electrodes with alternating impulses of magnitude V	20

2.6	A schematic of film growth at an oblique angle α . (a) As nucleation sites grow in size, they begin to block the region directly behind them from the incident vapor flux. These shadowed regions have no film growth. (b) As the deposition proceeds, only the exposed nuclei continue to grow by capturing the incoming vapor atoms, and develop into columns tilted towards the incident flux at an angle β	27
2.7	Examples of structures fabricated with GLAD using SiO ₂ : a) slanted posts, b) chevrons, c) helices.	29
3.1	Schematic of a) a solid-electrode IDT and b) a split-electrode IDT with finger width d , spacing w , and aperture a	34
3.2	Optical mask used to fabricate SAW devices. The red outline shows the parallelogram shape of a device after dicing.	36
3.3	Process flow for SAW device fabrication showing the deposition of metals (step 2), photolithography (steps 3-5), and metal etching (step 6).	37
3.4	Deposition chamber.	41
3.5	Schematic of a fully fabricated Love wave SAW device with a deposited GLAD thin film.	43
3.6	Fabricated sample holder for SAW devices. a) Top-down and b) bottom-up views.	44
3.7	The a) insertion loss and b) phase response of a typical Love wave SAW device used in this research.	46
3.8	General circuit for a SAW device in an oscillator configuration.	47

3.9	Oscillation circuit and its components used for SAW device testing.	48
4.1	a) Cross-sectional and b) top-down SEM images of a 450 nm thick SiO ₂ GLAD film with a 30 nm solid underlayer. Scale bar is applicable to both a) and b). Reprinted from [95] with permission from Elsevier.	53
4.2	a), b) Cross-sectional and c), d) top-down SEM images of 210 nm and 590 nm thick, respectively, SiO ₂ GLAD film with a 30 nm solid underlayer. Scale bar is applicable to all images.	54
4.3	The a) insertion loss and b) phase response of a device before and after a 210 nm thick GLAD film has been deposited on top.	57
4.4	Relationship between GLAD film thickness and shift in the operating frequency, as-deposited and after 24 h. Reprinted from [95] with permission from Elsevier.	58
4.5	Relationship between GLAD film thickness and insertion loss, as-deposited and after 24 h. Reprinted from [95] with permission from Elsevier.	58
4.6	Time-resolved response of GLAD-modified SAW sensors to increasing relative humidity loadings of 9.8%, 19.3%, 28.6%, 38.6%, and 48.3%.	60
4.7	Examples of adsorption and desorption curve fitting on the time-resolved frequency data for the SAW device with a 450 nm GLAD film.	61
4.8	Response of GLAD-modified SAW sensors to relative humidity loading. Reprinted from [95] with permission from Elsevier.	62

4.9	Sensitivity curves of SAW sensors to RH with varying thicknesses of GLAD films. Reprinted from [95] with permission from Elsevier.	63
4.10	Examples of sensitivities with respect to film thickness for different relative humidity loadings, showing the non-linear relation. The lines are exponential fits to the data.	64
4.11	Response to humidity of a device with 590 nm GLAD on a thin layer of PMMA and that with no GLAD and a thick layer of PMMA. Both devices operate at about the same frequency. Reprinted from [95] with permission from Elsevier.	65
4.12	Long term stability of a device with 500 nm GLAD stored in open air over 21 days. Reprinted from [95] with permission from Elsevier.	68
5.1	Common SAM precursor molecules. a) octadecyltrichlorosilane b) 3-aminopropyltrimethoxysilane c) tridecafluoro-1,1,2,2-tetrahydrooctyltrichlorosilane	75
5.2	SEM images of a) an unmodified GLAD film and b) GLAD film solution-phase functionalized with APS	77
5.3	Cross-sectional (first column) and top-down SEM images of 1600 nm films before water treatment (second column), and after water treatment (third column). Scale bars are applicable to their respective views. Reproduced from [124] with permission from IOP Publishing Ltd.	81

5.4	Cross-sectional SEM images of a 550 nm film (a) before ion-milling and (b) after 0.5 min of ion-milling. Reproduced from [124] with permission from IOP Publishing Ltd.	82
5.5	An example of a) a top-down SEM image of one of the GLAD films, b) its Fourier transform, and c) the radial average of the Fourier intensity profile. Reproduced from [124] with permission from IOP Publishing Ltd.	84
5.6	Plot of the change in dominant spacing after water treatment as a function of ion-milling time for films of varying thicknesses, as extracted from Fourier transform analysis of the top-down SEM images. Data points are from the experiment, with error bars showing 1σ values. (Note that error bars are smaller than datapoint symbols for 900 nm and 550 nm film sets for ion milling times ≥ 0.5 min.) Solid lines are a decaying exponential fit to the data (detailed in text). Reproduced from [124] with permission from IOP Publishing Ltd.	86
5.7	Plot of decay constant τ <i>vs.</i> measured film thickness h . Data points (and error bars) are τ values (and 1σ uncertainties) obtained from curve fits from Fig. 5.6. Solid line is linear best-fit to the data. Reproduced from [124] with permission from IOP Publishing Ltd.	87
5.8	Sketch of the inverted frustrum in a singly-clamped cantilever configuration.	88
5.9	XPS survey spectrum of an unmodified and APS-functionalized ion-milled GLAD film	91

5.10	a) unmodified ion-milled film and b) APS-functionalized film after 24 h in a AuNP solution	91
5.11	SEM images showing the transition from the unmasked region to the masked region of a functionalized GLAD film in a UV/ozone cleaner, followed by AuNP immobilization.	92
6.1	SEM images of (a) an as deposited GLAD film, followed by (b) ion-milling, or (c) clustering. (d) is a top-down SEM image of (c). Scale bar is applicable to all images. Reproduced from [156] with permission from Elsevier.	97
6.2	Relationship between GLAD film thickness and insertion loss, as-deposited, after ion-milling, and after clustering. Error bars are the standard deviations of the changes over several devices. Reproduced from [156] with permission from Elsevier.	99
6.3	Relationship between GLAD film thickness and frequency shift, as deposited, after ion-milling, and after clustering. Error bars are the standard deviations of the shifts over several devices. Linear fits are shown for the ion-milled and clustered films. Re- produced from [156] with permission from Elsevier.	100
6.4	Frequency response of a Love-wave device with an ion-milled film to varying glycerol-water mixtures exchanged over the sur- face: 5.0, 10.0, 15.4, 20.0, 25.6, 32.9, 37.3, 42.3, 46.7 %. . . .	101
6.5	Frequency response of a Love wave device to increasing viscos- ity of glycerol/water mixtures exchanged over the surface, then reversing the order: 15.4, 25.6, 32.9, 37.3, 42.3, 46.7%.	103

6.6	Baseline frequency values for successive viscous loadings in Fig. 6.5.	
		103
6.7	Frequency response of a Love wave device to decreasing viscosity of glycerol/water mixtures exchanged over the surface, then reversing the order: 46.7, 42.3, 37.3, 32.9, 25.6, 15.4 %.	104
6.8	Baseline frequency values for successive viscous loadings in Fig. 6.7.	
		104
6.9	Frequency reponse of a Love wave device to the several loadings of the same glycerol/water mixture.	106
6.10	Frequency shifts with respect to the square root of density-viscosity product for varying thicknesses of GLAD thin films, with fits for each data set. Reproduced from [156] with permission from Elsevier.	107
6.11	Sensitivity curves with respect to $(\rho\eta)^{1/2}$ for devices with varying GLAD film thicknesses. The curve for the 350 nm clustered film is truncated past $(\rho\eta)^{1/2} = 1.6$ beacuse there was no data collected for these values of $(\rho\eta)^{1/2}$. Points for each curve are included for clarity. Reproduced from [156] with permission from Elsevier.	109

List of Symbols and Abbreviations

Symbols

α	Wave attenuation; deposition angle
a	Aperture
A	Area
$\Delta\mathbf{A}$	Differential area vector
β	Wave number of surface wave; column tilt angle
c	Device-dependent factor
c_{ijkl}	Elastic stiffness tensor
δ	Inter-pillar distance
d	Distance between successive electrodes
D	Diameter of nanostructure
\mathbf{D}	Electric displacement vector
ΔDS	Change in dominant spacing
e_{kij}	Piezoelectric tensor
ε_{ik}	Permittivity tensor
E	Young's modulus
\mathbf{E}	Electric field vector
f	Frequency
f_0	Fundamental frequency of SAW device
F_c	Capillary force
$\Delta\mathbf{F}$	Differential force vector
γ	Complex propagation factor; surface tension
k	Wave vector
k_0	Fundamental wave number

K^2	Electromechanical coupling coefficient
λ	Acoustic wavelength
h	Film thickness
m	Mass
η	Viscosity; metallization ratio
η_c	Critical viscosity
N	Number of pairs of electrodes
N_l	Near-field length
ρ	Material density
r_1	Radius at bottom of nanostructure
r_2	Radius at top of nanostructure
ϕ	Substrate rotation axis, normal to substrate
Φ	Electric potential
θ	Contact angle
S_{ij}	Strain tensor
τ	Clustering decay constant
t	Time
t_{im}	Ion-milling time
T	Temperature
T_M	Melting point temperature
T_{ij}	Stress tensor
\mathbf{u}	Displacement vector
v	Phase velocity
v_0	Fundamental acoustic wave velocity
ω	Angular frequency
w	Finger width spacing

ξ Power law scaling exponent

Z Surface impedance

Abbreviations

AES Auger electron microscopy

APS 3-aminopropyltrimethoxysilane

AuNP Gold nanoparticle

CTM Crystal thickness monitor

DI Deionized

DS Dominant spacing

FT Fourier transform

FTIR Fourier transform infrared spectroscopy

GLAD Glancing angle deposition

IDT Interdigitated transducer

IL Insertion loss

LoD Limit of detection

NA Network analyzer

PMMA Polymethylmethacrylate

PPM Parts-per-million

PVD Physical vapor deposition

QCM Quartz-crystal microbalance

RF Radio frequency

RH Relative humidity

RIE Reactive ion etching

SAM Self-assembled monolayer

SAW Surface acoustic wave

SCCM	Standard cubic centimeters per minute
SEM	Scanning electron microscope
XPS	X-ray photoelectron spectroscopy
SERS	Surface-enhanced Raman spectroscopy
SH	Shear horizontal
SZM	Structure zone model
SH-APM	Shear horizontal acoustic plate mode
SPR	Surface plasmon resonance
STW	Surface transverse wave
TCD	Temperature coefficient of delay
TSM	Thickness-shear mode
UV	Ultra violet

Chapter 1

Introduction

1.1 Sensors and Transducers

A sensor can be defined as a device that detects a variation in the input energy, and in turn produces a variation in another or the same form of energy [1]. A transducer is then defined as a device that converts the measurand or physical property into a usable signal. Thus, a transducer by definition encompasses a sensor, but not vice versa. However, the two terms are often used interchangeably and for the purposes of this thesis they will be used as such. The original measurand from a sensor is often unusable because it is difficult to quantify and thus impractical for use towards the intended application(s). As a very simple example, a metal bar can be used as a temperature sensor from its expansion/compression resulting from temperature changes, but only after a calibrated scale is placed along the length of the bar to relate it to temperature can the temperature be quantified and used. The signal types that are measured and/or converted can be divided into six categories: mechanical, electrical, thermal, magnetic, radiant and chemical. In the example above, it

would be classified as a conversion from a thermal to a mechanical signal.

Sensors are found in everyday life, from a simple temperature sensor (thermometer), to the complex touch-screen sensors found in phones, cars, *etc.* Arguably one of the more important utilizations of sensors, though, is for health and safety applications. This includes examples such as the acceleration sensors used to trigger airbags in cars, hazardous gas sensors for use in residential housing and industrial sites, and medical diagnostic sensors to detect and quantify the presence of harmful pathogens. The evolution and impact of these sensor technologies is tremendous, enabling a higher level of safety that ultimately saves time, money, and most importantly, lives. For example, one of the earliest forms of a humidity sensor consisted of segments of wool placed on a scale balanced with rocks [2]. As humidity increased, the amount of water absorbed in the wool would increase, thereby increasing its weight, and thus providing a measure of the humidity. Fast forward to the humidity sensors used today and one will find that one of the most precise humidity sensors available is the chilled mirror dewpoint hygrometer, which utilizes a chilled mirror and optoelectronic mechanism to detect condensation on the mirror surface [3], a significant increase in complexity but improvement on accuracy. Advancements in other technologies have also significantly increased the accuracy and reduced the overall size of a variety of sensor types, including accelerometers, pressure sensors, and torque sensors [4]. One of the first commercial accelerometers, for example, was based on a resistance bridge, weighed about a pound, and was 196 cm³ in size [5]. Today, multiple accelerometers based on a capacitive detection can be found in handheld cellular phones, with a size of 0.0038 cm³ and weight of no more than a few grams [6].

With the ever-increasing human population and concerns over public health, there has been much research devoted to developing cheaper, quicker, and more efficient medical and biological sensors. More specifically, the key requirements to achieving these goals are high sensitivity and selectivity. The sensitivity of a sensor can be defined as the level or magnitude of the measured output in response to a given input, while the selectivity of a sensor is defined as the ability to distinguish between two or more inputs. The increasing demand for increased sensitivity and selectivity in microarray technology, for example, has led to the further development of surface chemistry, labeling strategies, and detection methods [7]. These studies have been extended to other sensor technologies such as surface-enhanced Raman spectroscopy (SERS) [8], surface plasmon resonance (SPR) [9], and surface acoustic waves (SAWs) [10]. A closely related concept to sensitivity is the limit of detection (LoD), which is the minimum quantity or concentration of an analyte that can be reliably measured. The LoD is just as important when developing a sensor, particularly in the medical field, where the initial detection of a particular pathogen can be crucial to quickly taking the necessary counter-measures to prevent spreading.

1.1.1 Surface acoustic wave sensors

An area that has become increasingly studied in the sensor field, and the focus of this thesis, is surface acoustic wave (SAW) technology [11]. SAW devices have been in use in the telecommunication industry for over sixty years in electronic devices, such as signal filters [12], and began to emerge as a major sensor platform in the past three decades [10–12]. As the name suggests, SAW sensors utilize an acoustic wave that is confined to the surface of the sensor as the sensing mechanism. When a perturbation occurs at the surface, this will

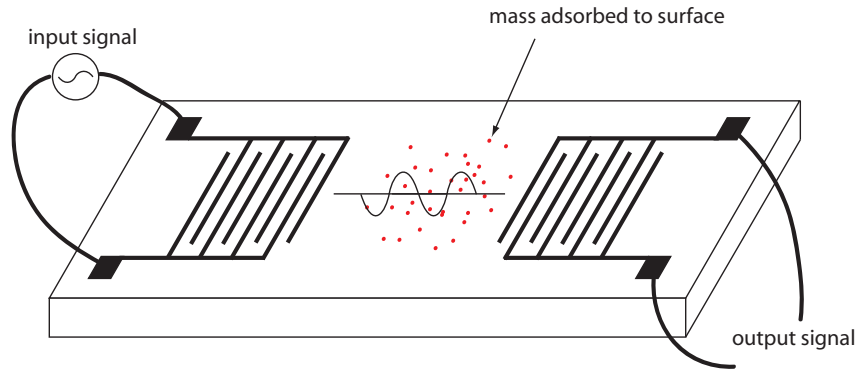


Figure 1.1: Schematic drawing of a SAW sensor. An input oscillating electric field is applied at the input to create a surface acoustic wave, which propagates along the device and is altered by the adsorbed mass. The wave is then reconverted into an electric field for measurement at the output.

affect the velocity and/or amplitude of the SAW, which can then be measured, quantified and related back to the perturbation. This is similar to thickness-shear mode (TSM) devices, where waves that are in the bulk of the material are used to detect changes at the surface. Common perturbations include mass adsorption on the surface (mass-loading), variations in viscosity, and changes in conductivity. Because of the surface nature of the acoustic wave, it is very sensitive to these perturbations and hence the motivation to develop this as a sensor platform. In addition to the high sensitivities, another key advantage of SAW sensors is their ability to function wirelessly by directly connecting the device to an antenna, which can be accessed by a radio frequency (RF) signal. A schematic of a common SAW sensor is shown in Fig. 1.1.

SAW devices were first demonstrated as a gas sensor in 1979 [13]. Since then, a wide range of SAW chemical sensors have been studied, and there has been a shift toward studying SAW sensors operating in liquid environments as well. In all cases, attempts to increase sensitivity have been a major theme. Various types of SAW sensors have been developed to further confine the acous-

tic wave energy to the surface of the device to increase sensitivity. Examples of such devices include using a very thin substrate (flexural plate wave devices) or a waveguide layer (Love wave devices). Aside from maximizing the trapped acoustic energy at the surface, increasing the surface area of the active area of the device can also increase the sensitivity by increasing the amount of mass adsorbed to the surface or the interaction between the surface and the exposed medium. This can be achieved by using nanostructured coatings on the active area of the SAW devices [14]. Structures on this scale typically have at least one feature in the range of one to one hundred nanometres. As the characteristic dimensions of a structure decreases, the surface area-to-volume ratio significantly increases. At the nanometre scale, key consequences of this are that the structural and material properties (*e.g.*, electrical and optical) begin to differ from their macroscopic counterparts. The surface area gain at such a small volume cost makes nanostructures extremely attractive for coupling with SAW sensors to increase sensitivity and LoD, as those of current SAW sensors may not be adequate for many bio-detection experiments [14]. The addition of nanostructures onto SAW devices would also provide the increase in surface area with essentially no sacrifice in sensor size. The challenges, then, become developing suitable nanostructures for the intended sensing application, and the corresponding process for integrating the nanostructures with the SAW sensor.

1.2 Glancing angle deposition

Glancing angle deposition (GLAD) is a powerful physical vapor deposition (PVD) technique for fabricating nanostructured thin films. GLAD allows for

the precise control of film morphology and density, resulting in the fabrication of a diverse range of different nanostructures. The GLAD process will be described in detail in Chapter 2. GLAD, being a PVD technique, can use a wide range of materials, including metals (*e.g.*, Cu, Ti, Al, Co), dielectrics (*e.g.*, SiO₂, TiO₂, CaF₂), semiconductors (*e.g.*, Si, Ge) and organics (*e.g.*, Alq₃, CuPc, C₆₀) [15]. The high surface area and porosity of GLAD thin films, combined with the flexibility of the GLAD technique make it promising for applications in sensor technology, and in particular with SAW sensors.

1.3 Motivation and scope of thesis research

The main objective of this thesis is to engineer GLAD-enhanced SAW sensors. The integration of nanostructures, in general, with SAW technology is still quite new and not well studied. In the case of GLAD, there have been no studies to demonstrate its viability for enhancing SAW sensors. Realizing this objective will not only further demonstrate the versatility of GLAD in sensor applications, but also the capabilities of SAW sensors. This will hopefully encourage further development of SAW sensors towards commercialization for more widespread, affordable sensors and diagnostic tools to increase the standard of living across the globe.

Following this introductory chapter, Chapter 2 provides important background material pertaining to this thesis research. The principles of thin film deposition, GLAD fabrication, and the key changes when transitioning to GLAD are discussed in detail. An overview of the theory and working principles of SAW devices is provided.

Chapter 3 presents the general experimental methods used in this thesis.

The design and fabrication processes for the SAW devices are presented in detail, as well as the general procedures for fabricating GLAD films. This is followed by a discussion of the characterization tools that were employed.

Chapter 4 describes the first integration of GLAD films with SAW sensors. Dense, high surface area films of varying thickness are grown and their effects on the response of the SAW devices is examined. The enhanced sensitivity of these devices to humidity is also studied and compared to other SAW humidity sensors.

When GLAD structures are exposed to liquids, they have been known to deform or cluster together due to capillary forces from the liquid acting on them [16–21]. This is a potentially serious problem for sensing applications involving liquid environments as the clustering destroys the ordered structure of the film and reduces the accessible surface area. Chapter 5 examines the use of ion-milling on vertical post nanostructures grown by GLAD to eliminate the clustering effect. The effects of ion-milling on the structure and morphology of the vertical posts and their relation to the clustering is investigated. It is shown that ion-milling does not significantly impact the porosity and accessible surface area of the nanostructures while simultaneously strengthening the nanostructures and reducing the capillary forces acting on them. Tailoring the surface chemistry of these films is also demonstrated.

Chapter 6 investigates the use of highly porous, well separated nanostructures grown by GLAD on liquid SAW sensors. The work in the previous chapter is directly applied here to enable use of these structures in a liquid environment. The effect of ion-milled films and clustered films on device response is examined, and the device performance is investigated by viscous loading. It is shown that sensitivity increases with film thickness at the cost of an increase

in signal loss, thus requiring an optimum balance between the two based on the application.

Chapter 7 summarizes and concludes the work completed in this thesis. Future directions for this research are also suggested.

Chapter 2

Background Material

2.1 Introduction

The work in this thesis revolves around two main subjects: SAW sensors and GLAD thin films. This chapter provides background material on both these subjects needed to understand, analyze and interpret the research. A brief review of acoustic waves will be followed by a transition into a discussion about SAW devices. Basic operating principles of SAW devices will also be explored, with emphasis on the type of SAW device used in this research. Similarly, a review of thin film growth and PVD will be discussed, transitioning into the methodology of GLAD.

2.2 Surface acoustic waves

2.2.1 Elasticity

This section provides a general introduction to elasticity; interested readers are invited to consult references [22, 23].

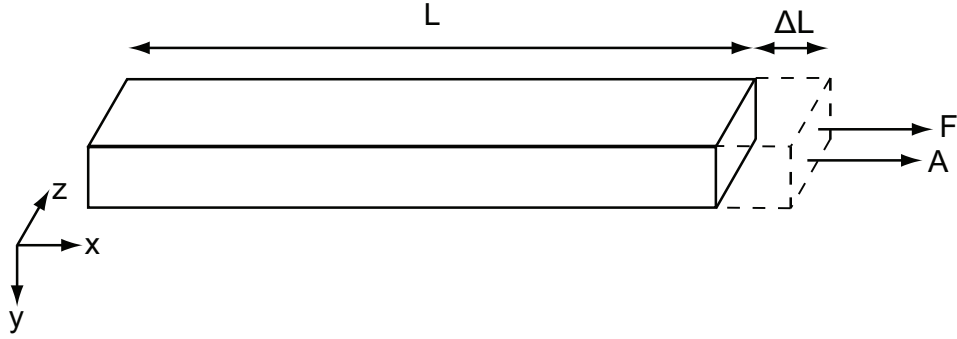


Figure 2.1: Uniformly stretched bar by an applied force in the x-direction.

In a solid, an acoustic wave involves the displacement of atoms from their equilibrium positions. These displacements are described by the strain tensor. Consider a particle that is located at point $\mathbf{x} = (x_1, x_2, x_3)$ at equilibrium. The term “particle” is used to define an elementary volume of material that is significantly smaller than other characteristic dimensions (*e.g.*, wavelength), yet larger than interatomic distances. If the particle is displaced by an amount $\mathbf{u} = (u_1, u_2, u_3)$, where the components of \mathbf{u} are functions of the components of \mathbf{x} , then the particle has been displaced to the new position of $\mathbf{x}' = \mathbf{x} + \mathbf{u}$. The components of the strain are then defined as:

$$S_{ij} = \frac{1}{2} \left(\frac{\partial u_i}{\partial x_j} + \frac{\partial u_j}{\partial x_i} \right), \quad (2.1)$$

where $i, j = 1, 2, 3$ ¹. This equation removes the non-zero strain when the material is rotated or displaced as a whole. The strain is a second-rank tensor and symmetrical so that $S_{ij} = S_{ji}$, and thus only six of the nine components are independent. In a simple example, consider the uniformly stretched bar in Fig. 2.1 with a Poisson’s ratio of zero. Because the only displacement is along the x -direction, and the bar is uniformly stretched, then $u_y, u_z = 0$ and

¹This permutation of the indices will be assumed from here on out unless otherwise stated. For example, if a reference is made to F_i , then it is referring to all components F_i , $i = 1, 2, 3$.

$\frac{\partial}{\partial y}, \frac{\partial}{\partial z} = 0$. So the only strain is $S_{xx} = \partial u_x / \partial x$.

When the particle in a material is displaced, internal forces that tend to return the particle back to equilibrium are produced. These forces are described by stress, which is defined as the force exerted per a unit area. Consider a small surface area $\Delta \mathbf{A}$ in a solid, with directional components ΔA_j with respect to the orthonormal reference frame, which is subjected to a force $\Delta \mathbf{F}$, with components ΔF_i . Like strain, stress is also a second rank tensor, and its components are defined as:

$$T_{ij} = \frac{\Delta F_i}{\Delta A_j}. \quad (2.2)$$

In other words, component T_{ij} is the i -th component of the force exerted on the surface element perpendicular to the j -axis. The stress tensor is also symmetrical so that $T_{ij} = T_{ji}$. Going back to the bar in Fig. 2.1, if a small section of the bar is considered (of differential thickness), then the force is equal and opposite in direction on each side of the section since the bar is not moving. Also, because the force is only applied along the x -direction, on the area that is also in the same direction, then the only stress present is $T_{xx} = F_x / A_x = F / A$. Stresses where the force and area are in the same directions (subscripts are the same) are of interest in compressional waves, which will be described later.

A material is considered elastic if it returns to its initial state after all external forces are removed. As noted above, these returning forces are due to internal stresses. In non-piezoelectric materials, and for small deformations, the stress and strain are directly proportional according to Hooke's Law:

$$T_{ij} = c_{ijkl}S_{kl}, \quad (2.3)$$

where c_{ijkl} is the elastic stiffness tensor, a fourth rank tensor. While this tensor has 81 components, the number of independent components is significantly reduced because of the symmetries of the stress and strain tensors. It can also be shown that thermodynamic considerations impose another degree of symmetry, where $c_{ijkl} = c_{klij}$, further reducing the number of independent components. Thus, the stiffness tensor has at most 21 independent components, with further reductions when taking into account the crystal symmetries of a material. For example, the tensor components of an isotropic material can be fully described by two coefficients.

2.2.2 The piezoelectric effect

The direct piezoelectric effect was first discovered by Pierre and Jacques Curie in 1880, and occurs when a mechanical strain in a crystal produces an electric polarization, which is proportional to the strain and of opposite sign [24]. The converse piezoelectric effect was later confirmed, whereby an applied electric field causes the crystal to undergo a proportional strain. The piezoelectric effect is specific to only certain crystalline materials, with the minimum requirement of the crystal being a lack of centre of symmetry. Of the 32 crystal classes, 21 classes have no centre of symmetry and of those 20 are piezoelectric. Furthermore, the piezoelectric effect is only exhibited along certain directions relative to the crystal axes, with the number of directions increasing with asymmetry. Some of the more common piezoelectric materials include quartz, lithium niobate, lithium tantalate, and gallium arsenide.

In piezoelectric materials, the stress-strain relationship in Eq. 2.3 no longer holds when an electric field is present. The coupling between electrical and mechanical parameters must be accounted for, and this is reflected in the stress-strain relationship and the electrical displacement and field relationship as in Eq. 2.4 and 2.5 respectively, where the last term on the right side of each equation has a piezoelectric term introduced [25].

$$T_{ij} = c_{ijkl}^E S_{kl} - e_{kij} E_k \quad (2.4)$$

$$D_i = \varepsilon_{ik}^S E_k + e_{ikl} S_{kl} \quad (2.5)$$

Here, e is the piezoelectric tensor, c is the elastic stiffness tensor at constant electric field E , ε is the permittivity tensor at constant strain S , and E is the electric field. It can also be shown that the electromechanical coupling coefficient K^2 can be defined by [26]

$$K^2 = \frac{e^2}{c\varepsilon}. \quad (2.6)$$

K^2 , often expressed as a percentage, is a measure of the efficiency of the piezoelectric material in converting between electrical and mechanical energy. The higher the value, the higher the coupling of energy from the electrical domain to the mechanical domain and *vice versa*.

2.2.3 Acoustic waves

Acoustic wave modes can be described by the particle displacement relative to the direction of wave propagation. Longitudinal (or compressional) waves

have particle displacements parallel to the direction of propagation whereas transverse waves are orthogonal to the direction of propagation. To describe the propagation of waves in elastic materials, an equation of motion is used by taking the stress and strain to be functions of time in addition to position. For a material with density ρ , the equation of motion is written as:

$$\rho \frac{\partial^2 u_i}{\partial t^2} = \frac{\partial T_{ij}}{\partial x_j}, \quad (2.7)$$

which is valid for both non-piezoelectric and piezoelectric materials. For piezoelectric materials, the electric field can be expressed as a function of the electric potential, Φ , using a quasi-static approximation:

$$E_k = -\frac{\partial \Phi}{\partial x_k}, \quad (2.8)$$

because the elastic waves move much more slowly than the electrical ones. Furthermore, if the material is taken to be an insulator (which is most often the case), then $\nabla \mathbf{D} = 0$. Combining these equations yields the following:

$$\rho \frac{\partial^2 u_i}{\partial t^2} = c_{ijkl}^E \frac{\partial^2 u_k}{\partial x_j \partial x_l} + e_{kij} \frac{\partial^2 \Phi}{\partial x_j \partial x_k}, \quad (2.9)$$

$$0 = e_{jkl} \frac{\partial^2 u_l}{\partial x_j \partial x_k} - \varepsilon_{jk}^S \frac{\partial^2 \Phi}{\partial x_j \partial x_k}. \quad (2.10)$$

To solve these equations, solutions of the form,

$$u_l = u_l^0 \exp[j(\omega t - k_l x_l)], \quad (2.11)$$

$$\Phi_l = \Phi_0 \exp[j(\omega t - k_l x_l)], \quad (2.12)$$

are assumed and substituted into Eqs. 2.9 and 2.10, yielding four equations in the four variables u_l^0 and Φ_0 . Here, ω is the angular frequency and k_l is the wave vector. In general, the solutions yield three waves propagating in the same direction with different velocities and mutually orthogonal displacement vectors (polarizations) [22]. The polarization is generally also not directly parallel or orthogonal to the propagation direction. Thus, the wave which has a displacement vector closest to the propagation direction is called the quasi-longitudinal wave, while the other two are quasi-transverse waves. However, there are propagation directions relative to the crystal lattice that allow for the polarizations to be purely longitudinal or transverse.

2.2.4 Surface acoustic waves

Consider now, a piezoelectric solid in a half-space (Fig. 2.2), where vacuum exists in the space $x_3 > 0$ and the piezoelectric solid occupies the space $x_3 < 0$. The surface-propagating wave is assumed to be directed along x_1 , and the plane defined by the surface normal and wave vector is known as the sagittal plane. To obtain the wave solutions, boundary conditions must now also be satisfied in addition to solving the equation of motion. In general, the solutions take the form of:

$$u_l = u_l^0 \exp(j\gamma x_3) \exp[j(\omega t - \beta x_l)], \quad (2.13)$$

$$\Phi_l = \Phi_o \exp(j\gamma x_3) \exp[j(\omega t - \beta x_l)], \quad (2.14)$$

where γ is generally a complex quantity and β is the wave number of the surface wave. For an isotropic, non-piezoelectric solid, the only condition im-

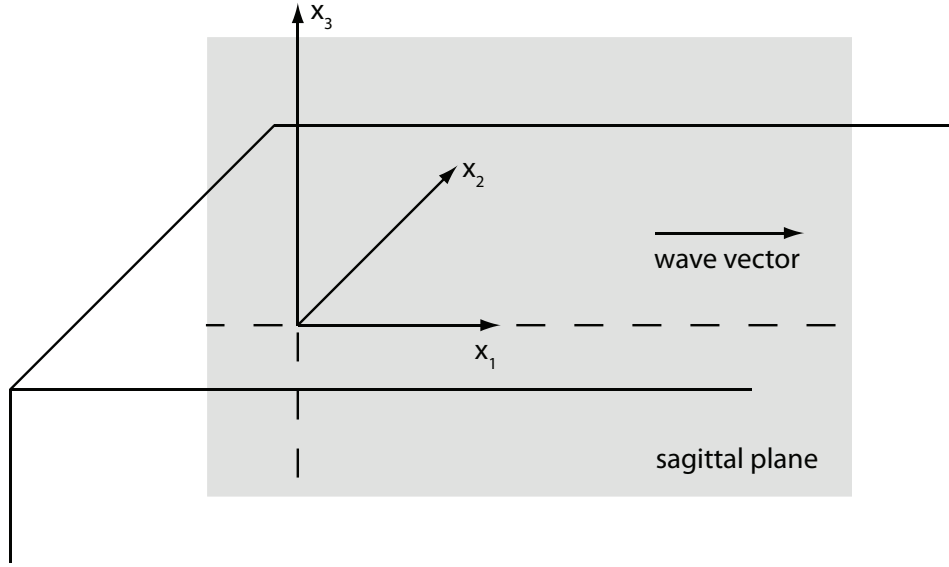


Figure 2.2: Arbitrary coordinate axes for SAW analysis. The sagittal plane shown is defined by the x_1 and x_3 axes.

posed is that there can be no traction forces on the free surface at $x_3 = 0$, or in terms of stress, this means that $T_{i3} = 0$ at $x_3 = 0$. In the piezoelectric case, the electrical boundary conditions must be considered as well. Crystal symmetry for anisotropic materials place further constraints on the wave solutions, so the solutions become increasingly difficult to come by and thus require approximations and numerical methods.

The most common type of SAW is the Rayleigh wave, named after Lord Rayleigh who first discovered it [27]. In isotropic materials, Rayleigh waves have a longitudinal and transverse component, which are both contained in the sagittal plane. With piezoelectricity and anisotropy, the solutions are more complex and results in what is known as the piezoelectric Rayleigh wave, which is still similar to a Rayleigh wave for isotropic materials. The penetration depth is typically on the order of a wavelength. Thus, most of the energy of the wave is confined to the surface of the material, making it very sensitive

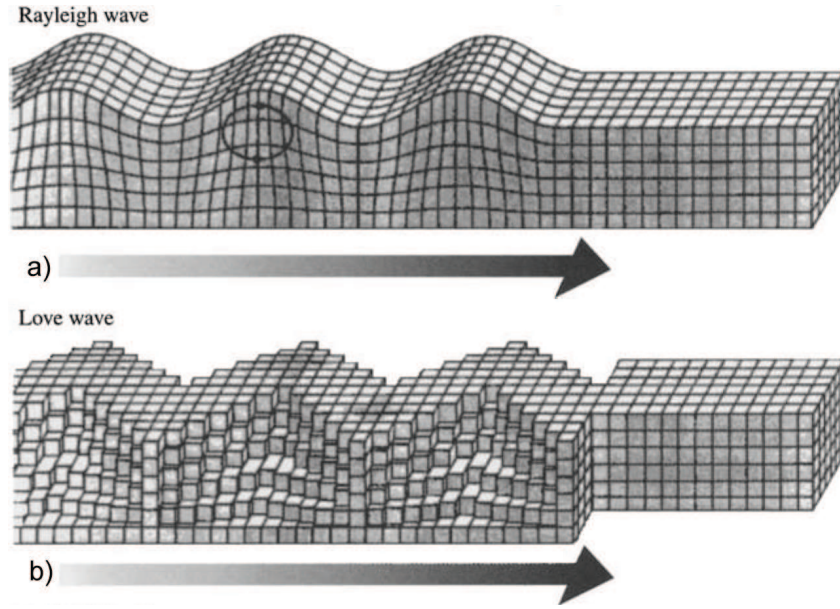


Figure 2.3: Schematic examples of the displacement of particle elements for: a) Rayleigh wave and b) Love wave. Arrows show the direction of wave propagation. The triangular shape of the Love wave is a result of the large particle sizes used to depict it. Reprinted from [25] with permission from Wiley.

to surface perturbations. As an example, Rayleigh waves are commonly produced along the crystallographic X -axis of single crystal quartz. A pictorial representation of a Rayleigh wave is shown in Fig. 2.3a.

Another solution for piezoelectric materials can also exist, called the Bleustein-Gulyaev wave [28, 29]. The existence of this wave occurs when the sagittal plane is normal to an even-order axis of symmetry. The polarization of the wave is normal to the sagittal plane and is associated with an electric field. It is thus similar to a shear horizontal (SH) wave, which can exist in isotropic materials and is present in the bulk of the material, and not confined to just the surface. The piezoelectric property of the material causes Bleustein-Gulyaev waves to be more confined to the surface compared to SH waves, but the wave penetration is still much greater than the wavelength ($10-100 \lambda$), so the velocity of the two waves is quite similar. As such, there have been methods

developed to confine the wave to the surface region. One method is to use a thin substrate on the order of the acoustic wavelength, producing SH acoustic plate modes (SH-APMs). In these modes, the wave is reflected back and forth from the boundaries of the substrate, effectively trapping the wave near the surface. However, one of the biggest drawbacks of this type of wave is that several different wave modes are often excited at once, which increases the chance of mode hopping in an oscillator circuit.

Surface transverse wave (STW) devices utilize a metal grating on the surface along the propagation path to trap the acoustic waves [30]. An increasingly popular type of wave is the Love wave, shown in Fig. 2.3b. Love waves are named after A. E. H. Love, following his development of mathematical theory for the propagation of surface waves in 1911 [31]. A Love wave device consists of a wave-guiding layer that is deposited on top of the substrate surface to confine the wave energy within the layer and the part of the substrate closest to the interface. By applying the appropriate boundary conditions for the solutions to the propagation equation, namely that the tangential stresses cancel out at the top of the waveguide layer and that they are continuous at the interface between the waveguide layer and the device surface, the system has a nontrivial solution only when the guiding layer's propagation velocity is less than the substrate's. This is the necessary condition for a Love wave to exist. It can then be shown that the acoustic energy is concentrated in the layer. The larger the difference in velocities, the stronger the confinement [25]. A variety of materials have been used for the waveguide layer, including silica [32, 33], polymethylmethacrylate (PMMA) [34, 35], and photoresist [36, 37].

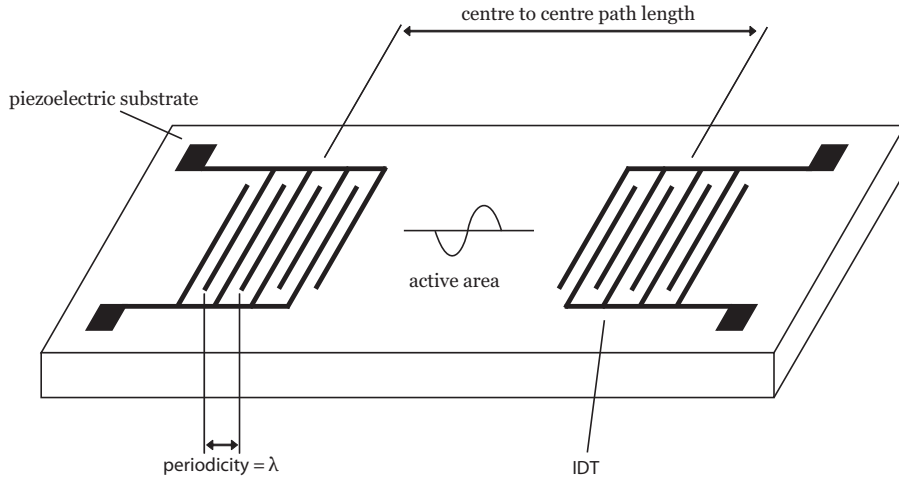


Figure 2.4: Schematic representation of a two port delay-line SAW device.

2.2.5 Delay-line SAW devices

The most common type of SAW sensor is the two-port delay-line device shown in Fig. 2.4, consisting of the piezoelectric substrate and two interdigitated transducers (IDTs). IDTs are simply comb-like, periodically arranged, metal electrode fingers. The sole purpose of the IDTs is to convert an electric input signal to a mechanical one (the acoustic wave) at the input, and *vice versa* at the output. The “delay-line” name comes from the fact that the mechanical signal travels significantly slower than it would if it were an electromagnetic signal [38]. When an alternating electric potential is applied to one set of IDTs, a corresponding alternating mechanical strain is induced due to the piezoelectric effect, and SAWs are produced. The SAWs radiate away from the IDT, effectively creating pairs of identical waves travelling in opposite directions. The fundamental frequency of the device is defined as:

$$f_0 = \frac{v_0}{\lambda}, \quad (2.15)$$

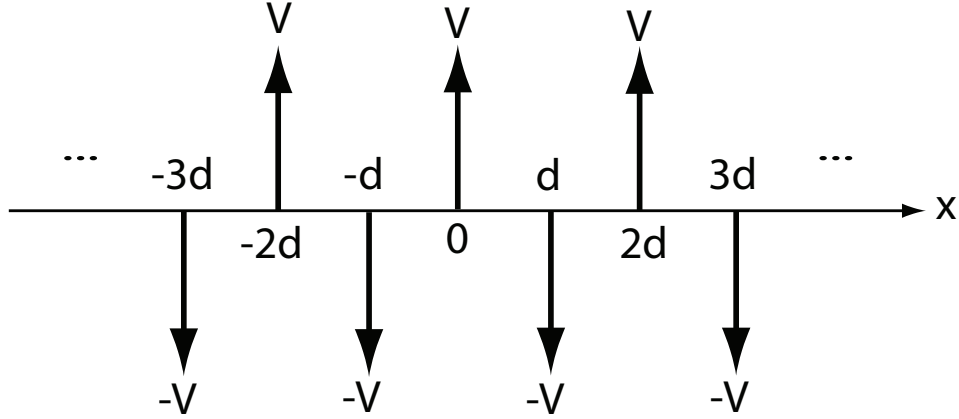


Figure 2.5: IDT consisting of an infinite number of electrodes with alternating impulses of magnitude V .

where v_o is the acoustic wave velocity and λ is the acoustic wavelength, which is dictated by the periodicity of the IDTs (Fig. 2.4). If the SAW frequency matches the fundamental frequency, then the induced waves from each finger pair of the IDT will be exactly in phase and add constructively. As the frequency of the SAW shifts away from the fundamental frequency, there will be increasingly more destructive interference and eventually the wave will cease to exist [30].

To understand the frequency response of an IDT, the Fourier transform can be used to relate the time domain with the frequency domain. First, consider an IDT with an infinite number of alternating polarity electrodes (Fig. 2.5). The distance between successive electrodes is $d = \lambda/2$, so that the electrodes are spaced in time by $d/v_o = 1/2f_0$. It can be shown that the Fourier transform of this sequence in time results in an infinite series of impulses at $(2n + 1)f_0$, where $n = 0, \pm 1, \pm 2, \dots$ [39]. Imposing the constraint that the number of electrodes is finite results in the multiplication of the signal in time by a rectangle function of length N/f_0 , where N is the number of pairs of electrodes. This corresponds to a convolution of $(N/f_0)\text{sinc}(N\pi f/f_0)$ (Fourier

transform of the rectangle function) with the sequence above, in the frequency domain. The frequency response of the IDT thus consists of sinc passbands around odd multiples of f_0 , with the sharpness of these bands increasing with N . It should be noted that the electrodes were approximated as line charges, where in reality they have a finite width with a charge distribution. The inclusion of the charge distribution will add a proportionality factor with the sinc function, but the overall shape of the response is relatively unchanged. Furthermore, while the charge distribution on the electrodes near the ends of the IDTs is different from those in the middle, the approximation is generally sufficient when N is large so that these effects can be ignored. Typical values of N found in the literature range from 30–80.

2.2.6 SAW sensors

The “surface” nature of SAWs is what makes them particularly appealing for sensor applications. Since the SAW is confined near the surface of the substrate, any changes that occur at the surface, or surface perturbations (*e.g.*, mass deposition, changes in conductivity, changes in viscosity of the adjacent media) along its path will be reflected in the wave measured at the output. This is also why SAW devices are much more sensitive than traditionally used TSM devices, which operate at much lower frequencies due to substrate thickness requirements. Typical mass sensitivities of TSM devices are on the order of $14 \text{ cm}^2/\text{g}$, where Rayleigh mode SAW sensors have sensitivities on the order of $200 \text{ cm}^2/\text{g}$ [38].

For a given acoustic mode, changes in the propagation velocity are reflected in a change in resonant frequency because the wavelength is fixed by the geometry of the IDTs [30]. Changes in signal amplitude will also be reflected

with changes in the insertion loss (IL), which is the amount of power lost from input to output. SAWs were first investigated as sensors in 1979 by Wohltjen and Dessy, who used Rayleigh mode SAWs for organic gas detection [13, 40, 41]. Since then, there has been considerable progress in the development of SAW gas sensors [42–44]. A major drawback of these Rayleigh wave devices, however, is that operation in liquid media is not possible because the surface-normal displacements directly couple with the liquid to generate compression waves. These waves radiate into the liquid and result in significant attenuation of the SAW, *i.e.*, high IL [45]. SH-polarized waves, on the other hand, do not excessively couple with the liquid because the particle displacement is parallel to the device surface. In particular, Love wave devices are particularly attractive because they exhibit higher sensitivities due to the trapping of acoustic energy to the wave-guide layer [46]. As such, there has been a considerable number of studies on Love wave devices in the past two decades. This includes theoretical studies of sensitivity [47], use of different waveguide materials [34, 48–50], and use of different substrate materials [51]. In this thesis work, Love-wave devices are used exclusively.

Any surface perturbation will always affect the travelling SAW by altering the amplitude and/or velocity (and hence operating frequency). Perturbation theory, which involves the solving of an known equation and solution with the addition of a small change or perturbation to it, has already been applied to describe the interaction of a SH-polarized SAW with mechanical surface perturbations [46]. The changes in the complex propagation factor, γ , are related to the wave energy and velocity by:

$$\frac{\Delta\gamma}{k_0} = \frac{\Delta\alpha}{k_0} - j\frac{\Delta v}{v_0}, \quad (2.16)$$

where k_0 , α , v_0 , and v are the wavenumber, attenuation, and the phase velocity before and after the perturbation, respectively. $\Delta\alpha/k_0$ and $\Delta v/v_0$ are then the normalized wave attenuation and fractional change in wave velocity, respectively. SAW devices typically have their wavelength fixed by the IDT spacing, so $\Delta v/v_0 = \Delta f/f_0$ (from Eq. 2.15). The perturbation can be described by a surface impedance, Z , which is related to the wave parameters by:

$$\frac{\Delta\alpha}{k_0} - j\frac{\Delta f}{f_0} = cZ, \quad (2.17)$$

where c depends on the device material and geometry, surface particle velocity and the wave power density [51].

In the case of a rigid mass loading at the surface, or a perfectly elastic, thin film, the surface impedance becomes:

$$Z = j\omega(m/A), \quad (2.18)$$

where ω is the angular frequency and (m/A) is the mass per a unit area. The impedance is proportional to (m/A) and purely imaginary; thus, there is no damping since $\Delta\alpha = 0$.

When the surface perturbation is a viscous liquid (with viscosity η and density ρ) in the adjacement medium, the surface impedance can be shown to be:

$$Z = (1 + j)\sqrt{\frac{\omega\rho\eta}{2}}. \quad (2.19)$$

For this scenario, there is clearly both a real and an imaginary part, giving rise to changes in both amplitude and frequency. The frequency (velocity) shift due to changes in viscosity is proportional to $(\rho\eta)^{1/2}$, which was demonstrated by

Kanazawa and Gordon using aqueous glucose solutions and aqueous methanol solutions with small viscosities [52]. It should be noted that Eq. 2.19 is only valid when $(\omega\eta)/(\rho v^2) \ll 1$, or in other words, the viscosity is low enough that the liquid behaves as a Newtonian fluid, which has a linear stress-strain curve characterized by its viscosity. Beyond a critical viscosity value, η_c , the liquid enters the Maxwellian region and must be modelled accordingly [53]. Maxwell fluids exhibit both viscous and elastic properties.

2.3 Glancing angle deposition (GLAD)

2.3.1 Physical vapor deposition

A common technique used to grow thin films is physical vapor deposition (PVD). In PVD, atoms are first ejected from the source material thereby creating a vapor source flux. These atoms are then transported over some distance, and finally impinge on the substrate surface. At the substrate surface, the atoms will then condense, followed by film nucleation and growth [54].

The creation of the vapor source flux can be achieved by a variety of processes. Thermal evaporation involves the heating and then vaporization of the source material. A similar and more commonly used process, termed electron beam (e-beam) evaporation, uses a focused electron beam to heat and vaporize the source material. Sputtering is another commonly used process, but rather than heating the source material, energetic particles are used to dislodge and eject atoms from the surface of the source material. Other PVD processes include cathodic arc deposition, ion-plating, and pulsed laser deposition. For the work in this thesis, e-beam evaporation was exclusively used.

A key requirement for PVD is that it must be performed in high-vacuum

(very low pressure) environments. Under high vacuum, the characteristic mean free path of gas molecules between collisions is significantly larger than the source-to-substrate distance. The source material, now in vapor form, then follows a straight-line ballistic path to the substrate. This effectively allows for a consistent, reproducible transport of atoms from the source to the substrate. The lack of scattering also makes collimation of the flux possible. A high-vacuum environment also significantly reduces the number of impurities that may be integrated into the film during deposition, resulting from the lower number of molecules and hence, fewer random collisions between molecules and the substrate.

The final steps in PVD thin film growth are condensation and nucleation. When the source atoms arrive at the substrate, they may adsorb and remain on the surface, adsorb and re-evaporate after a finite time, or reflect immediately from the surface. Atoms that adsorb to the surface (adatoms) may be mobile across the surface. This can lead to clustering of atoms that encounter each other, resulting in the formation of a nucleus. The stability of a nucleus is a function of the thermodynamics of the system, as well as the size of the nucleus. Due to the very large surface-to-volume ratio, a small nucleus is more favorable to evaporate from the surface than a large one. However, once a critical size has been reached, then it becomes significantly more probable that the nucleus will be stable and remain on the surface. The critical nucleus size, the size with an equal probability of remaining on the surface as re-evaporating, is the minimum nucleus size for nucleation to proceed. The critical nuclei are the main sites for further film growth. The critical nucleus size depends heavily on the substrate temperature, where a higher substrate temperature results in a larger critical nucleus size [55].

As the deposition continues past these initial stages of nucleation, film structures begin to form. An important factor affecting the structure is the substrate temperature, and this has been studied extensively by Movchan and Demchishim. They proposed a structure zone model (SZM) relating film structure to the ratio of substrate temperature to material melting point (T/T_M) [56]. In their model, three distinct structural zones were identified and defined by boundaries at T/T_M values of 0.3 and 0.5. In the first zone ($T/T_M < 0.3$), the low temperature causes low adatom mobility, resulting in the growth of individual nuclei. As they grow larger, they begin to block neighboring sites from the incoming vapor flux, a concept known as atomic shadowing. The flux is thus captured by the shadowing nuclei and increasing their size, resulting in columnar structures separated by voids. Increasing the temperature and transitioning into the second zone ($0.3 \leq T/T_M \leq 0.5$), adatom mobility increases and surface diffusion is able to overcome the shadowing effect, resulting in less defined columns and producing columnar grains. In the third zone ($0.5 \leq T/T_M$), the high temperatures cause bulk diffusion, leading to crystallization and densely packed grains.

In general, there are three possible modes of film growth on surfaces [57, 58]. Volmer-Weber or island growth occurs when the adatoms are more strongly bound to each other than to the substrate. As a result, they agglomerate and form 3D clusters or nuclei. Conversely, Frank-van der Merwe or 2D layer growth occurs when the adatoms are more strongly bound to the surface than to each other. Thus, the initial adatoms will form a complete monolayer on the surface followed by less tightly-bound successive layers. The final growth mode is a combination of the layer and island modes, termed Stranski-Krastanov growth. This mode proceeds initially with layer growth, and then by subsequent island

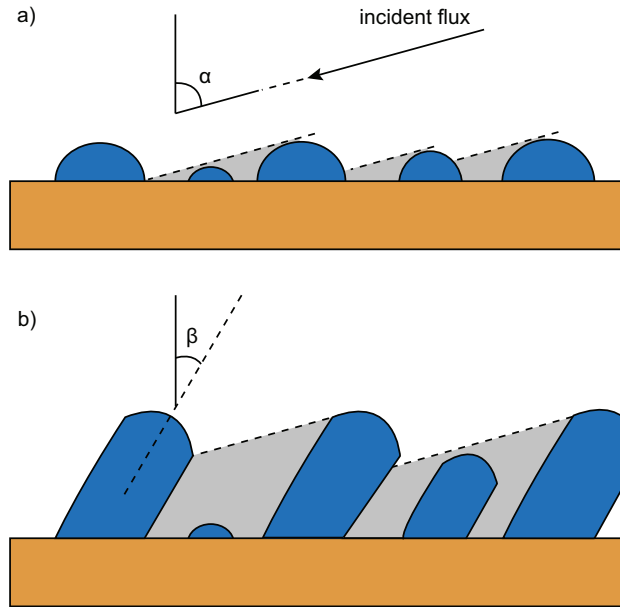


Figure 2.6: A schematic of film growth at an oblique angle α . (a) As nucleation sites grow in size, they begin to block the region directly behind them from the incident vapor flux. These shadowed regions have no film growth. (b) As the deposition proceeds, only the exposed nuclei continue to grow by capturing the incoming vapor atoms, and develop into columns tilted towards the incident flux at an angle β .

growth.

2.3.2 Glancing angle deposition

Traditional PVD methods for thin film fabrication employ a source flux arriving perpendicular to the substrate surface, which generally produces solid thin films. Unlike traditional PVD, GLAD employs a source flux arriving obliquely at an angle α , relative to the substrate normal. During the initial stages of film growth, the initial nuclei begin to shadow the regions directly behind them from the ballistic vapor atoms, as shown by the shaded regions in Fig. 2.6a. This effectively limits the growth to the nuclei that cast these shadows, with the dominant growth on the side directly exposed to the flux. High surface

diffusion will reduce the effect of shadowing, allowing adatoms to move into shadowed regions. Thus, GLAD typically operates at a low substrate temperature to limit adatom diffusion (Zone I of the SZM). The combination of ballistic shadowing and low adatom mobility results in columnar structures tilted towards the incoming flux, with an angle β relative to the substrate normal (Fig. 2.6b), where $\beta < \alpha$ [59–61]. An example of these slanted post structures is shown in Fig. 2.7a. As α increases, particularly at $\alpha > 80^\circ$, shadowing becomes more significant, resulting in larger column diameters and intercolumn spacing [62].

GLAD is a powerful deposition technique because it allows for precise control of film structure by controlling the substrate motion during deposition. More complex structures than slanted posts can be fabricated by manipulating/rotating the substrate around its normal axis, ϕ , effectively controlling the direction of column growth. For example, by discretely rotating the substrate in $\phi = 180^\circ$ increments, chevron structures can be obtained (Fig. 2.7b). If the rotation becomes continuous at a slow, constant rate, helices are produced (Fig. 2.7c). These helices will degenerate into vertical posts if the rotation rate is increased sufficiently. The deposition angle α can also be manipulated during deposition to control film density and porosity. For example, dense capping layers have been created by decreasing α significantly ($< 45^\circ$) near the end of the deposition, while maintaining substrate rotation [62, 63]. Advanced GLAD techniques, such as PhiSweep [64], have also been developed to control film morphology. PhiSweep is a technique that was developed to control film broadening, where the film structures experience an increase in their dimensions with film thickness [64]. A wide range of film structures using GLAD is thus possible by simultaneously controlling ϕ and α .

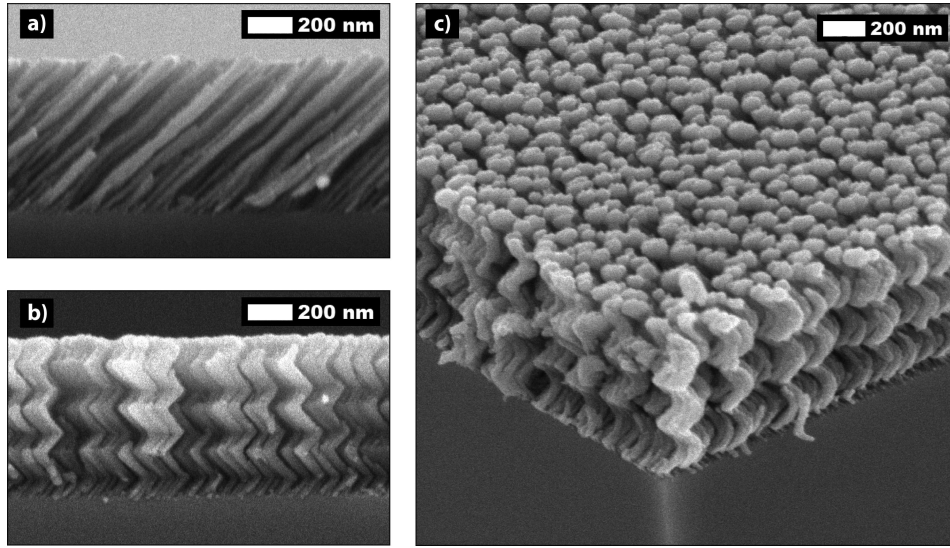


Figure 2.7: Examples of structures fabricated with GLAD using SiO_2 : a) slanted posts, b) chevrons, c) helices.

The flexibility and tunability of the GLAD technique has resulted in its application in a wide spectrum of fields. Perhaps the most obvious application of controllable micro and nanostructures would be for optics. Examples include, but are not limited to, antireflection coatings [65, 66], optical filters [67, 68], photonic crystals [69], and optical humidity sensors [70, 71]. On a closely related topic, GLAD films have also been applied to enhance solar cell performance [72–74]. Conversely, thermal barrier coatings [75], humidity sensors [76–78], and ultrathin-layer chromatography layers [79, 80] have utilized GLAD to enhance their performance.

2.4 Summary

This chapter provided a review of the material pertaining to the work in this thesis. A background of elasticity was introduced, followed by a discussion leading into the principles and operation of SAW devices. Only Love wave

SAW devices were used in this work, owing to their high sensitivity and ability to operate in liquid environments. The basics of thin film deposition and PVD were also covered in this chapter, introducing important concepts that are relevant to the GLAD technique. Low temperature and ballistic shadowing allow for the formation of columnar structures that can be further tailored by controlling substrate motion during deposition. With this background introduced, the following chapter will concentrate on the experimental details of this thesis work.

Chapter 3

Experimental methods

3.1 Introduction

In the previous chapter, an introduction to the theory required to understand the fundamentals of SAW operation was given. This chapter describes the design, fabrication and characterization of the Love wave SAW devices used in this thesis. Design considerations for IDT geometries and materials (substrate, waveguide, *etc.*) are discussed, followed by a description of the optical lithography methods used to fabricate the devices. The equipment and methods used to fabricate the GLAD films used in this thesis will also be introduced. Finally, a brief overview of the measurement techniques used to characterize the devices will be given.

3.2 Design and fabrication of SAW devices

3.2.1 SAW substrates

The most common piezoelectric materials used for SAW devices are quartz, lithium niobate, and lithium tantalate [12]. There are advantages and disadvantages for each material, and some important factors to consider when choosing between them include cost, temperature dependence, K^2 values, and propagation velocities. For example, Y - Z lithium niobate¹ is used to generate Rayleigh waves, and has an extremely high K^2 value compared to ST - X quartz, but is much more expensive and has a significantly higher temperature coefficient of delay (TCD). Many of the material characteristics are also a function of the direction of wave propagation along the crystal cut. In this thesis, Love wave devices are exclusively used, so only substrates that support SH-polarized waves were considered. ST -cut quartz (Sawyer Technical Materials, LLC.) was chosen for use based on its low-cost, availability, and wide-use [37, 81–83]. When the propagation direction is perpendicular to the crystallographic X -axis, SH-polarized waves are known to be produced [34, 84]. Furthermore, the propagation velocity (4990 m/s) is much higher than the same corresponding waves in Y -cut lithium niobate (3158 m/s) and 128° -cut lithium niobate (3992 m/s)[25]. This allows for greater trapping of the wave energy with a given waveguide material. The larger the difference in acoustic velocity between the substrate and the waveguide layer, the larger the trapping effect [85].

¹This notation is used to describe the crystal’s orientation, The first letter indicates the directional cut of the crystal, and the second letter indicates the propagation direction.

3.2.2 IDT design

Aside from the choice of substrate, IDTs are often the main factor affecting device performance. The most basic IDT, the solid-electrode IDT, consists of single, alternating electrodes and is shown in Fig. 3.1a. The period of the IDT is equal to $2(d + w)$, and the metallization ratio, η , is defined as $d/(d + w)$. The nominal value used for η is usually 0.5 ($d=w$), and small changes around this value do not adversely affect the amplitude of the signal at f_0 [39]. While the solid-electrode IDT is sufficient in producing SAWs, there is a significant problem with it. The electrodes, having a small but finite thickness, act as a discontinuity at the surface and thus will reflect part of the SAW. The magnitude of these reflections is in general small, but for a large number of electrodes it begins to become quite significant. The distance between successive electrodes is $(d + w)$, so a reflected wave will have traveled $2(d + w)$, which is exactly one wavelength at f_0 . The reflections will therefore add up constructively and be detrimental to signal at the intended operating frequency. To eliminate this problem, the IDT structure shown in Fig. 3.1b can be utilized. This IDT, known as the split-electrode IDT, has successive pairs of electrodes of the same polarity. With this geometry, the path length of reflected waves between neighboring electrodes is now $\lambda/2$, and the reflected waves cancel each other out. If d and w are the same as with the solid-electrode IDT, then the periodicity has doubled and the operating frequency is halved. Thus, to retain the same operation frequency as a solid-electrode, the electrodes must be twice as close together. Depending on the desired f_0 , this can be problematic with contact photolithography, which has a minimum resolution of a few micrometres.

Typical operating frequencies for SH SAW devices range from 30–300 MHz

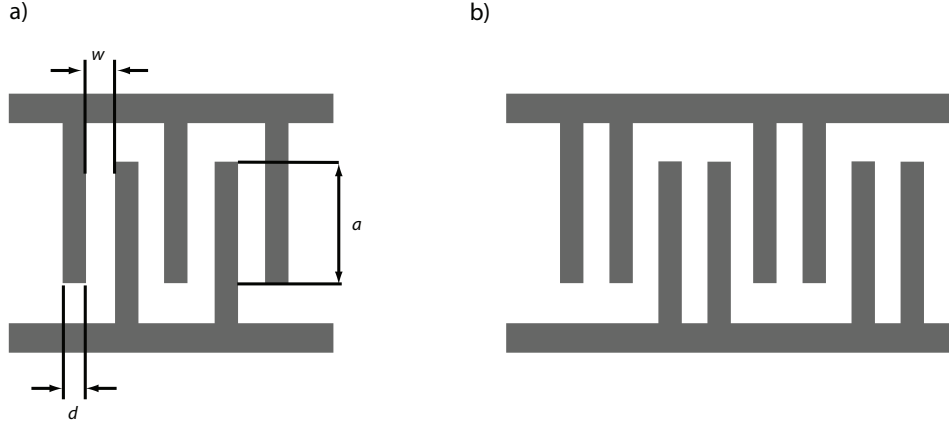


Figure 3.1: Schematic of a) a solid-electrode IDT and b) a split-electrode IDT with finger width d , spacing w , and aperture a .

[38], so for ST-quartz this imposes a range of 166–16 μm for the periodicity of the IDTs (or wavelength of the device, Eq. 2.15). A periodicity of 40 μm with 50 pairs of electrodes was chosen for work in this thesis in keeping with typical values seen in literature. This results in an operating frequency of about 125 MHz. A split-electrode design was employed and thus required electrode widths and spacings of 5 μm . The aperture (a , in Fig. 3.1a) and center-to-center distance between the IDTs were chosen to be 75λ and 125λ , respectively. Because of the finite aperture of the electrodes, diffraction will be present during the operation of the device. Diffraction causes a spreading of the wavefronts, diverting from the desired planar wavefronts. However, there is a region where the wave propagates as a plane wave, known as the near-field or Fresnel zone. It is thus desirable to design the device such that it operates within this field so that the output IDT can capture all the power. The near-field length is defined as:

$$N_l = \frac{a^2}{4\lambda},$$

where a is the aperture of the electrodes. For the chosen aperture then, the near field length is 141λ and the chosen propagation length is hence within the considered near-field. The aperture and propagation length values were also comparable with those seen in the literature.

3.2.3 Fabrication details

Photolithography is a process that involves transferring a pattern from an optical mask onto the substrate [86]. The substrate is coated with photoresist, overlaid with the optical mask, and exposed to ultraviolet (UV) radiation. The UV exposure changes solubility of the photoresist to the developer, which is used to remove it and create the pattern that was transferred from the mask. There are two types of resists available: negative and positive resists. After exposure to UV light, negative resists become insoluble in the developer, whereas positive resists become more soluble. In general, positive resists provide better edge definition than negative resists, so they are more commonly used for high-resolution patterns for microdevices [87]. After the pattern has been transferred to the substrate, the resist pattern is used as an etch mask. Wet or dry processes are used to remove the layer(s) of materials on the substrate to directly transfer the pattern to the substrate. The remaining resist is removed in the final step to complete the process.

The mask that was designed and used is shown in Fig. 3.2. This mask allows for the fabrication of 28 devices, and it can be seen that the edges of the SAW devices are slanted. This design consideration was implemented to reduce interference caused by waves reflecting back from the edges of the device. The angled edges will reflect the unwanted signals out of the path of the delay-line [30].

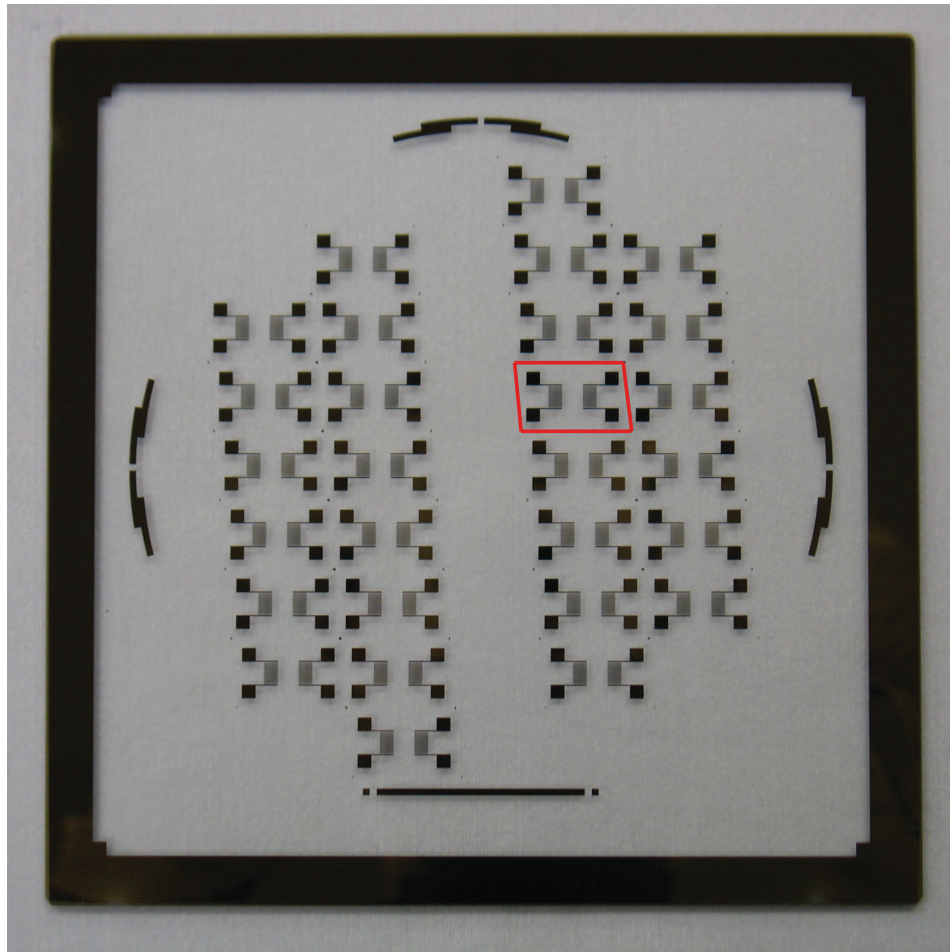


Figure 3.2: Optical mask used to fabricate SAW devices. The red outline shows the parallelogram shape of a device after dicing.

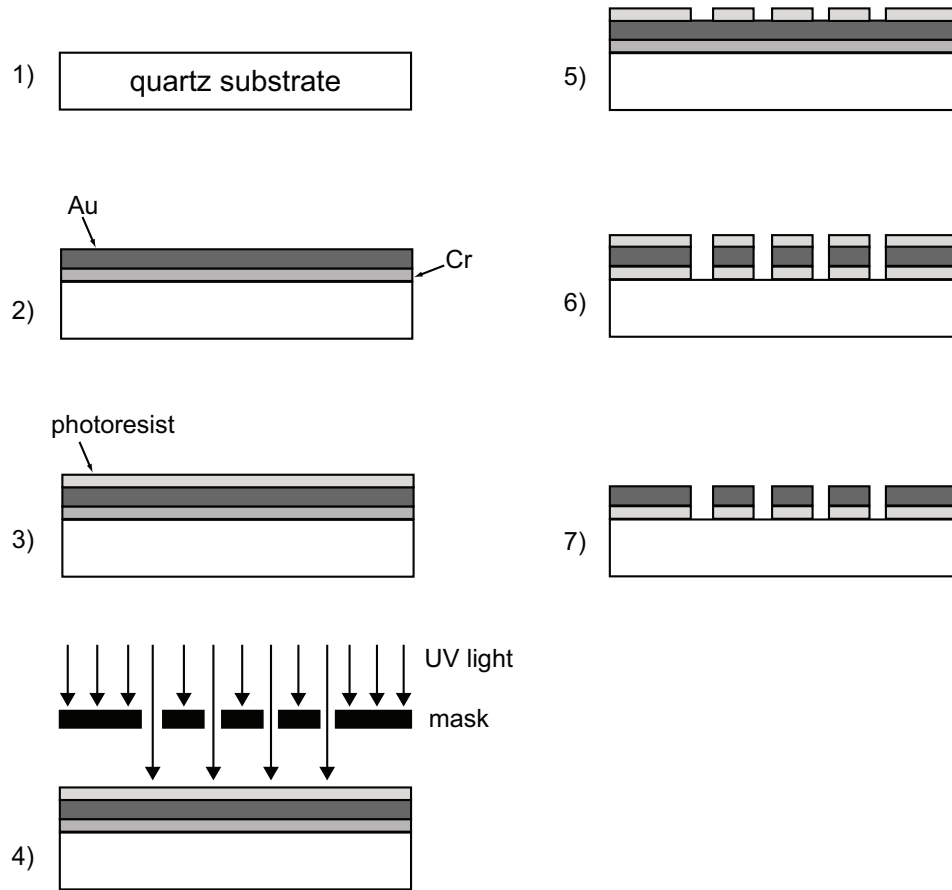


Figure 3.3: Process flow for SAW device fabrication showing the deposition of metals (step 2), photolithography (steps 3-5), and metal etching (step 6).

The general process flow used to fabricate the SAW devices is shown in Fig. 3.3. The quartz substrates were initially cleaned by immersing in piranha (3:1 solution of 96 % H_2SO_4 : 30 % H_2O_2) for 15 min to dissolve any organic impurities on the surface. The metals deposited for the IDTs were gold, with a thin layer of chromium metal as an adhesion layer. Aluminum is another common metal used, but gold was chosen for its higher resistance to oxidation. In step 2 of Fig. 3.3, 30/120 nm thick layers of Cr/Au were deposited by a planar magnetron sputtering system. HPR 504, a positive photoresist, was then spun onto the metallized substrates with a 10 s spread at 500 rpm followed

by the spin for 40 s at 4000 rpm. The substrates were then softbaked at 115 °C for 30 min to cure the resist, resulting in an $\sim 1.25\ \mu\text{m}$ thick layer (step 3). Step 4 was carried out with an ABM mask aligner with a 365 nm UV light source. The mask aligner was used to align the substrate with the mask and expose the photoresist for 2.0 s at $\sim 14\ \text{mW}/\text{cm}^2$. After exposure, the substrate was developed to produce the pattern from mask (step 5). To imprint the pattern into the Cr/Au layers, the metal layers were etched using pre-made wet chemical etchants specific for each metal (step 6). The Cr etchant is a commercially prepared solution containing ceric ammonium nitrate and nitric acid. The Au etchant was prepared by the University of Alberta NanoFab staff and contains potassium iodide and iodine. It should be noted that the Au etchant was diluted with 1:1 volume of water to allow for more precise control of the amount of Au removed. The substrate was then rinsed with acetone to remove the photoresist layer, resulting in the device in the final step of Fig. 3.3. The individual devices were then obtained by using a dicing saw (Diamond Touch). Device yield was on the order of 75%. This could be improved with optimization of the UV exposure and wet etching times, as well as using larger electrodes since the 5 μm electrode widths and spacings are near the limit of the resolution of the photolithography equipment.

3.2.4 Waveguide layer

As previously mentioned in Sec. 2.2.4, many materials for the waveguide layer have already been explored. In particular, amorphous SiO_2 has often been utilized for its excellent elastic and thermal properties [46, 85, 88]. It also exhibits high chemical resistance and can be easily tailored with a wide range of chemical functionalities [89, 90]. On the other hand, the shear velocity

(around 2850 m/s [23]) is relatively high compared to polymers such as PMMA (around 1100 m/s [84, 91]), resulting in weaker trapping of the wave energy. The optimum thickness of an SiO₂ waveguide layer was calculated to be 6.8 μm for a device with a wavelength of 40 μm [47]. In practice, thicknesses on this order are very difficult to achieve due to problems related to film adhesion and stress. PMMA, however, can be deposited without these issues very easily and cheaply by means of spinning. The lower acoustic velocity of ≈ 1100 m/s also allows for better trapping and thinner layers [34, 85]. For these reasons, PMMA was used as the waveguide layer material in this thesis.

The use of PMMA as a guiding layer has already been studied in detail by many groups over the past two decades [34, 51]. With these in mind, a common PMMA thickness was chosen for this thesis as an initial parameter choice and kept constant throughout all experiments. Prior to PMMA deposition, the SAW devices were cleaned by sonicating in acetone for 10 min, followed by rinsing with acetone, isopropyl alcohol (IPA), and de-ionized (DI) water. 495PMMA A11 (MicroChem) was spun onto the SAW devices (*i.e.*, overtop the electrodes and contact pads) at 4500 rpm for 50 s, followed by a bake at 185 °C for 3 min to cure the PMMA. The PMMA on the electrode pads was carefully removed with a razor blade so that they could be accessed. The thickness of the guiding layers was about 1.1 μm , as measured with a KLA-Tencor Alphastep IQ profilometer.

3.3 Fabrication of GLAD thin films

3.3.1 Deposition systems

GLAD can be achieved by a variety of PVD techniques (sputtering, thermal evaporation, e-beam evaporation, etc.), but only e-beam evaporation was used in this thesis work. Two custom-built deposition chambers (Kurt J. Lesker AXXIS systems) were used to deposit the GLAD films used in this thesis. The systems are nearly identical in functionality and have only minor differences in their hardware. Use of a particular system was made based on availability, but the same system was used for a given set of experiments to ensure consistency. Each system has a dedicated system of vacuum pumps to prepare the required high-vacuum environment for deposition. The source material was evaporated via heating by a focused electron beam that was rastered in a circular pattern. Substrates were mounted on a chuck that is positioned directly above the source material to capture the vapor flux. The distance between the source and substrate is approximately 40 cm. The layout of the deposition chamber can be seen in Fig. 3.4.

The deposition rate is controlled by the electron current and monitored by a quartz-crystal microbalance (QCM), also known as a crystal thickness monitor (CTM). As mass is deposited on the CTM, it will cause shifts in its resonance frequency that can be measured and accurately related to deposited mass. This is related to a film thickness, and hence deposition rate, by using the material density and Z-ratio. The deposition rate is continually read by a computer program and used as a feedback mechanism to control the substrate motion in α and ϕ according to a user-defined file. This file is used to dictate the position of the substrates at a given thickness to achieve the desired film

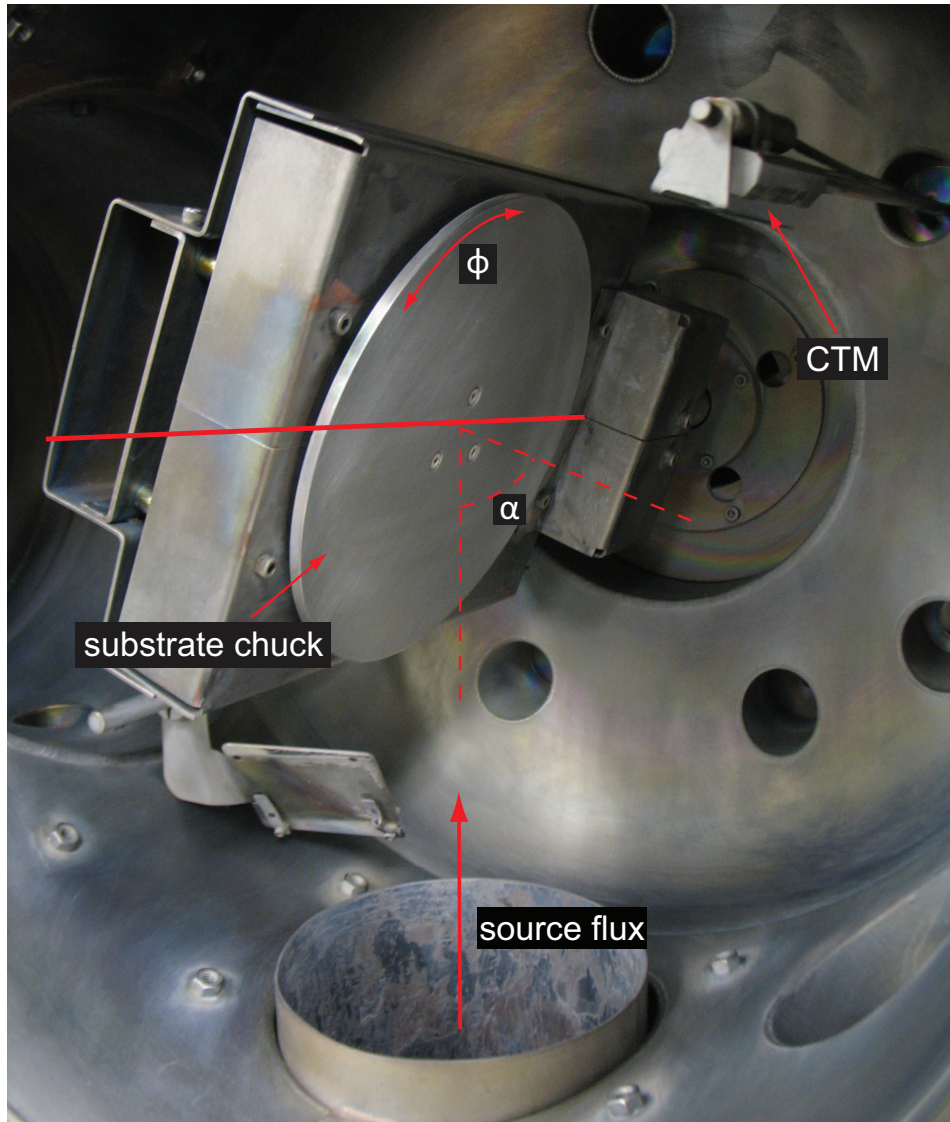


Figure 3.4: Deposition chamber.

structure.

3.3.2 General deposition method

Prior to deposition, the chamber was pumped to a base pressure of $< 10^{-6}$ Torr. All films in this thesis were deposited using SiO_2 source material (1–3 mm pieces, 99.99% purity from Cerac, Inc.). In addition to the advantages outlined in Sec. 3.2.4, SiO_2 is also a well studied material for the GLAD process [92–94]. The SiO_2 source material was placed in a graphite crucible liner, and refilled after each deposition to maintain consistency of initial conditioning and deposition conditions. The material was conditioned by maintaining a rate of 0.2 ± 0.1 nm/s for 5 min to remove any surface impurities. Only vertical post nanostructures were grown and utilized in this work. The posts were grown by rotating the substrates to achieve a pitch of 5 nm, defined as the nominal film thickness grown per revolution. Deposition rates and final film thicknesses varied throughout this work, and will be discussed more specifically in their respective sections. SAW and Si substrates were used for film deposition. The main purpose of the Si substrates were for characterization. For the deposition of GLAD films onto SAW devices, a 30 nm base layer was deposited prior on top of the PMMA waveguide layer, prior to film deposition. This layer served as a protective layer for the PMMA, as well as a base sensing layer for the humidity sensing in Chapter 4. Fig. 3.5 schematically shows a full fabricated SAW device.

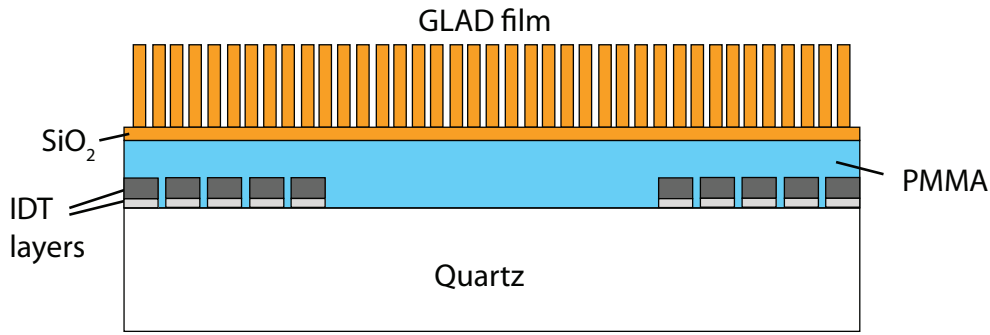


Figure 3.5: Schematic of a fully fabricated Love wave SAW device with a deposited GLAD thin film.

3.4 Sample characterization

3.4.1 Film structure

Scanning electron microscopes (SEMs; Hitachi S4800 and JEOL 6301F) were used to image and characterize film structures and thicknesses. The higher-resolution Hitachi S4800 was used whenever possible, but in general the JEOL SEM was sufficient for most purposes. An SEM functions on the principle of secondary electron emission when the primary electron-beam impinges on the surface of the sample. Other consequences of this interaction with the surface, such as backscattered electrons and x-ray emission, are also possible, but were not applicable to this work. An SEM image is produced when the electron-beam is rastered across the surface while measuring the intensity of secondary electrons emitted at each point, which is then converted to a pixel intensity. The number of secondary electrons emitted is dependent on many factors, including material composition, beam energy, and surface topography. The latter of these factors allows for the accurate imaging of the film structures grown in this research. Top-down and cross-sectional views were mainly used for imaging.

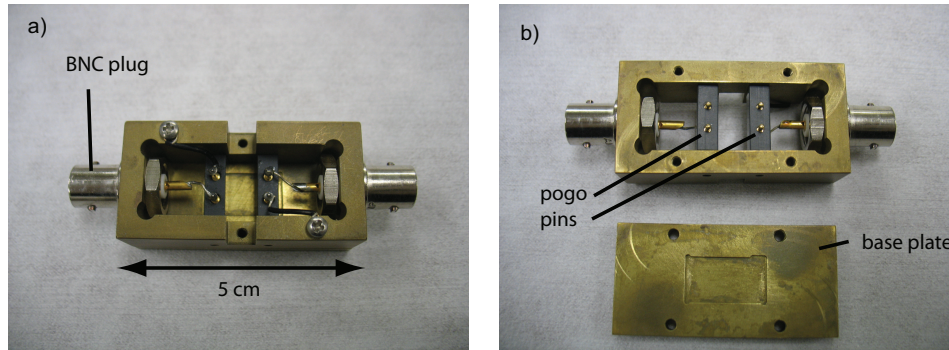


Figure 3.6: Fabricated sample holder for SAW devices. a) Top-down and b) bottom-up views.

3.4.2 SAW device measurement

The use of a device as a sensor requires instrumentation that is able to measure the signal(s) of interest so that the data may be processed and quantified in a meaningful way. For SAW devices, the signals of interest are the amplitude and phase response. For a two port SAW device, there are three electronic configurations to measure either or both of these quantities [25]:

1. The SAW device is connected to a network analyzer or vector voltmeter
2. The SAW device is used as the active element in a feedback loop, controlling the frequency of the oscillator circuit.
3. The SAW device is used as the passive element and driven by a fixed RF source (amplitude or phase measurements).

In this research, only the first two configurations were utilized. A custom sample holder was designed and then made by the Department of Electrical and Computer Engineering's machine shop. The holder (Fig. 3.6) was made of brass, and was comprised of BNC plugs soldered to spring-loaded pogo pins. The use of these pins prevented excessive force from being applied to

the electrode pads of the SAW devices when they were mounted, which would potentially crack the substrate.

The network analyzer (NA) is capable of measuring the characteristic admittance or impedance of the device. These can be expressed in magnitude and phase plots as a function of frequency, allowing for the most detailed information possible about a device under load. A Hewlett-Packard 4396B NA was used to fully measure the frequency response (amplitude and phase) of the SAW devices in this work. An example of the response for a Love wave SAW device fabricated as per Sec. 3.2 is shown in Fig. 3.7 with an amplitude (also known as insertion loss, IL) of about -15 dB at 123 MHz. There are, however, some disadvantages associated with using a NA. The most notable issues are the cost and size of NAs. In general, NAs are very cumbersome and far from portable. The cost, even second hand, is also quite significant, making them impractical for general laboratory use.

The oscillator circuit configuration places the two-port SAW device into the feedback loop of an RF amplifier (Fig. 3.8). The requirement for oscillation is that the overall gain of the loop is equal to 1, or $A(f_0)B(f_0) = 1$. The phase of the loop gain also has to be an integer multiple of 2π to prevent destructive interference of the signal. In practice, the loop gain is often >1 to account for attenuation of the signal due to certain perturbations. In these cases, the signal will continually increase until the limitations of the amplifier/power supply are met. The oscillation frequency will be f_0 , provided that the acoustic pathlength is an integer multiple of the wavelength and there are no phase shifts introduced by the circuit. Relative changes in the acoustic velocity are directly related to changes in the oscillation frequency, as per Sec. 2.2.6. Thus, using a digital frequency counter to measure the oscillation frequency

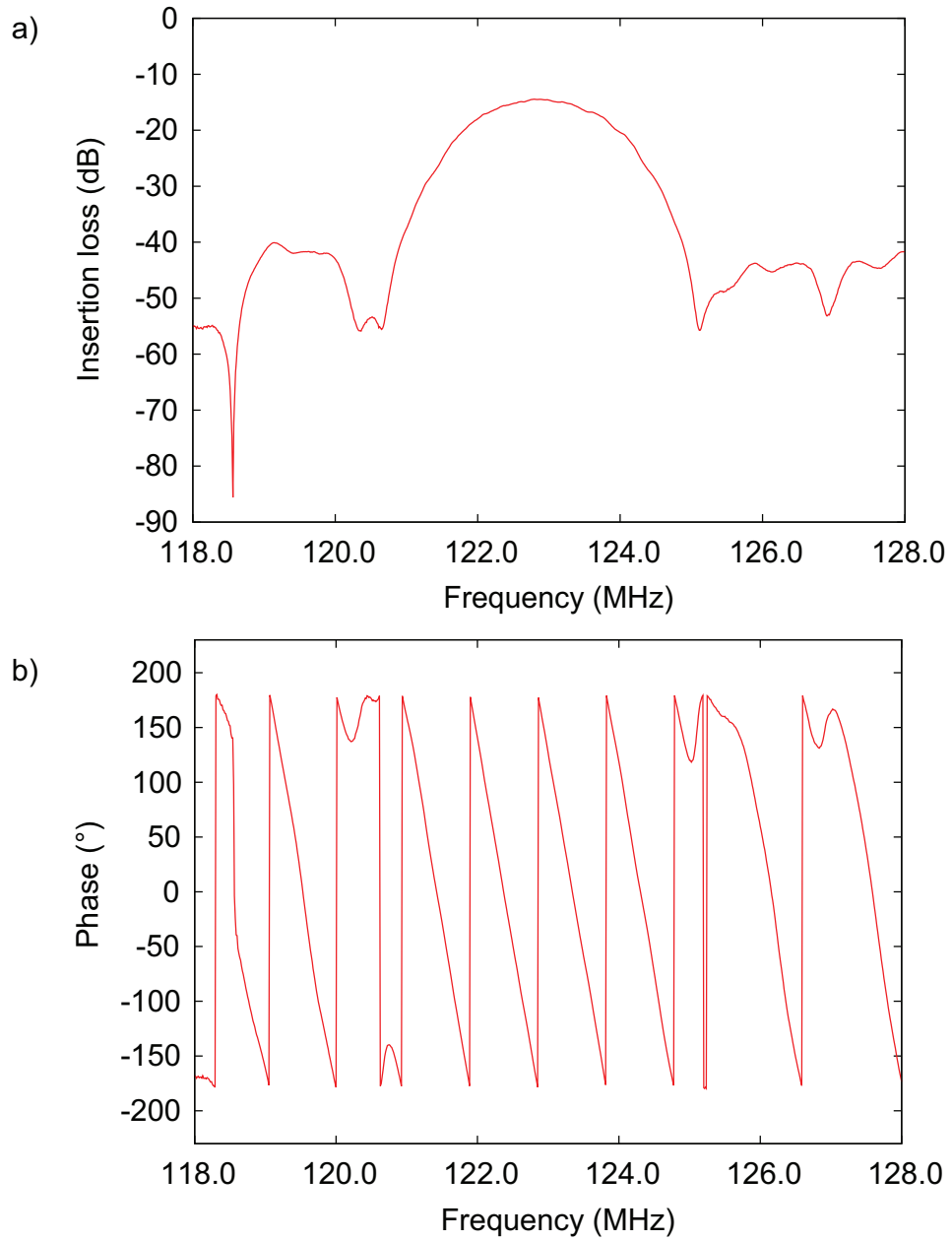


Figure 3.7: The a) insertion loss and b) phase response of a typical Love wave SAW device used in this research.

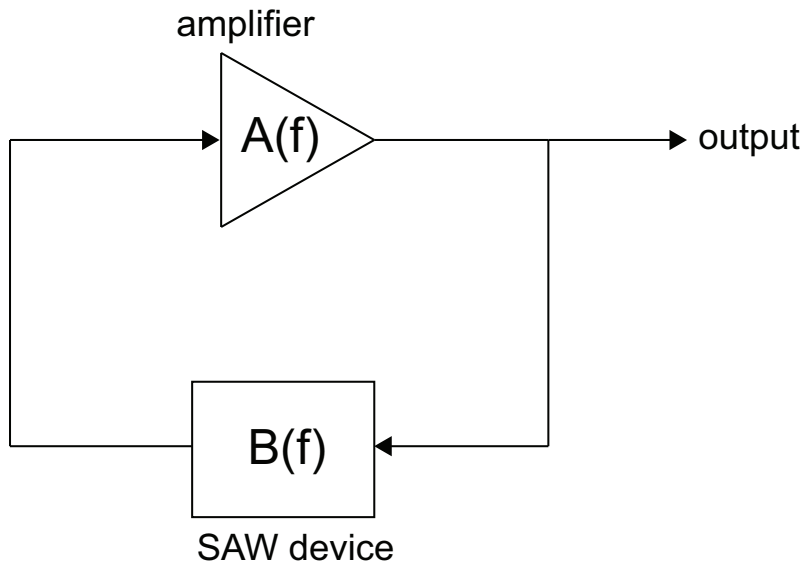


Figure 3.8: General circuit for a SAW device in an oscillator configuration.

provides an indirect, relatively cheap, and accurate method of measuring the acoustic wave velocity [38]. The biggest disadvantage to this configuration is that amplitude measurements generally cannot be made.

The devices in this research were incorporated into an oscillating circuit and the signal was coupled out to a frequency counter (Agilent 53132A) that was interfaced with a computer. The oscillating circuit, shown in Fig. 3.9, included two amplifiers (Minicircuits ZFL-500), a low-pass filter (Minicircuits SLP-150), and a directional coupler (Minicircuits ZFDC-10-1). Each amplifier was powered with a 12 V source, resulting in a gain of 21 dB each and a total gain of 42 dB for the circuit. The additional amplifier was used to ensure that the signal would not be lost from attenuation of the signal during device testing. This was particularly important with liquid loading (Chapter 6), where additional losses were encountered from the attachment of the flow cell and the loading of the liquid itself. The low-pass filter was incorporated to remove unwanted high frequency (>140 MHz) signals and the directional

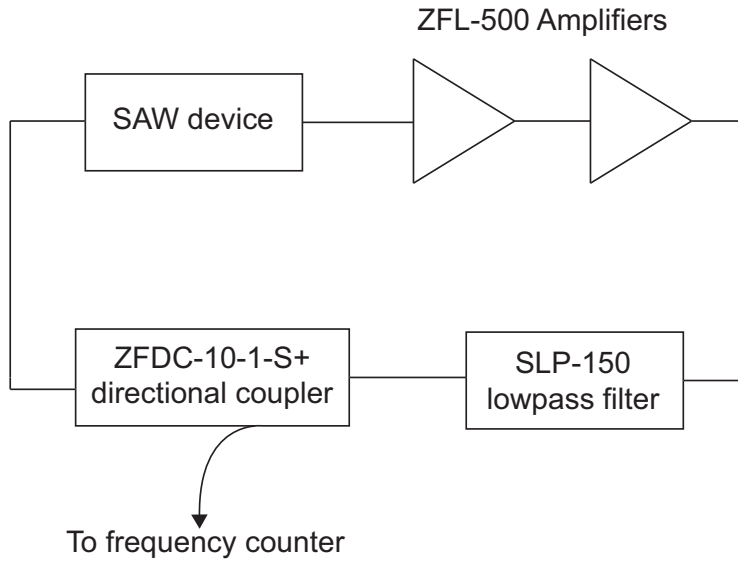


Figure 3.9: Oscillation circuit and its components used for SAW device testing.

coupler coupled the signal out to the frequency counter without impacting the operation of the circuit. The oscillator did not require an external excitation source as the residual noise in the circuit was enough to initiate oscillation.

3.5 Summary

This chapter has described the experimental details regarding the fabrication of SAW devices and GLAD films, as well as the instrumentation used to characterize them. Design considerations for the Love wave SAW devices were discussed in detail, along with the fabrication process that was used. The equipment and general process for depositing GLAD films have also been presented. The SEM was the primary tool used to image and characterize GLAD films in this research. Data for SAW devices were collected by two methods: a network analyzer and an oscillator circuit. The network analyzer allows for a full characterization of device response, while the oscillation configuration is

simpler, more compact alternative to monitor changes in acoustic velocity to device loading.

Chapter 4

Love wave humidity sensors using nanostructured films grown by GLAD¹

4.1 Introduction

One of the most important design considerations for SAW sensors is the choice of sensitive coating or film layer at the surface. This layer provides the sensor with selective adsorption of the target analyte and, thus, a shift in the velocity of the acoustic wave. For gas sensor applications, a wide variety of materials have been employed to fabricate this thin film layer, including polymers [96–100] and carbon nanotubes [101–103]. On the other hand, self-assembled monolayers (SAMs) have been more common for functionalizing the surface for selectivity in liquid sensing [37, 104–106].

The idea of using nanostructures on SAW sensors is a relatively new con-

¹A version of this chapter has been published in *Sensors and Actuators B* [95].

cept. In 2006, Rao and Zhang had suggested that nanostructures would be a promising candidate for increasing the effective surface area of the SAW sensors to enhance the overall sensitivity [14]. They conducted a brief survey of the different types of nanostructures that may be utilized, along with their corresponding fabrication process. Their list included nanopores by anodization, nanopillars by template based electrodeposition, carbon nanotubes by chemical vapor deposition, and even nanorods by GLAD. Since then, many groups have already used a variety of different nanomaterials to enhance the performance of SAW gas sensors. The more commonly studied gases have been volatile organic compounds [43, 103] and humidity [96–100, 107–111]. Sadek *et al.* used ZnO nanorods to create a hydrogen sensor operating at 265 °C [112]. Huang *et al.* also used ZnO nanorods for hydrogen detection, but used a platinum coating on top of the nanorods as a catalyst [113]. Hydrogen sensors utilizing nanostructured polyaniline have also been developed by Arsat *et al.* [114] and Yu *et al.* [115]. Buvailo *et al.* reported a rapid humidity sensor with a TiO₂-based nanomaterial doped with LiCl [98]. The high surface area provided by these nanomaterials increases the amount of gas that is adsorbed at the surface, resulting in larger shifts in the operating frequency and hence enhanced sensitivity.

In this chapter, the impact of dense, nanostructured GLAD films on the device performance of Love wave SAW devices is studied. The thickness of the films was varied and their effects on the response of the devices is reported. These films were also investigated for their efficacy as a sensitivity-enhancing layer for gases. In particular, the sensitivity to humidity was studied because of its simplicity and the hydrophilicity of SiO₂. Selectivity toward other gases can be achieved by chemically functionalizing the surface of the film [116, 117],

but was not investigated in this thesis.

4.2 Experimental

4.2.1 Film fabrication

SiO₂ vertical post nanostructured thin films were prepared using GLAD as per the procedure described in Sec. 3.3.2. A 30 nm layer of solid film was first grown at an angle of 30° to provide a base sensing layer. GLAD films were then deposited on top at an angle of 70° relative to the substrate normal. Films were deposited on both the IDTs and the active area of the devices. Si wafers were also included as substrates for characterization purposes. The deposition angle of 70° was chosen because of the resultant high surface area films (surface area enhancement on the order of $730 \text{ m}^2\text{m}^{-2} \mu\text{m}^{-1}$) [94]. The deposition rate was kept in the range of 1.3–1.8 nm/s, as measured by the CTM. Films were grown to varying thicknesses of 200–700 nm. A reference device with only the 30 nm solid film layer was also fabricated and used for comparison.

Fig. 4.1a and 4.1b are the high resolution, cross-sectional and top-down views, respectively, of a 450 nm thick film. It can be seen that the film consists of tightly packed, vertical post nanostructures with a high porosity. These characteristics are relatively independent of the thickness of the GLAD film in the range studied. Fig. 4.2 shows lower resolution SEM images of thinner (210 nm) and thicker (590 nm) films. While the structures appear to be quite similar for both thicknesses, the top-down images show that the thicker film is less porous, or more dense, at the tops of the film. This is consistent with previous studies that have demonstrated column broadening with increasing

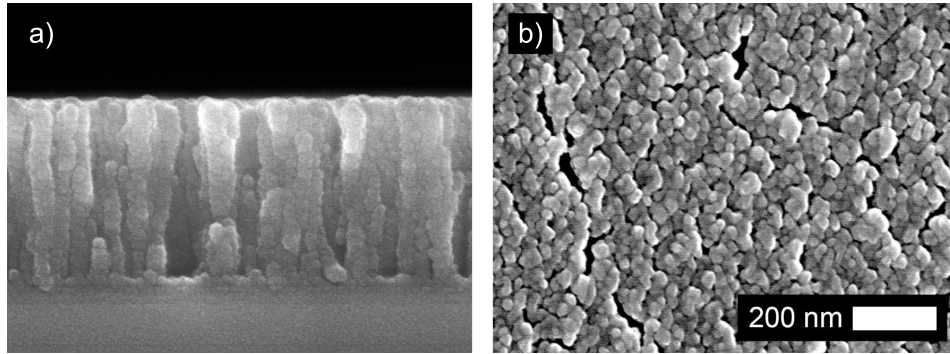


Figure 4.1: a) Cross-sectional and b) top-down SEM images of a 450 nm thick SiO_2 GLAD film with a 30 nm solid underlayer. Scale bar is applicable to both a) and b). Reprinted from [95] with permission from Elsevier.

thickness [64].

4.2.2 SAW measurement setup

The network analyzer was used to examine the IL and phase immediately before and after films were deposited onto the Love-wave devices. Rather than taking the changes in operating frequencies based on the peak IL, they were based on the difference in frequencies at a fixed phase value for each device (Fig. 4.3b). This ensured consistency of the measurement between devices, as even a small change (*e.g.*, due to the added film or other deposited impurities at the surface) in the shape of the response around the peak would significantly alter the measured frequency shift. The process used for measuring these changes is as follows:

1. Take the peak IL for the bare Love wave device, its corresponding frequency, and the phase at this frequency.
2. Deposit GLAD film onto device.
3. Take the peak IL of device afterwards and use this for the change in IL.

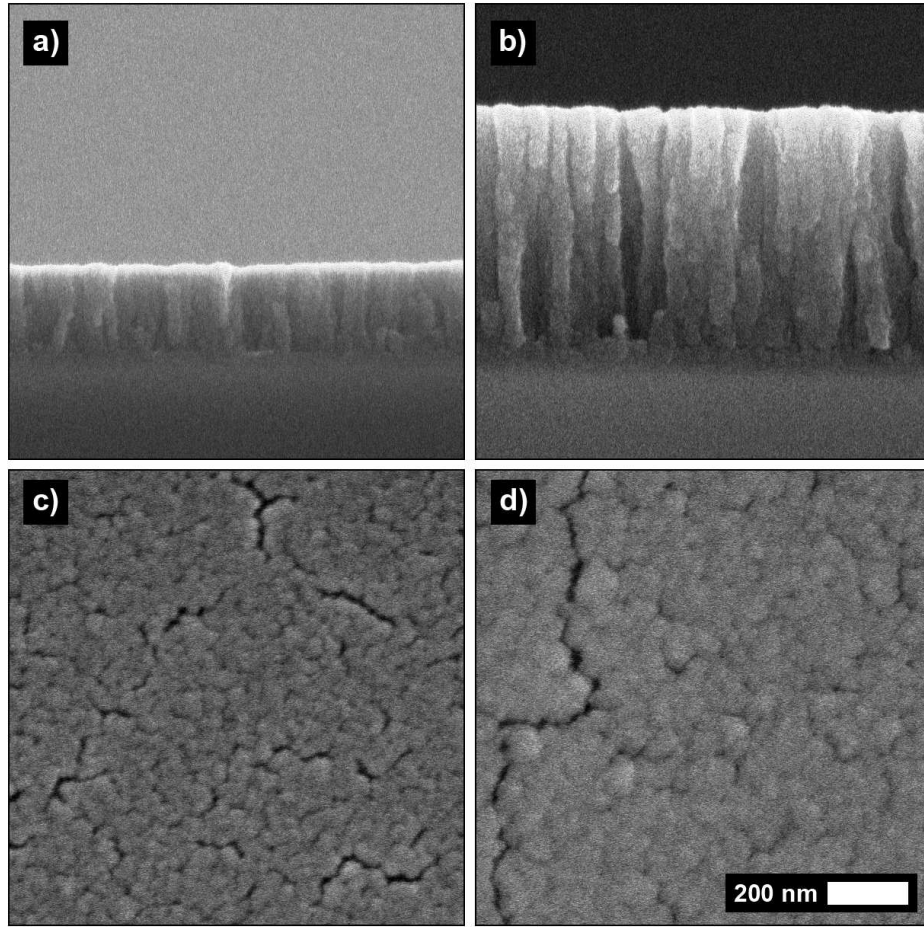


Figure 4.2: a), b) Cross-sectional and c), d) top-down SEM images of 210 nm and 590 nm thick, respectively, SiO₂ GLAD film with a 30 nm solid underlayer. Scale bar is applicable to all images.

4. Look for the phase taken from step 1 in the phase response of the current device. Although the phase repeats after it reaches $\pm 180^\circ$ (like in Fig. 3.7b), the correct frequency position of where that particular phase should be is trivial if the before and after phase responses are superimposed. Since the measured phase response is discretised, then linear interpolation will be required to determine the frequency at that particular phase. Linear interpolation is justified because the phase response itself is linear. For example, if a phase of 146.3° was taken from step 1, and the closest phases to it are 146° and 149° at 123.333 MHz and 123.500 MHz, respectively, then the frequency at which 146.3° should be for this device will be interpolated based on the range between the two phases and corresponding frequencies. The interpolated frequency will then be used to calculate the change in frequency from that taken in step 1.

Humidity tests were run at room temperature ($\sim 23^\circ\text{C}$) using a custom-made humidity control chamber capable of varying the relative humidity (RH) from 0% to 98% [118]. Mass flow controllers (MKS M100B) were used to control the mixture of dry nitrogen and moist air (from a bubbler system), with a maximum combined flow rate of 500 standard cubic centimeters per minute (sccm) at any given time. The chamber humidity, for a given mixture of gases, was calibrated with a Vaisala HMP100 RH probe and the flow of gas was aimed directly onto the SAW device to saturate the surface quickly. The Vaisala probe was previously calibrated with saturated salt solutions by John Steele in his thesis work [119]. Humidity levels were successively increased, with a return to 0%RH after each loading. The dwelling time at each humidity level was fixed at 15 min. The SAW devices were incorporated into the oscillating

circuit presented in Sec. 3.4.2 and the frequency was continually monitored for the entire duration of the testing.

4.3 Results and discussion

The impact of a 210 nm thick GLAD film on the response (IL and phase as functions of frequency) is shown in Fig. 4.3. Both the IL and the phase are shifted down in frequency due to the addition of the film on the device. The shape and magnitude of the IL curve also appears to be conserved. While the phase response appears to be mostly conserved, there appears to be some distortion introduced at the frequencies corresponding to the points of maximum IL (low points on the curve) on either side of the main lobe. These are not significant in the operation of the device though, because they occur at the maximum IL and are significantly far away from the operating frequency. A possibility for the source of this distortion could be from small changes in conductivity at the electrode pads, which only show up at points in the signal with the highest losses.

Figs. 4.4 and 4.5 show a summary of the shift in frequency and change in IL, respectively, for the devices with varying thicknesses of GLAD. As seen in Fig. 4.4, as the thickness of the film increases, the operating frequency shifts further downward. This can be associated with the increased mass-loading effect of a thicker film. However, if the GLAD film were acting as a rigid/elastic mass-loading layer, then the change in IL should be independent of GLAD film thickness [46, 120], which was not observed. While films with thicknesses less than 300 nm show negligible impact on the IL, there is a significant increase in IL with the thicker films, suggesting that the film is acting as a viscoelastic

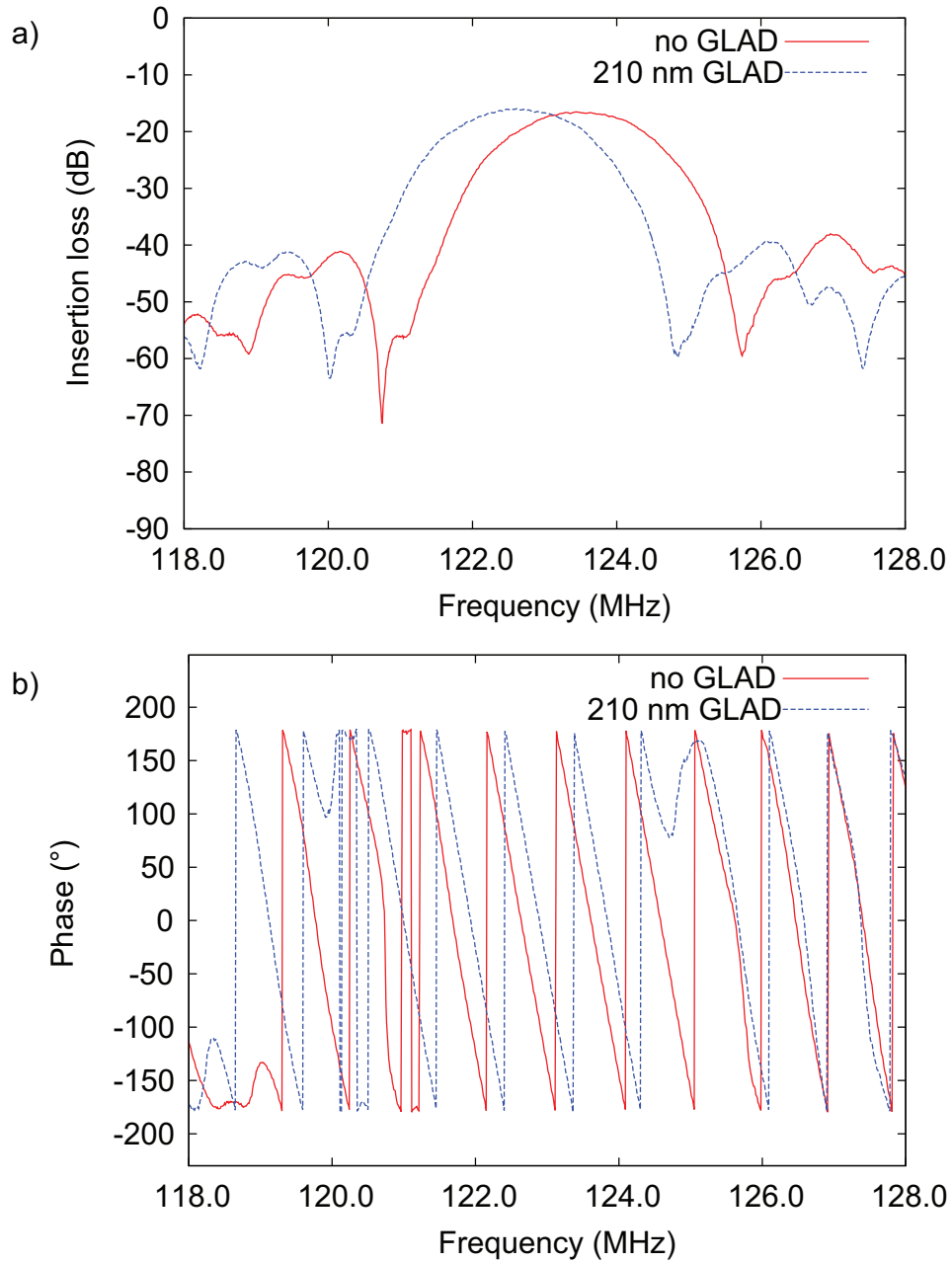


Figure 4.3: The a) insertion loss and b) phase response of a device before and after a 210 nm thick GLAD film has been deposited on top.

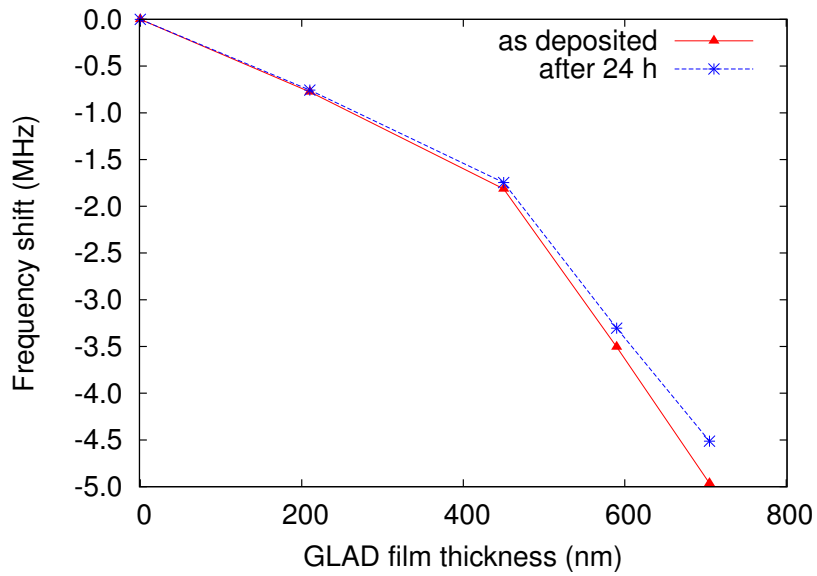


Figure 4.4: Relationship between GLAD film thickness and shift in the operating frequency, as-deposited and after 24 h. Reprinted from [95] with permission from Elsevier.

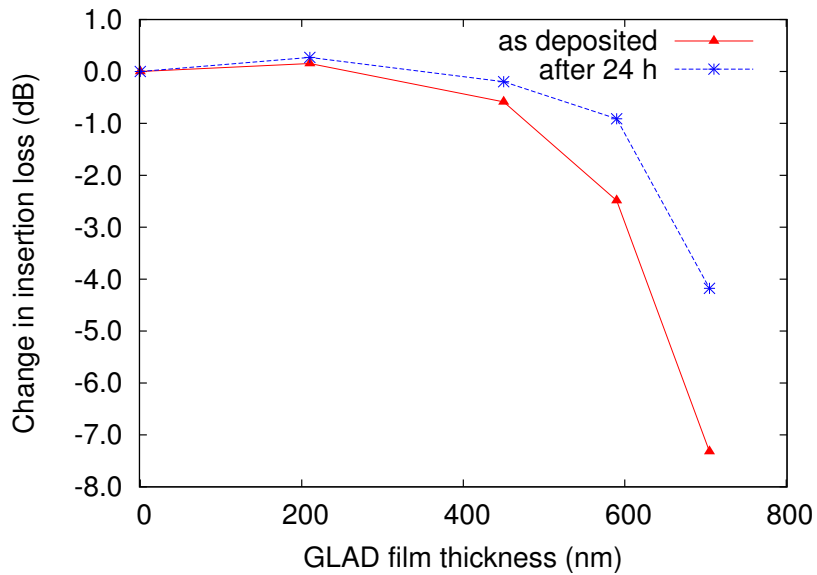


Figure 4.5: Relationship between GLAD film thickness and insertion loss, as-deposited and after 24 h. Reprinted from [95] with permission from Elsevier.

(lossy) layer. Moreover, the thicker films exhibit immediate aging effects, as the responses of the devices were seen to be continually changing upon measurement immediately after film deposition, with an upward shift in operating frequency and decrease in IL. The response of all the devices were thus remeasured 24 h after deposition, and the results are also shown in Figs. 4.4 and 4.5, reflecting the noted trends. This aging effect has not been previously reported for films used for capacitive-based sensors [118]. It is possible that this aging effect is the result of the relaxation of the dense GLAD film. From a literature survey, there has only been a single report on modeling the effects of vertically aligned nanostructures on SAW devices [121], and the modeling is based on Rayleigh-mode SAWs. There is clearly a need for further study to better understand how these nanostructures affect SAW operation, particularly with taller nanostructures.

The sensors were put through RH loadings ranging from 0% to 90%, and were tested 48 h after deposition. Fig. 4.6 shows the time-resolved frequency shifts of devices with varying thicknesses of films for humidities up to 48.3%RH. Higher humidity loadings were omitted from the figure to preserve clarity between the different devices. All devices with GLAD films show significantly increased frequency shifts at any given RH value. The frequency shifts are primarily due to the adsorption of water molecules (mass-loading) onto the surface of the film. Comparison between the varying thicknesses of GLAD films shows that frequency shifts increase with film thickness. This is expected as the surface area increases relatively linearly with thickness [94]. There was no significant increase in baseline oscillation noise due to the addition of GLAD on any of the devices, but there was noticeable noise during testing, as evident in Fig. 4.6. This noise is associated with the GLAD films causing increased

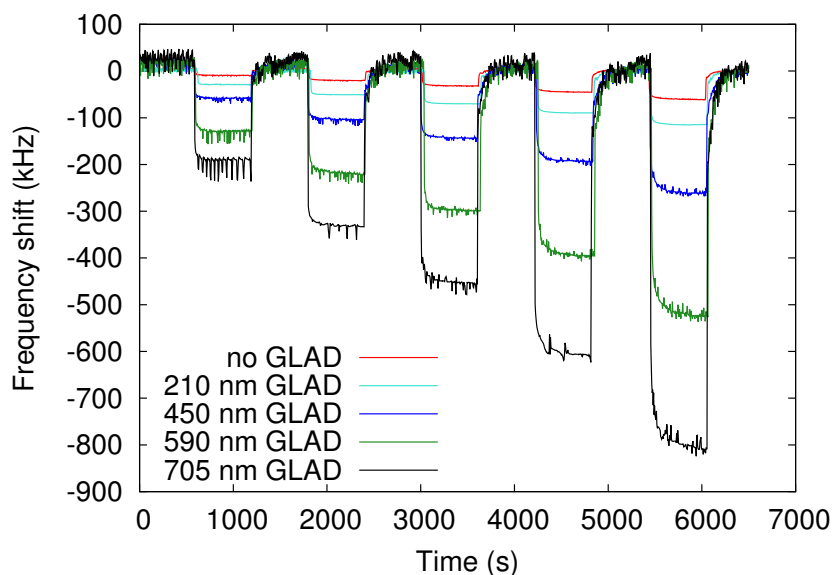


Figure 4.6: Time-resolved response of GLAD-modified SAW sensors to increasing relative humidity loadings of 9.8%, 19.3%, 28.6%, 38.6%, and 48.3%.

sensitivity to pressure. Since the flow of gas was aimed directly onto the device, then any changes in the flow pressure will also be reflected in the frequency recorded by the counter. Whenever any of the devices with a GLAD film was placed in an environment with no significant flow of air, this noise floor was not observed. The most notable noise is seen with the 705 nm thick film at an RH loading of 9.8%. The noise appears to be periodic in nature, but this was not seen in other RH loadings, or in other devices, so this is likely characteristic of the way the film oscillates with the SAW at this RH. The noise for a given film thickness, however, is quite small compared to the actual frequency shifts. Humidity sensors are also often semi-enclosed to prevent contamination and/or damage to the sensor area, and this would also protect from spurious changes in the air flow in the environment. Conversely, this increased sensitivity to dynamic pressure could be utilized as an additional function to provide a measure of the circulation rate of air in the environment,

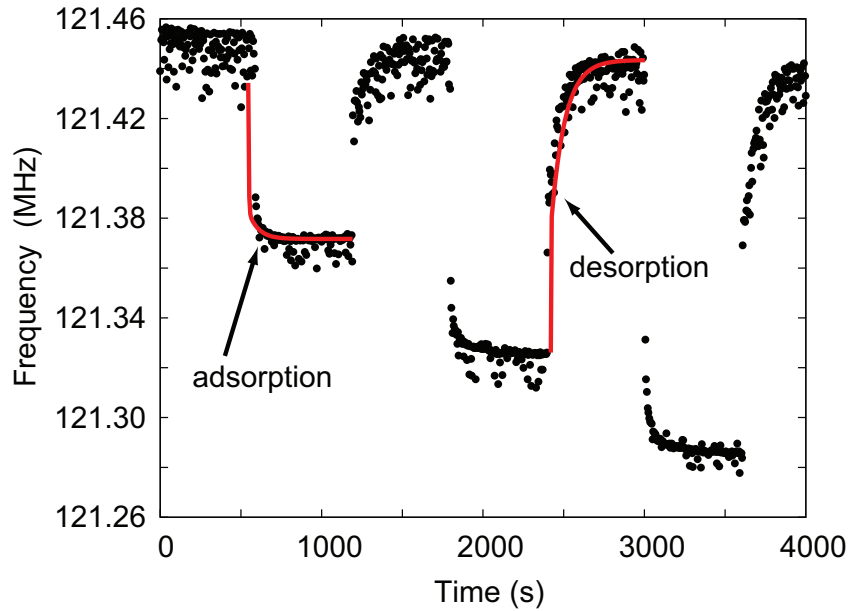


Figure 4.7: Examples of adsorption and desorption curve fitting on the time-resolved frequency data for the SAW device with a 450 nm GLAD film.

e.g., circulation of air in an office.

The magnitude of the frequency shifts were obtained by fitting exponential decays to each of the time-resolved adsorption and desorption curves for each humidity loading. The curves were fit with a function of the form:

$$f(t) = A\exp(-t/\tau) + B\exp(-t/\rho) + C,$$

where A , τ , B , ρ , and C are fitted constants. An example of the fitting is shown in Fig. 4.7. This double exponential function was utilized because it was able to consistently and accurately fit the data. The desorption curves are characteristic of the baseline value, so an average of all fitted values for a given device was taken as the baseline. The frequency shift for a given humidity loading was then obtained by subtracting this baseline from the frequency obtained from the adsorption fit. Fig. 4.8 presents a summary of

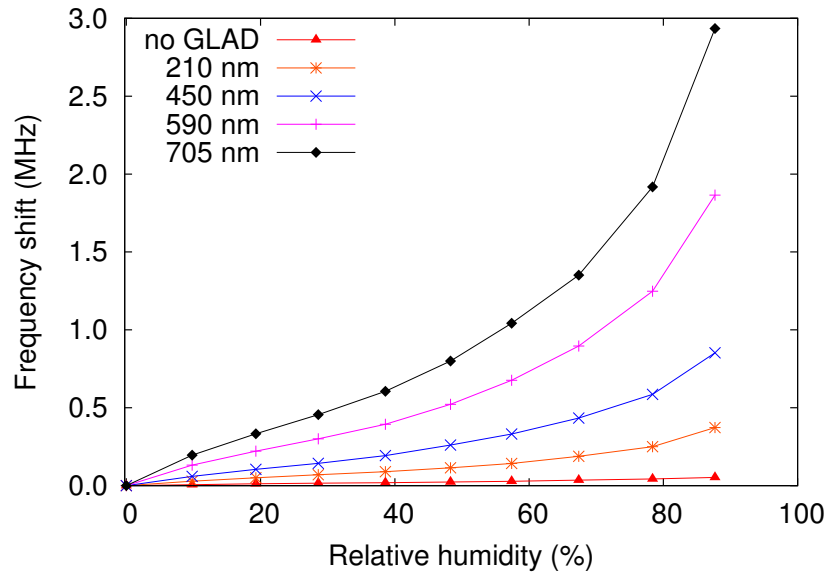


Figure 4.8: Response of GLAD-modified SAW sensors to relative humidity loading. Reprinted from [95] with permission from Elsevier.

the frequency shifts with varying RH for the different thicknesses of GLAD films.

The data in Fig. 4.8 were empirically fit with a fifth order polynomial with only odd-order terms, and sensitivity curves were extracted by differentiating the fit, resulting in Fig. 4.9. While the data appear to follow a type II isotherm [122], it is not accurate to label them as such because the data were not collected as isotherms. Table 4.1 shows the fit parameters for each film thickness. With only 210 nm of GLAD film deposited, the sensitivity is seen to be significantly increased. For example, at 25%RH, the sensitivity increases from 0.50 kHz/%RH (reference device with no GLAD deposited) to 2.28 kHz/%RH. The sensitivity increases significantly to 15.50 kHz/%RH when 705 nm of GLAD film is present, a 30 times increase. Although the surface area increases linearly with film thickness, the sensitivity increases exponentially, suggesting that the increase in surface area from the nanostructured film

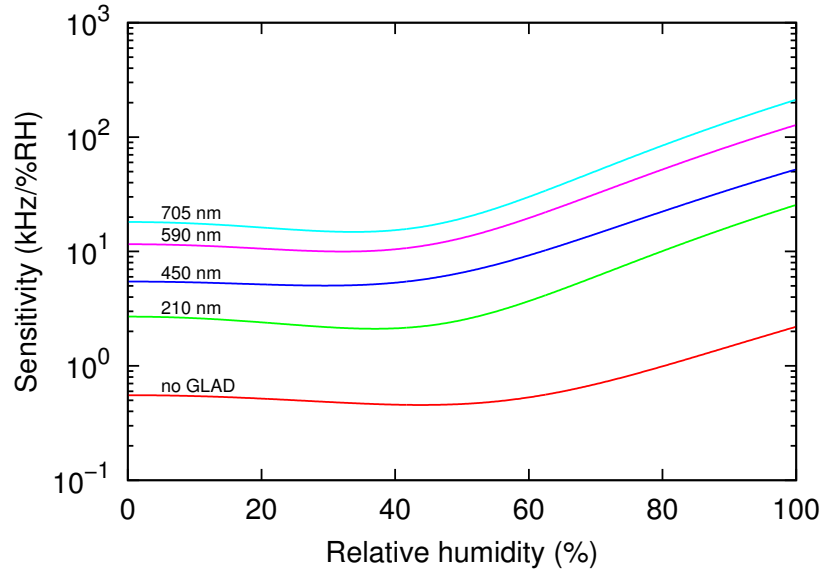


Figure 4.9: Sensitivity curves of SAW sensors to RH with varying thicknesses of GLAD films. Reprinted from [95] with permission from Elsevier.

Thickness (nm)	a_1	a_3	a_5
0	0.0554561	-0.034313	0.0534966
210	0.269531	-0.285656	0.628545
450	0.546083	-0.328609	1.13282
590	1.15769	-1.01665	2.93248
705	1.81054	-1.91357	5.02843

Table 4.1: Fit parameters for data set from Fig. 4.8, following the fit $a_1x + a_3x^3 + a_5x^5$. The frequency unit used in the fit is MHz and the RH is expressed as a fraction rather than a percentage. Reprinted from [95] with permission from Elsevier.

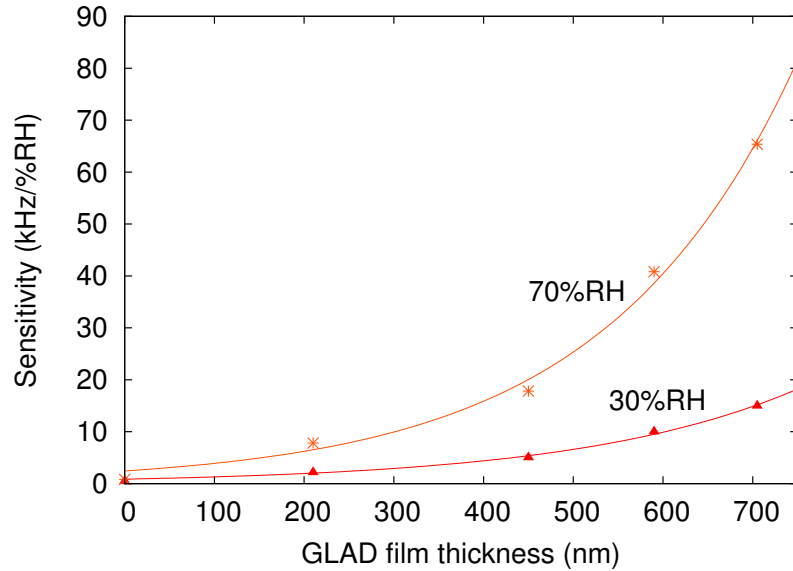


Figure 4.10: Examples of sensitivities with respect to film thickness for different relative humidity loadings, showing the non-linear relation. The lines are exponential fits to the data.

is not the only factor affecting sensitivity. This is illustrated in Fig. 4.10 with two sets of data at different RH loadings. In addition to the increased surface area, taller nanostructures could be more sensitive to surface perturbations, as they are known to also increase radiative losses and scattering [81], particularly when there is a mass loading (in this case, water adsorption). The taller nanostructures could be more effectively coupling the perturbations with the acoustic wave. The increase in sensitivity was significantly more pronounced at higher RH, possibly due to the multilayer formation of the water molecules. At 75%RH, for example, the sensitivity for a bare device was 0.82 kHz/%RH, compared to 65.37 kHz/%RH for a device with 705 nm of GLAD film, an 80 times increase. We hypothesize that using taller nanostructures would further increase sensitivity, but at the cost of increased losses as noted above. While this was not investigated in this thesis, this effectively puts an upper limit on

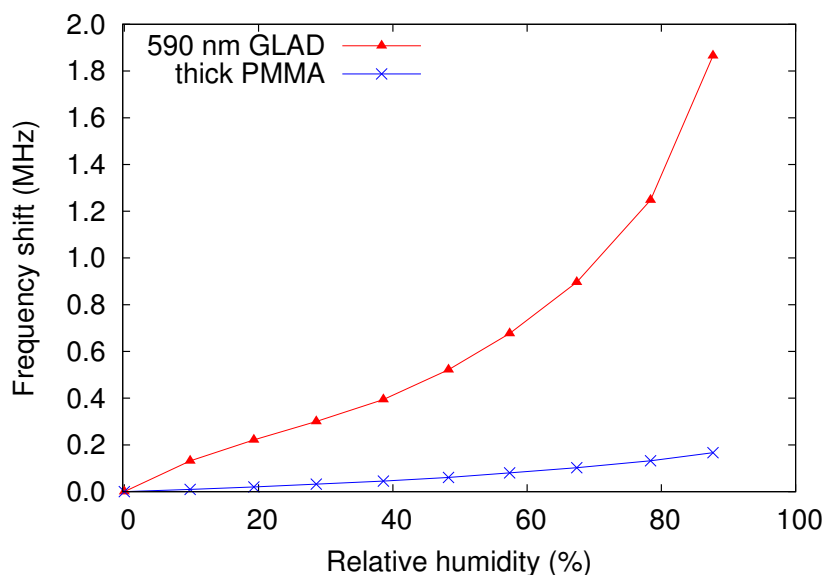


Figure 4.11: Response to humidity of a device with 590 nm GLAD on a thin layer of PMMA and that with no GLAD and a thick layer of PMMA. Both devices operate at about the same frequency. Reprinted from [95] with permission from Elsevier.

the height of nanostructures that can be utilized before the losses begin to affect device performance.

To confirm that the increase in sensitivity was primarily related to surface area and structure, and not to an increase in effective guiding layer thickness [123], another device was fabricated with a thicker layer of PMMA as the waveguiding layer. The thickness of the PMMA layer was $\sim 1.6 \mu\text{m}$ (compared to $\sim 1.1 \mu\text{m}$ as on the nominal devices) and after deposition of the dense 30 nm SiO_2 sensing layer the device had an operating frequency of ~ 120.4 MHz. This operating frequency is just above the operating frequency for the device with a 590 nm GLAD film (~ 120.3 MHz), so that device was used for comparison. Fig. 4.11 compares the response to changes in RH for these two devices. It can be clearly seen that the frequency shifts (and in turn sensitivity) for the device with GLAD significantly exceeds that of the device with a thick guiding layer

across the entire measured RH range. In fact, even though the thicker guiding layer does improve sensitivity over its thinner counterpart, as expected, the sensitivity is still below that of the device with only 210 nm of GLAD film.

Compared to most reported sensitivity values, the sensitivity values obtained are much higher. Literature values are commonly reported in parts-per-million (ppm), which is calculated as the sensitivity (in Hz/%RH) divided by the operating frequency (in MHz). Rimeika *et al.* reported a sensitivity of 110 ppm/%RH, between values of 25–35%RH, with significantly lower sensitivity for RH values between 10–25% [108]. Their devices were among the most sensitive that are reported in the literature. In comparison, the devices here with 705 nm GLAD film had a minimum sensitivity of 125 ppm/%RH at 34%RH. Penza and Cassano had a similar response to our devices, and had sensitivities of 12.4 ppm/%RH at 28%RH and 395 ppm/%RH at 60%RH [97]. While the devices here were able to obtain higher sensitivities at low RH, their devices have a much higher sensitivity at high levels of RH. However, they were using resonator SAW devices as well as operating at much higher frequencies, which is known to increase sensitivity [11].

The response times of the sensors were briefly investigated to determine if the GLAD films had a significant impact on them. Adsorption response times were obtained by letting the sensors stabilize at 0%RH in the chamber, and then quickly removing the chamber lid to allow the sensors to stabilize at the ambient humidity (19%RH at the time). Similarly, the desorption times were achieved by having the sensors stabilize at 78%RH, and then quickly removing the chamber lid to expose them to ambient humidity (24%RH at the time). The frequency was measured at intervals of 1 s, which was the minimum interval allowed by the software. The response times were taken to be

Thickness (nm)	Adsorption time (s)	Desorption time (s)
0	31	40
210	20	23
450	18	24
590	21	26
705	22	34

Table 4.2: Response times for the adsorption and desorption of humidity of SAW devices with GLAD films.

the time it took for the signal to reach 90% of the stabilized value. Table 4.2 shows the response time for the devices with varying GLAD thicknesses. All devices show an improvement in response time with GLAD film present, as expected from the high porosity and surface area provided by GLAD resulting in faster diffusion times of the gas [119]. However, the improvement does not show a clear trend with film thickness. The response times across all GLAD thicknesses are quite comparable, with the exception of the desorption time of the 705 nm thick film. While still faster than the device with no GLAD film present, the desorption time was significantly higher than its thinner counterparts. This is likely due to the decreased diffusion rate resulting from the thicker film, particularly near the device surface (bottom of the films), as the films are quite dense. The film is able to saturate and adsorb the humidity relatively quickly, but the high density makes it difficult for the humidity to escape because the humidity has to travel through more of the film before leaving the device. Overall, the response times are still quite high compared to some other sensor technologies like capacitive-based sensors, which have sub-second response times [76]. However, this is an inherent limitation of the technology, and response times on this order (tens of seconds) may still be more than adequate for the intended application.

Finally, the stability of the sensors was investigated. To test the stability,

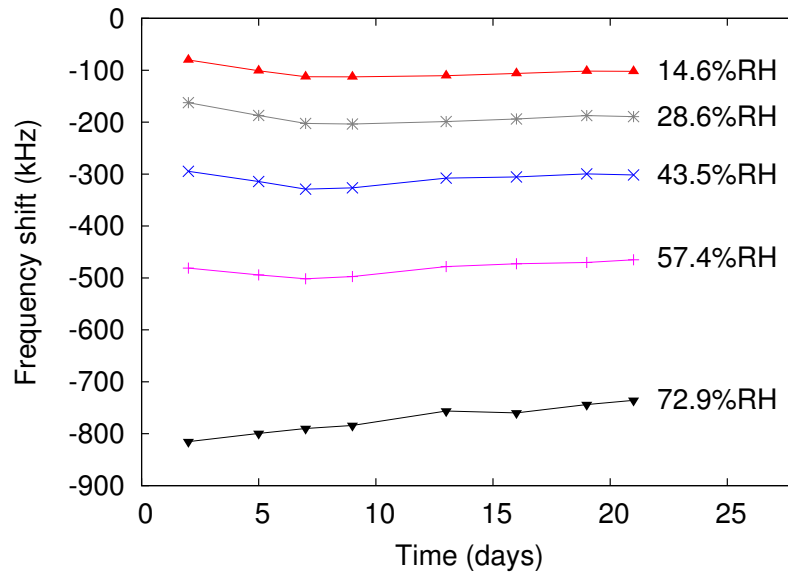


Figure 4.12: Long term stability of a device with 500 nm GLAD stored in open air over 21 days. Reprinted from [95] with permission from Elsevier.

a device with 500 nm of GLAD was fabricated and then tested over of 21 days. After each test, the device was stored in open air at room temperature. As seen in Fig. 4.12, the device showed relatively good stability at each of the tested humidities, for a first time experimental testing environment. In order for these devices to become commercial-grade sensors, higher stability will be required.

4.4 Summary

This work presents the first use of GLAD on SAW sensors. Dense, high surface area, nanostructured SiO₂ thin films fabricated by GLAD onto SAW devices were studied and shown to significantly improve the performance as a humidity sensor. Increasing thicknesses of GLAD films were shown to cause a decrease in the operating frequency and increase in the IL. This was accompanied with

exponential increases in the sensitivity to humidity over the range 0–90%RH. The thickest film deposited was 705 nm, and produced one of the highest sensitivities that have been reported. The GLAD films also improved response times of the SAW devices, and showed good long term stability. The increased surface area played an important role in the sensitivity enhancement, but it was shown to not be the only factor responsible. It is suspected that the structure and morphology are also important, motivating further investigations and modeling studies to better understand the mechanisms involved.

Chapter 5

Development of GLAD

nanostructures suitable for use in liquid environments¹

5.1 Introduction

The integration of high surface area nanostructures with existing technologies is an attractive field of study. In addition to SAW sensors, their ability to provide a high surface area with minimal change in the planar dimensions of the device has found use in a variety of other applications such as solar cells [16, 73, 125, 126], superhydrophobic surfaces [17, 18, 127], and other sensor platforms [19, 128–130]. However, in applications where high aspect ratio nanostructures, such as those grown by GLAD, are in contact with a liquid, these nanostructures have been reported to deform or cluster together due to capillary forces from the liquid acting on them [16–21]. This is a

¹A version of portions of this chapter (discussing ion-milling and FT image analysis) has been published in Nanotechnology [124].

serious problem for sensing applications involving liquid environments as the clustering reduces the accessible surface area and introduces issues regarding the reproducibility, longevity, and accuracy of the sensor. In the case of GLAD nanostructures, Rao and Zhang had even suggested that the application of GLAD nanostructures may be limited to dry environments as a result of their tendency to cluster [14].

Fan *et al.* have studied clustering for Si nanorods grown by GLAD in detail [20, 21, 131, 132]. They also showed that the clustering, which they refer to as the “nanocarpet effect”, can be prevented by capping the nanorods [21]. This increased the size of the tips of the nanorods at the top and in the channels, reducing the available bending distance of the nanorods and providing additional mechanical support for neighboring nanorods, respectively. While clustering of the nanorods was prevented, there was significant loss in porosity, particularly through the top surface of the film, hence reducing the accessible surface area. On the other hand, Anandan *et al.* were able to produce high aspect ratio gold and silver nanopillars that did not deform using an electrodeposition technique [19]. They found that the deflection of the nanopillars due to capillary forces is proportional to the aspect ratio to the third power, where the aspect ratio is defined as the ratio of the length of the nanopillars to their diameter.

In this chapter, the use of ion-milling to eliminate the clustering effect in vertical post nanostructures grown by GLAD is presented. Brief introductions on the Fourier transform image analysis technique and chemical functionalization of surfaces are first provided. Solution and vapor-phase chemical functionalization of GLAD films were investigated, with the vapor-phase method shown to be more effective at modifying the films. The effects of ion-milling

on the structure and morphology of the vertical posts and their relation to the clustering are then reported. It is shown that that clustering of these structures is eliminated with sufficient ion-mill exposure time. The accessibility of the surface area after the ion-milling process was investigated by chemically functionalizing the films and immobilizing gold nanoparticles on the functionalized nanostructures. The results shown here make films promising for integration with sensing technologies, such as SAW sensors, involving liquid media.

5.2 Fourier transform image analysis

The Fourier transform (FT) is a mathematical tool for transforming a function in one domain into another. In the case of continuous 2D images, the FT is an operation that transforms the spatial information of the image into its spatial frequency components. For an image in the spatial domain defined by $f(x, y)$, which is the pixel intensity as a function of position (x, y) , the FT is defined as

$$F(u, v) = \int_{-\infty}^{+\infty} \int_{-\infty}^{+\infty} f(x, y) e^{-i2\pi xu} e^{-i2\pi yv} dx dy \quad (5.1)$$

where $F(u, v)$ is the transformed image in the spatial frequency domain [133]. For a digital 2D image with a discrete number of points ($N \times M$ pixel image), Equation (5.1) can be transformed into

$$F(u, v) = \frac{1}{NM} \sum_{x=0}^{N-1} \sum_{y=0}^{M-1} f(x, y) e^{-i2\pi xu/N} e^{-i2\pi yv/M} \quad (5.2)$$

where all the variables (x, y, u, v) are now discrete integer values. The highest frequency components in each direction are $u = \pm \frac{N}{2}$ and $v = \pm \frac{M}{2}$, which is

the equivalent of a resolution of 2 pixels in length [134].

The spatial frequency in an image represents how rapidly or slowly the brightness level of neighboring pixels is changing. For example, the higher the spatial frequency along a particular direction, the greater the change in brightness levels between neighboring pixels will be. Thus, by examining the 2D FT of an image, it is possible to extract information regarding regularity and patterns with their respective directions. This analysis has already been applied to GLAD thin films to analyze the dominant spacing between columns. In Zhao *et al.*'s studies, they showed that the Fourier transform of top-down SEM images resulted in a diffuse ring structure, indicating that there was a homogeneous characteristic length in the surface pattern with no directional dependency. The circularly averaged power spectra with respect to spatial frequency was computed and the peak of the data (the dominant spatial frequency) was taken as the average column distance. They used this analysis as a metric for characterizing the deformation of the GLAD nanostructure after wetting [20, 21, 131]. Buzea *et al.* also used this same analysis to characterize the growth mechanisms and film morphologies of silicon films grown using GLAD [135].

5.3 Tailoring the chemistry of surfaces

Chemical functionalization of silicon-based surfaces has become an increasingly popular area of study. In particular, the application and formation self-assembled monolayers (SAMs) on smooth surfaces have been widely studied. Originally introduced by Netzer and Sagiv [136], SAMs have found application in many technologies such as enzyme [137] and DNA [138] immobilization

and anti-stiction coatings in MEMS technology [139]. Hence, to maximize the functionality of SAMs, there has been considerable research into developing processes to produce the most uniform and functional SAMs.

SAMs can only be formed with select precursor molecules. The molecule must be able to attach strongly to the surface while also exposing terminal functionality to the external environment. The molecule can be divided into three parts: the head group, the chain group, and the tail group. The head group is responsible for chemisorption to the surface through the formation of strong bond(s). For the purposes of silicon-based surfaces (*e.g.*, silicon, glass, quartz, *etc.*), this is usually a strong covalent Si–O–Si bond whereby the head group is a silane, often an alkoxy silane ($-\text{Si}(\text{OC}_n\text{H}_{2n+1})_3$) or chlorosilane ($-\text{SiCl}_3$). This bond formation with the surface is also the most exothermic process and as a result, the molecules will attempt to occupy all available sites. This maximizes packing density through surface mobility and hence self-assembly [140]. The chain group is most commonly an alkyl chain and acts as the link between the head and tail groups. An alkyl chain can vary from a few carbon links to greater than ten. The chain length can influence the packing density of the precursor on the surface, with longer chains decreasing the packing density (depending on deposition conditions). The final part of the precursor molecule is the tail group, which provides the SAM's functionality. The choice of group is dependent on the desired application and examples include a methyl group ($-\text{CH}_3$), an amine group ($-\text{NH}_2$), or a fluorine atom ($-\text{F}$). Fig. 5.1 shows some common precursor molecules used in the formation of SAMs.

In practice it is very difficult to actually obtain a monolayer, and equally difficult to prove that there is in fact a monolayer. Tailoring the chemistry of

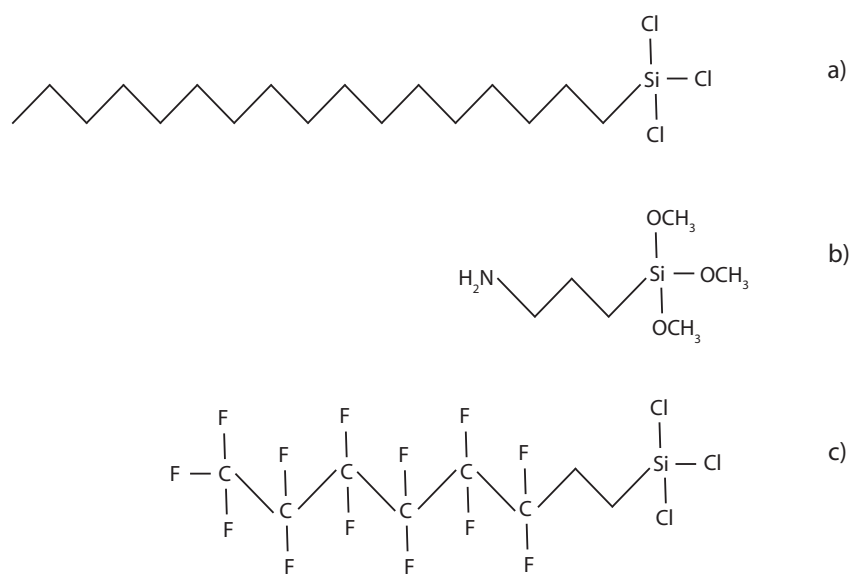


Figure 5.1: Common SAM precursor molecules. a) octadecyltrichlorosilane b) 3-aminopropyltrimethoxysilane c) tridecafluoro-1,1,2,2-tetrahydrooctyltrichlorosilane

nanostructured surfaces is even more difficult because the structures often do not have smooth surfaces, and their morphology makes characterization even more difficult. Thus, though the desired application and fabrication process may be the same, chemical functionalization of nanostructured surfaces do not necessarily constitute as SAMs, and will not be referred to as SAMs in this thesis.

5.4 Experimental

5.4.1 Sample fabrication

As in the previous chapter, SiO₂ vertical post nanostructured thin films were prepared using GLAD as per the procedure described in Sec. 3.3.2. GLAD films were deposited at an angle of 86° relative to the substrate normal onto p-type Si(100) substrates. At this angle, films are known to have well-separated

structures that are also known to cluster after exposure to a liquid. The deposition rate was kept in the range of 1.3–1.8 nm/s, as measured by the CTM, and films were grown to thicknesses of approximately 550, 900, 1200, and 1600 nm.

Ion-milling was carried out using an Ionfab 300 Plus (Oxford Instruments) at the University of Alberta NanoFab. Samples were milled for varying times (0.5, 1.0, 2.0, 3.0 min) at normal incidence relative to the substrate surface, with a beam voltage of 950 V at a current of 120 mA over an area with a diameter of ≈ 14 cm. The substrate holder was rotated at 20 rpm during milling to maximize ion-beam exposure uniformity on the substrates.

5.4.2 Chemical functionalization

The amine ($-\text{NH}_2$) functional group is of importance and interest in medical and biological studies for its excellent biocompatibility and ability to interact with many biochemical species. As such, ion-milled GLAD films were chemically functionalized with an amino-terminated precursor molecule (3-aminopropyltrimethoxysilane or APS). A dual-manifold Schlenk line was utilized so that the functionalization atmosphere (N_2 or vacuum) could be readily controlled. Functionalization was initially carried out using both solution- and vapor-phase methods. A strictly anhydrous environment was used following the results in the literature [141]. This was achieved by drying glassware in an oven immediately prior to functionalization, and distilling toluene (the solvent) over sodium to dry it. Prior to functionalization, the films were cleaned using reactive-ion etching (RIE) using O_2 plasma (80% oxygen flow) for 90 s, under a pressure of 150 mTorr and an RF power of 75%. In addition to cleaning the surface, the RIE etch is also responsible for hydroxylating the surface,

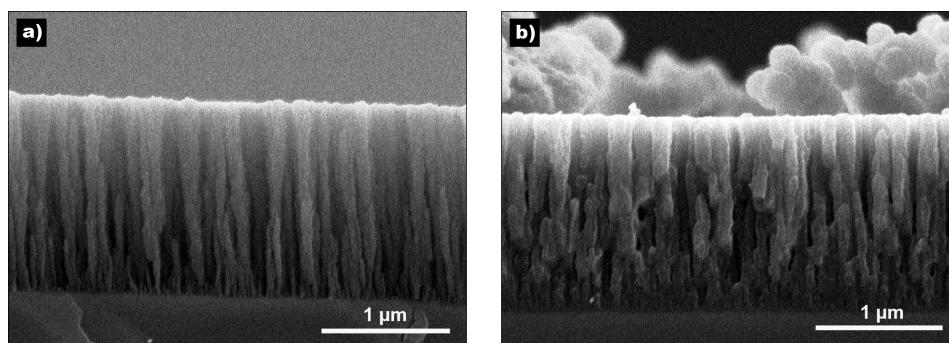


Figure 5.2: SEM images of a) an unmodified GLAD film and b) GLAD film solution-phase functionalized with APS

a key requirement of the functionalization process.

Unmodified GLAD films were originally used in early solution-phase functionalization trials. A 20 mM solution of APS in anhydrous toluene was made and cleaned samples were placed in the solution for 24 h under a nitrogen environment. The samples were then rinsed with anhydrous toluene and placed in an oven at 150 °C overnight to remove any loosely bound APS molecules. SEM imaging of the samples (Fig. 5.2) showed that there was a significant change in the structure of the GLAD film after functionalization as well as significant aggregation of the APS molecules on the surface of the film. To eliminate this effect the concentration and reaction times were reduced, but this only served to reduce the observed effects, as the structure was still visibly altered. This was largely attributed to the difficulty in keeping the materials dry, as it has already been noted that water can have a large effect on the functionalization results.

A less cumbersome vapor-phase method was then investigated and used. In this method, 0.2 mL of pure APS was placed in a small vial inside a desiccator with samples facing upwards. The pressure inside the desiccator was then reduced via a rotary roughing pump (actual pressure was not measured) and

the samples were left for 2 h. Samples were then rinsed with acetone and placed in an oven at 150°C overnight (over 10 hours). Unlike the samples functionalized with the solution-phase method, the vapor-phase method did not appear to visibly alter the structure of the film. As a result, this vapor-phase method was utilized in this chapter.

5.4.3 Characterization

To investigate the extent of clustering of these films, samples were immersed in de-ionized water for 60 s and then gently removed. The samples were allowed to dry completely at room temperature before any analysis was conducted. All samples were sputter-coated with Cr and analyzed using SEM. Top-down SEM images were taken to analyze the extent of clustering. However, visual inspection provides only a qualitative means of comparison of the amount of clustering and how it differs due to effects of ion-milling exposure time or film thickness. Using FT image analysis allows for a well-defined, systematic method to quantify the amount of clustering and make comparisons between samples. As a result, the acquired images were analyzed with FT image analysis in MATLAB to quantitatively describe the level of clustering. During image acquisition, the contrast and brightness of the images were adjusted visually to optimize structure separation from the background, and were not further altered for the FT analysis. The magnification for each film thickness was chosen to ensure that a significant number of columns (~ 400) were captured in the image while also avoiding aliasing in the FT analysis, both which have previously been noted by Buzea *et al.* [135].

Chemical characterization of the functionalized films was conducted with X-ray photoelectron spectroscopy (XPS), Auger electron spectroscopy (AES)

and Fourier transform infrared spectroscopy (FTIR). However, the only tool that was able to provide any useful analysis was XPS. The small scanning beam of AES was intended to scan for nitrogen along the length of the vertical posts, but the difficulty of imaging and scanning due to charging of the film (SiO_2 is an insulator) combined with the low concentration of nitrogen resulted in no detected nitrogen. This was also true with FTIR, which would have shown 2 small peaks around $3400\text{-}3500\text{ cm}^{-1}$, corresponding to the N-H bending of primary amines. Instead there was no discernable signal to indicate the existence of any amines on the surface of the film. On the other hand, a surface scan using XPS was able to detect nitrogen and a larger carbon signal at the surface of the film and was thus utilized as the main characterization tool. It should be noted, though, that XPS provides no additional information regarding the uniformity of the coating, accessibility of the terminal amine groups, or the extent of functionalization because of the relatively poor spatial resolution of XPS and its inability to probe any deeper than $<10\text{ nm}$ into the film.

To gain a more thorough chemical analysis of the film, an indirect method was used. It has been known that amines have an affinity to gold, similar to but not quite as strong as thiols and gold [142–145]. Thus by reacting the functionalized films with gold nanoparticles (AuNPs), the nanoparticles should adhere to film wherever terminal, reactive amines are present. The distribution of particles across the film and along the structures would provide a qualitative analysis of the quality of the chemically functionalized film. Colloidal AuNPs with an average diameter of 20 nm were purchased from Sigma-Aldrich and used as-is. The AuNPs were uncoated, negatively charged, and suspended in phosphate-buffered-saline solution to prevent aggregation. Samples of sizes

approximately 1 cm x 1 cm were placed in 1 mL of the AuNP solution and left for 24 h at room temperature followed by rinsing with deionized (DI) water. The samples were then imaged with SEM.

5.5 Results and discussion

The physical effects of ion-milling on the film structure and its effects on clustering are shown in Fig. 5.3. The cross-sectional images (left column) show that ion-milling has the effect of shortening the vertical posts at a rate of ~ 90 nm/min while gradually increasing the diameter of the posts at the base. The latter effect is evident when comparing the as-deposited film (Fig. 5.3a with the film after 3.0 min ion-milling (Fig. 5.3m). The widening of the post bases also occurs more quickly for thinner films. An example of this can be seen in Fig. 5.4, which shows high resolution images of the 550 nm thick film as-deposited and after ion-milling for 0.5 min. This is in contrast to the visibly similar images of Figs. 5.3a and d, which show the 1600 nm film as-deposited and after ion-milling for 0.5 min, respectively.

The effect on clustering is shown through the series of top-down SEM images of the 1600 nm film, before and after water treatment (Fig. 5.3, second and third columns, respectively), as deposited and for various ion-milling times. As-deposited films exhibit clustering (Fig. 5.3c vs. b) as reported before [20], but after even 0.5 min of milling, there is a visible reduction in clustering (Fig. 5.3f vs. c). After 1.0 min of ion-milling (Fig. 5.3h and i), it becomes difficult to visually differentiate between the films before and after the water exposure.

To provide a more well-defined, quantitative, and reproducible analysis of

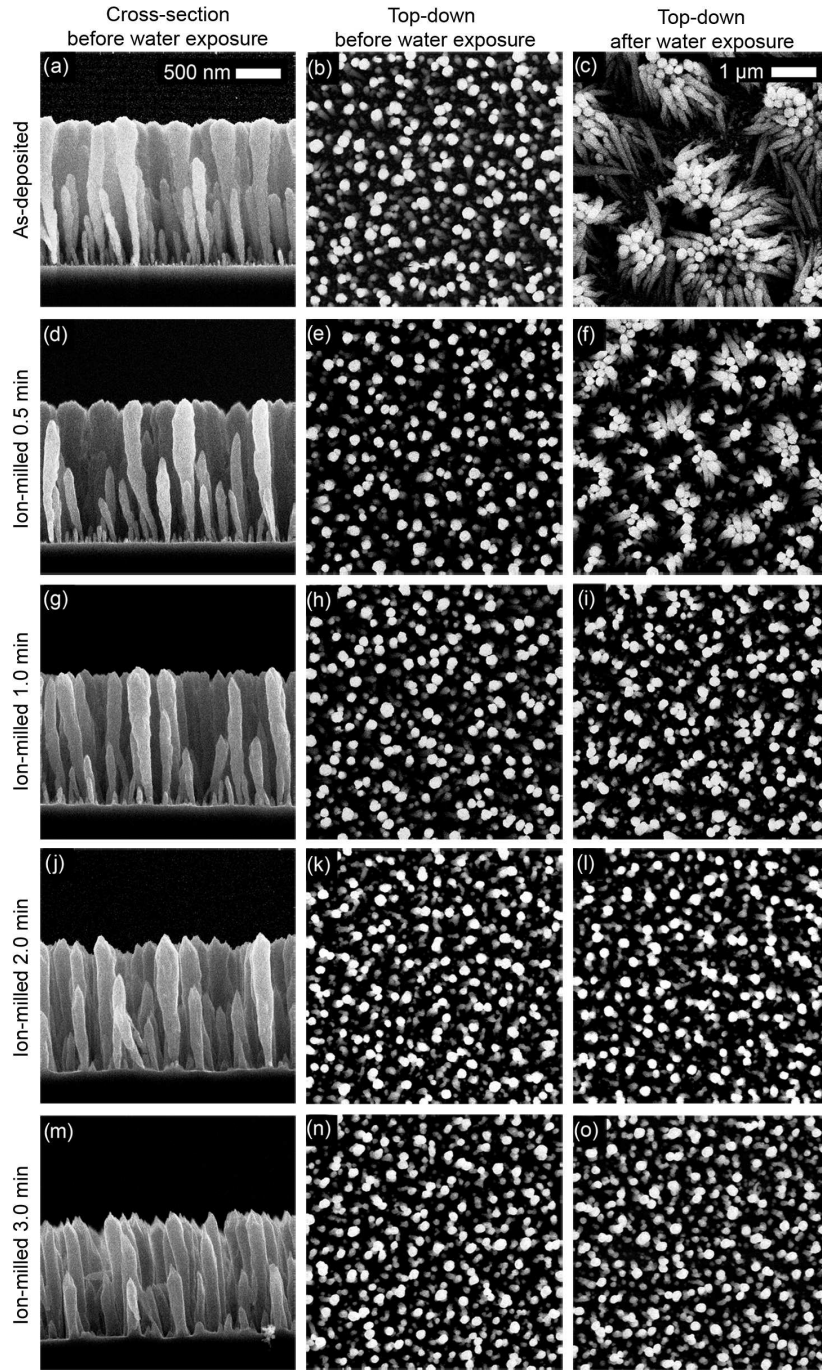


Figure 5.3: Cross-sectional (first column) and top-down SEM images of 1600 nm films before water treatment (second column), and after water treatment (third column). Scale bars are applicable to their respective views. Reproduced from [124] with permission from IOP Publishing Ltd.

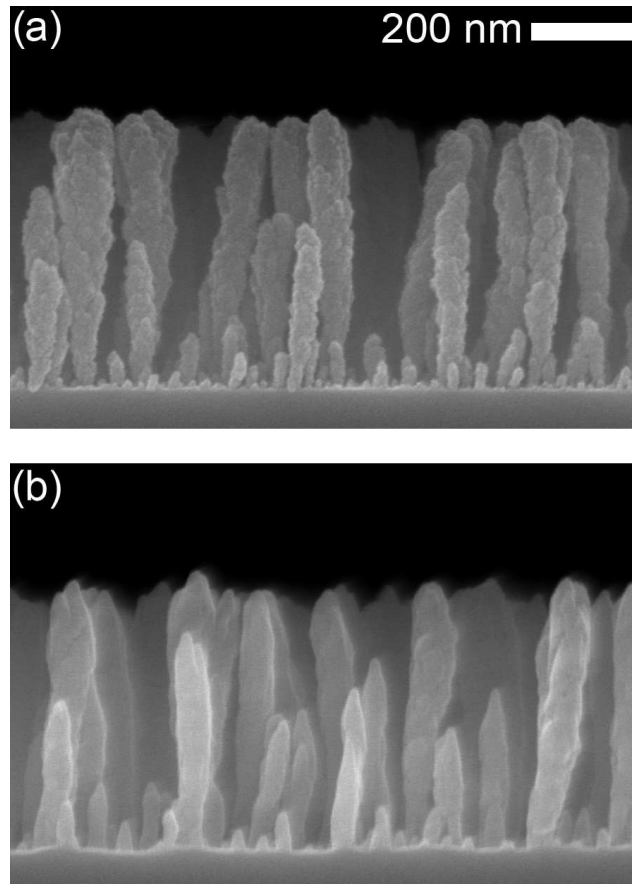


Figure 5.4: Cross-sectional SEM images of a 550 nm film (a) before ion-milling and (b) after 0.5 min of ion-milling. Reproduced from [124] with permission from IOP Publishing Ltd.

the extent of clustering, the top-down SEM images were evaluated by examining their FT magnitude spectra. An example of this can be seen in Fig. 5.5a and b. The magnitude spectra is a diffuse ring structure, which indicates that there is a dominant spatial frequency present in the image with no directional dependency [20, 135]. This diffuse ring structure was observed for all analyzed images.

Taking a radial average yields a graph of intensity versus spatial frequency, *i.e.*, the probability distribution function of the spatial frequency, shown in Fig. 5.5c. While the FT gives the spatial frequency in terms of units of inverse pixels (px^{-1}), this can be converted to units of inverse length knowing the magnification (by making use of the scale bar) from the original SEM image. The dominant spatial frequency can then be determined by fitting the peak of this curve. A 3rd order polynomial was fit to the curves in MATLAB to determine the position of the peak. The dominant center-to-center spacing between objects in the image can then be found by taking the inverse of the dominant spatial frequency. For the case where the film has not been exposed to water, the objects seen by the FT are the individual vertical post nanostructures and the dominant spacing (DS) extracted is a measure of nearest neighbor spacing. When the posts are clustered, the objects become the clusters of posts and the dominant spacing becomes a measure of the spacing between neighboring clusters, which would be larger than the original inter-post spacings. Five SEM images were taken at random spots for each sample, and the average and standard deviation of the dominant spacings were taken to obtain a statistical measure of the error. The reported change in DS is found from subtracting the DS values ($\Delta DS = DS_{\text{after}} - DS_{\text{before}}$). Lower magnification SEM images were used in the analysis of some of the clustered films because the spacings

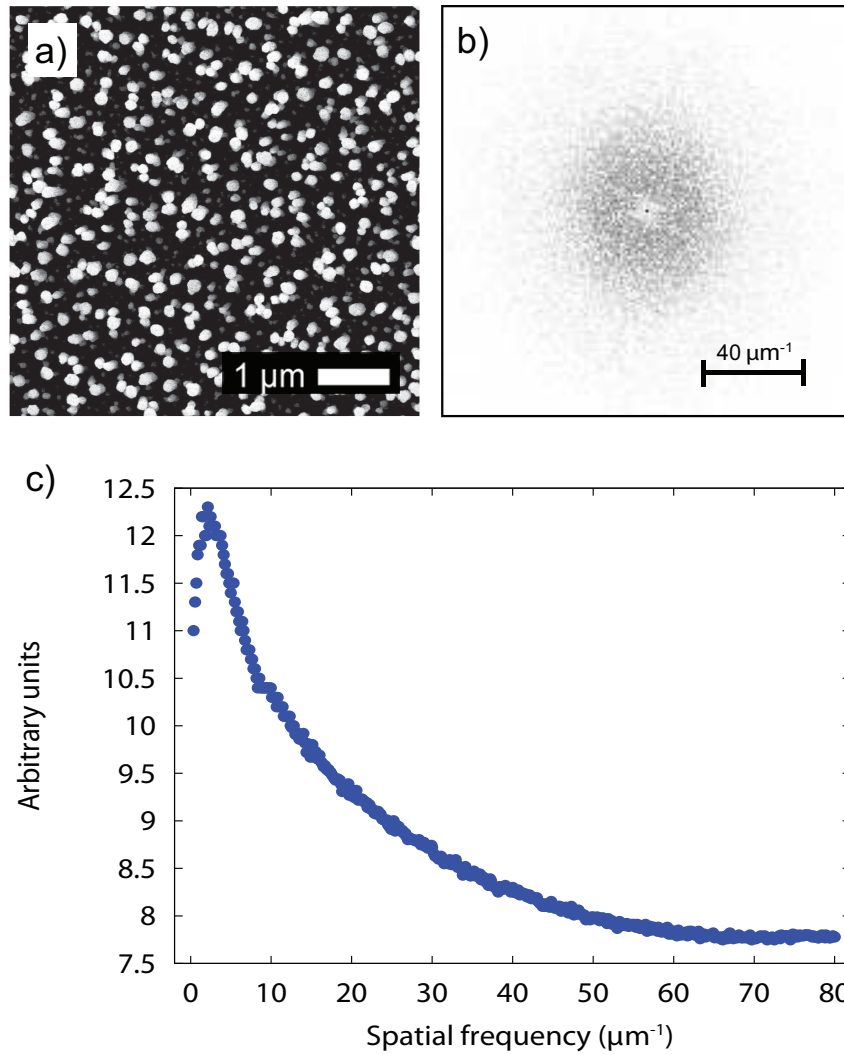


Figure 5.5: An example of a) a top-down SEM image of one of the GLAD films, b) its Fourier transform, and c) the radial average of the Fourier intensity profile. Reproduced from [124] with permission from IOP Publishing Ltd.

between the clusters approach the size of the image. In those cases, there is an insufficient number of clusters in the image to produce a well defined frequency peak that is representative of the local inter-cluster spacings.

The difference in dominant spacings from before and after water treatment, ΔDS , is plotted as a function of ion-milling time in Fig. 5.6. The data is fit with exponential functions of the form $\Delta DS = C \exp(-t_{im}/\tau)$, where C is a constant, t_{im} is ion-mill exposure time and τ is the clustering decay constant. It can be seen that there is a rapid decrease in clustering with ion-mill exposure time. By 2.0 min, $\Delta DS \approx 0$ for all thicknesses tested, consistent with visual estimations that show that clustering is eliminated.

The results also show a clear dependence of the size of clustering (which is related to and less than the dominant spacing) on the original thickness of the films, where thinner films become resistant to clustering more quickly. This can be verified by plotting the relationship between the decay constant τ and film thickness h , as shown in Fig. 5.7. A linear fit to this data ($\tau = ah + b$) supports that the decay constant correlates with thickness, to a first degree approximation.

To gain insight as to why ion-milling increases resistance to clustering, it is essential to first understand the immediate consequences of ion-milling these nanostructured films. Ion-milling causes sputtering of the film material from the exposed surfaces, primarily at the tops of the columns. Some material is sputtered away from the sample, contributing to a net loss of film material, but some sputtered film material is redeposited further down the sides of the columns, with some fraction that reaches the very bottom of the film. This results in the widening of the bases of the nanostructures. By modelling the vertical post nanostructure as a cantilever, Euler-Bernoulli theory can be

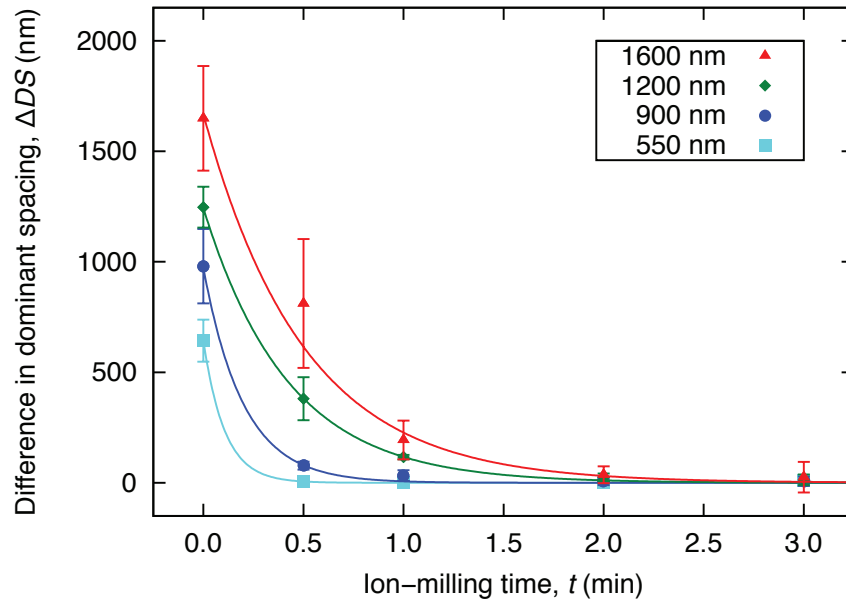


Figure 5.6: Plot of the change in dominant spacing after water treatment as a function of ion-milling time for films of varying thicknesses, as extracted from Fourier transform analysis of the top-down SEM images. Data points are from the experiment, with error bars showing 1σ values. (Note that error bars are smaller than datapoint symbols for 900 nm and 550 nm film sets for ion milling times ≥ 0.5 min.) Solid lines are a decaying exponential fit to the data (detailed in text). Reproduced from [124] with permission from IOP Publishing Ltd.

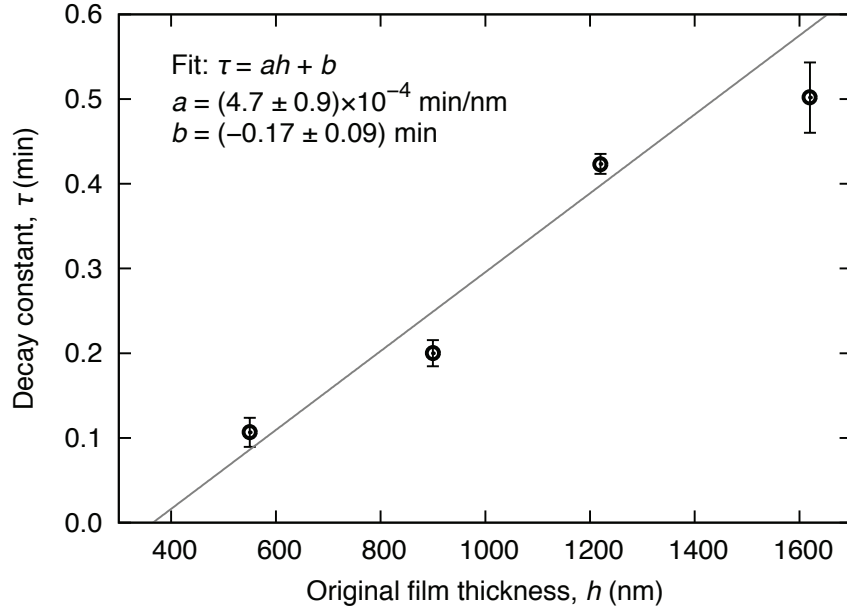


Figure 5.7: Plot of decay constant τ vs. measured film thickness h . Data points (and error bars) are τ values (and 1σ uncertainties) obtained from curve fits from Fig. 5.6. Solid line is linear best-fit to the data. Reproduced from [124] with permission from IOP Publishing Ltd.

applied to understand the dependence of the elastic properties on the base diameter [146, 147]. By combining the power-law scaling of the diameter of nanostructures grown by GLAD [135, 148, 149] ($D \propto h^\xi$), with Euler-Bernoulli theory, Mon [147] derived a relation describing the deflection of the tips of the posts for $\xi = 0.3$. By assuming the base of the post to be circular with radius r_1 , and including the effect of nanopillar tip radius, r_2 , on the capillary force [150], it can be shown that Mon's equation becomes:

$$y(h) \propto \frac{50 r_2 h^{1.8}}{9 E r_1^4}, \quad (5.3)$$

where y is the post deflection at the tip, and E is Young's modulus of the material. A schematic of this configuration is shown in Fig. 5.8. It should be noted that the exponent for the height dependence approaches 3 (ξ approaches

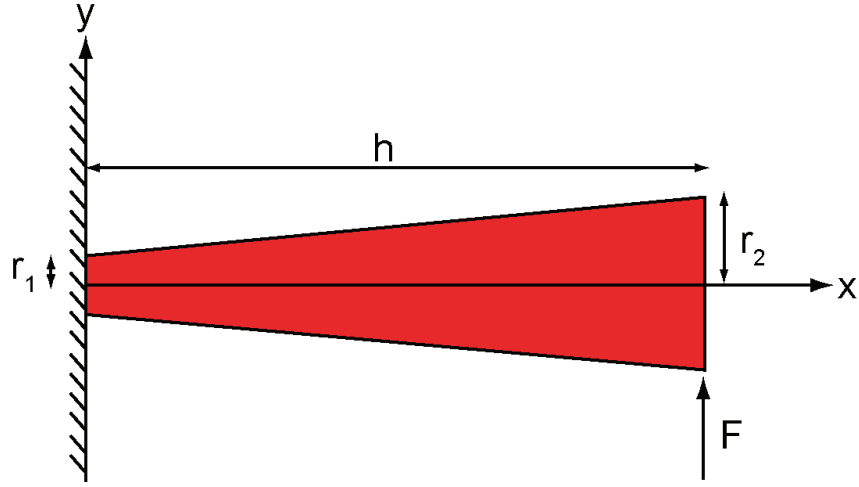


Figure 5.8: Sketch of the inverted frustrum in a singly-clamped cantilever configuration.

0) as the posts become more uniform in diameter. Thus, the post bending distance depends strongly on the radius of the base (r_1) and the height of the post (h). A quantitative understanding of the significance of the post dimensions can be obtained by taking the ratio of the deflection of a post from an as-deposited film to that from an ion-milled film. By using estimates of $h \approx 1600$ nm, $r_1 \approx 20$ nm from Fig. 5.3a and $h \approx 1505$ nm, $r_1 \approx 25$ nm from Fig. 5.3d (the same film after 0.5 min of ion-milling), the ratio of the two deflections is given as $y_{\text{as-deposited}}/y_{\text{ion-milled}} = 2.19$. Hence, even a small increase in the base diameter of 5 nm and reduction in height of 45 nm has a significant impact on the deflection distance and hence the ability of the nanostructures to resist clustering. This is also in agreement with the experimental results where ion-milling of thinner films increases the diameter of the base more quickly, resulting in the observed trend in Fig. 5.6. This result is attributed to the shorter distance and reduced obstruction between the tips of the posts and the bases of neighboring posts.

While we attribute the dominant effect to microstructure-related mechan-

ical changes, other effects will also alter the clustering. Ion-milling is also an energetic process that promotes film smoothing upon resputtering [151]. Wenzel had shown that a rough surface will enhance its hydrophobicity or hydrophilicity by the roughness factor r , defined as ratio of the actual surface area to the geometric surface area [152]. The as-deposited vertical posts have a rough surface as seen in Fig. 5.3a and Fig. 5.4a. This level of roughness has also been imaged at a higher magnification by transmission electron microscopy by Steele *et al.* [153]. Thus, the contact angle on the as-deposited posts is expected to be much less than if the posts were smooth, since SiO₂ is inherently hydrophilic. The series of cross-sectional images in Fig. 5.3, and Fig. 5.4b show that the surface of the posts becomes increasingly smooth with increased ion-milling time, which is expected to cause the contact angle to increase. (We point out here that the contact angle in question is that between the side of a column and the water meniscus, rather than that of a water droplet on top of the columns.) Chandra and Yang [154] recently reported that the capillary meniscus interaction force was responsible for clustering of micropillar arrays and in this context is given as

$$F_c = -\frac{\pi\gamma r_2 \cos^2 \theta}{\sqrt{(\delta/2r_2)^2 - 1}}, \quad (5.4)$$

where γ , θ and δ are the surface tension, contact angle, and inter-pillar distance respectively. Eq. 5.4 states that the smaller the contact angle θ , the larger the force on the pillar; thus, since ion-milling is expected to increase the contact angle, it is also expected to decrease the capillary force.

Finally, as ion-milling is a method of sputtering, it is thus known to increase the density of the film material [155]. In this case, this higher den-

sity material would be found on the surface of the nanostructures, which we hypothesize causes the effective Young's modulus to increase, which in turn further strengthens the columns (Eq. 5.3).

In summary, ion-milling of the vertical post nanostructures produces the following changes:

- thickening of the base of the structures through re-deposition of film material, coupled with a slight overall decrease in film height
- smoothening of the surface of the pillars
- an overall densification of the column, particularly the re-deposited material

As discussed above, all of these changes serve to render the nanostructures more mechanically robust.

The accessibility of the surface area of ion-milled GLAD films was investigated by functionalizing them with APS and exposing them to AuNPs. Fig. 5.9 compares the XPS surface scan of a film that was not functionalized with one that was. The functionalized film has a significantly larger carbon peak and a clear nitrogen peak, which are indicative of the presence of the carbon chain and amine head, respectively, of the APS molecule. The SEM images of the same films after exposure to AuNPs is shown in Fig. 5.10. Only the functionalized film was able to immobilize AuNPs, and the AuNPs were evenly distributed along all the nanostructures. This confirms that not only was the vapor-phase functionalization process successful in chemically modifying the nanostructures, but also that the functionalized structures are highly accessible.

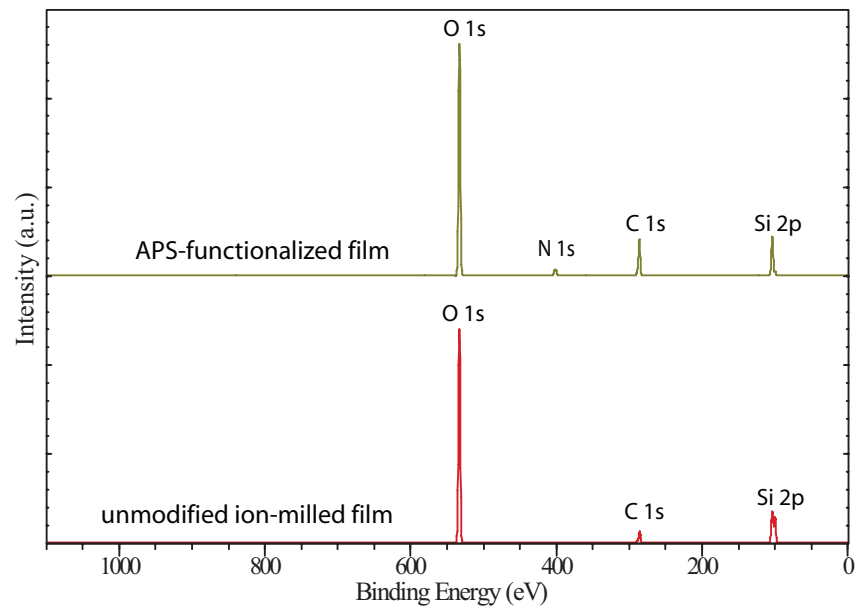


Figure 5.9: XPS survey spectrum of an unmodified and APS-functionalized ion-milled GLAD film

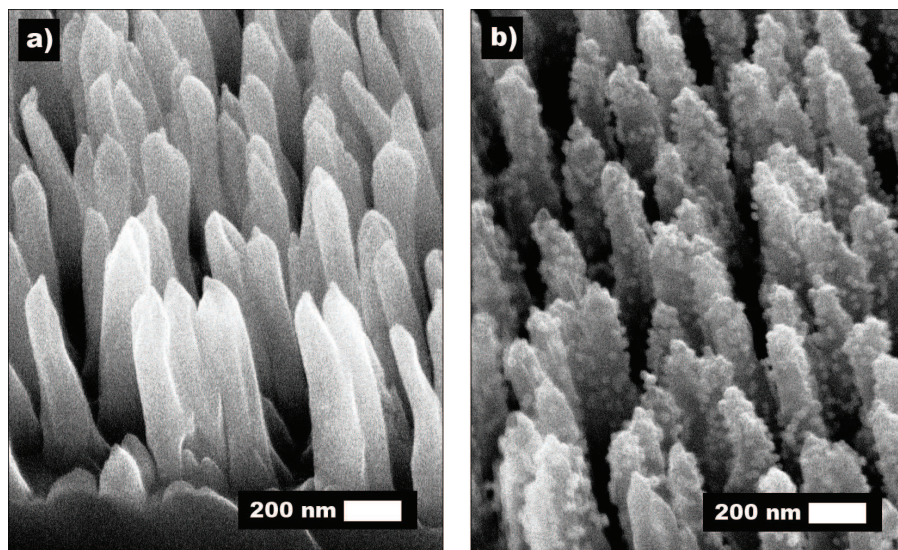


Figure 5.10: a) unmodified ion-milled film and b) APS-functionalized film after 24 h in a AuNP solution

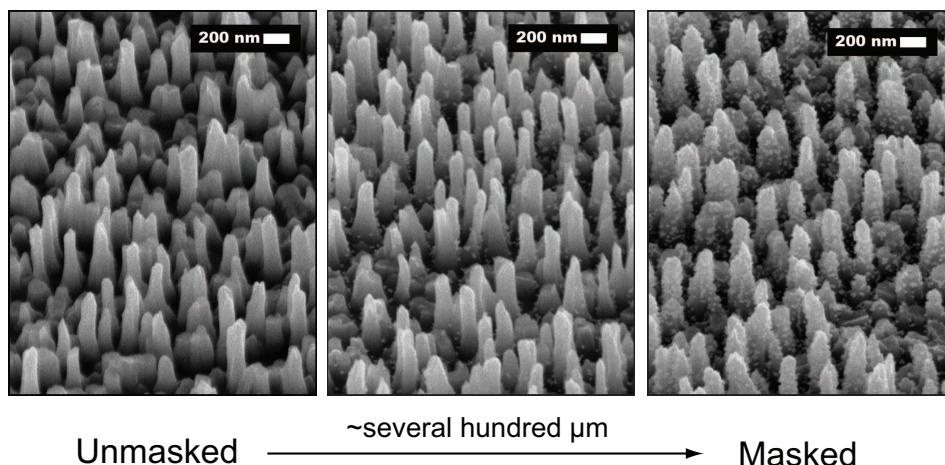


Figure 5.11: SEM images showing the transition from the unmasked region to the masked region of a functionalized GLAD film in a UV/ozone cleaner, followed by AuNP immobilization.

Finally, a brief experiment to try and pattern this chemical functionality into sections of the film was conducted. Half a functionalized sample was masked with aluminum foil and placed in a UV/ozone cleaner for 10 min to remove any APS from the exposed surface. After exposure the sample was reacted with the AuNPs again and then imaged (Fig. 5.11). It can be seen that the removal of the APS molecules was successful by the absence of AuNPs in the region that was exposed to the UV light. On the other hand, the masked region was able to maintain its chemical functionality and was able to immobilize the AuNPs as before. The transition width (where the edge of the mask was) was measured to be on the order of several hundred micrometres, which is quite small considering the imprecision of the masking method. It is probable that the transition width could be greatly reduced by using more a more precise masking process, such as using a finer edged mask.

5.6 Summary

This chapter has demonstrated the fabrication of GLAD nanostructures that are suitable for use in a liquid environment. Ion-milling of GLAD vertical post nanostructures was shown to be an effective and viable solution against the deleterious effects of post deformation and clustering upon exposure to liquid environments. The work here has shown that with sufficient ion-milling time, the nanostructures become more robust by thickening the diameter of the column bases and by reducing the capillary force on the nanostructures by smoothing of their surfaces. The salient characteristics of GLAD films—high aspect ratio and high surface area—are preserved in the ion-milling process.

Successful chemical functionalization of these nanostructures was also demonstrated in this chapter. Uniform immobilization of gold nanoparticles along the length of the nanostructures showed that the surface area provided by the nanostructures is highly accessible. Patterning of the surface chemistry was also shown to be possible, allowing for the potential of several high surface area regions with different chemical functionalities. Combined, these advantages make these modified GLAD nanostructures promising for integration with existing sensor technologies to enhancing their performance and functionalities.

Chapter 6

SAW liquid sensors enhanced with GLAD films¹

6.1 Introduction

Designing an acoustic-based sensor that is to operate in a liquid environment is challenging because elastic coupling of the wave with the liquid must be avoided. In the case of SAWs, liquid operation immediately removes the possibility of using Rayleigh waves, the most commonly used SAW, due to the significant radiation losses into the liquid (as mentioned in Sec. 2.2.6). As a result, shear-horizontal (SH) polarized waves have been almost exclusively employed for this application because they do not elastically couple with the liquid. In particular, Love wave devices have been extensively studied because of their high sensitivity [82, 84], as well as the inherent advantage of the waveguide layer protecting the electrodes from the environment.

Chapter 4 cited that various groups have employed nanostructures on SAW

¹A version of this chapter has been published in Sensors and Actuators B [156].

devices to increase effective surface area, and in turn, the sensitivity. However, almost all reports of nanostructure-enhanced SAW sensors have been on enhancing gas sensors, with limited studies on the enhancement of liquid sensors [81, 157, 158]. One reason for this is that high aspect ratio nanostructures tend to cluster or clump from the liquid capillary forces, which has caused them to be deemed unsuitable for sensors in a liquid environment [14, 19, 20]. As a solution to this, Chapter 5 demonstrated that ion-milling is an effective way of eliminating clustering for vertically-aligned nanostructures grown by GLAD. These modified structures are thus promising candidates for integration with sensors operating in a liquid environment. Conversely, clustered nanostructures have yet to be shown to be completely unusable for sensing applications. While they may lack the structure that is desired (vertically aligned), the clustered bundles of nanostructures may still be useful for certain applications that only require increased surface area.

In this chapter, the integration of nanostructured thin films fabricated by GLAD with Love wave SAW liquid sensors is investigated. Nanostructured thin films are first deposited on top of the SAW devices. One set of devices is then irreversibly clustered while another set is modified by ion-milling for comparison. The effect of film thickness with both of these film modifications on the device response is reported. Device performance is investigated by viscous loading of varying mixtures of glycerol and water, and compared to bare Love wave devices.

6.2 Experimental

6.2.1 Film preparation

SiO₂ vertical post nanostructured thin films were fabricated as per the procedure described in Sec. 3.3.2. A 30 nm layer of solid film was first grown (on the active area and IDTs) at an angle of 30°, followed by films deposited at an angle of 86° relative to the substrate normal with a pitch of 5 nm. An angle of 86° was used to produce highly porous films with well-separated structures. Films were deposited at a deposition rate of 1 nm/s as measured by the CTM. Half the devices were then ion-milled while the other half were clustered. An example of an as-deposited film can be seen in Fig. 6.1a.

Ion-milling was carried out following the same procedure used in Sec. 5.4.1. Milling times varied from 25 s to 40 s (increasing time with thickness), and were chosen with consideration of the minimum milling time required to prevent clustering. Fig. 6.1b shows an example of an ion-milled film used here. Though the films used here are considerably thinner than the films studied in the previous chapter, the effects of smoothed sides, sharper tips and wider bases are still present.

Clustering of the nanostructured films was achieved by placing a small droplet of DI water on top of the film, and then allowing it to dry off at room temperature. The devices were then rinsed with isopropyl alcohol to wash off residue that may have been present on the film. The effects of clustering can be seen in Figs. 6.1c and d. The slightly wider structures is attributed to a thicker chrome coating used to prevent charging during image acquisition. Fewer posts are also seen due to clustering in random directions, which is more apparent in the top-down view (Fig. 6.1d).

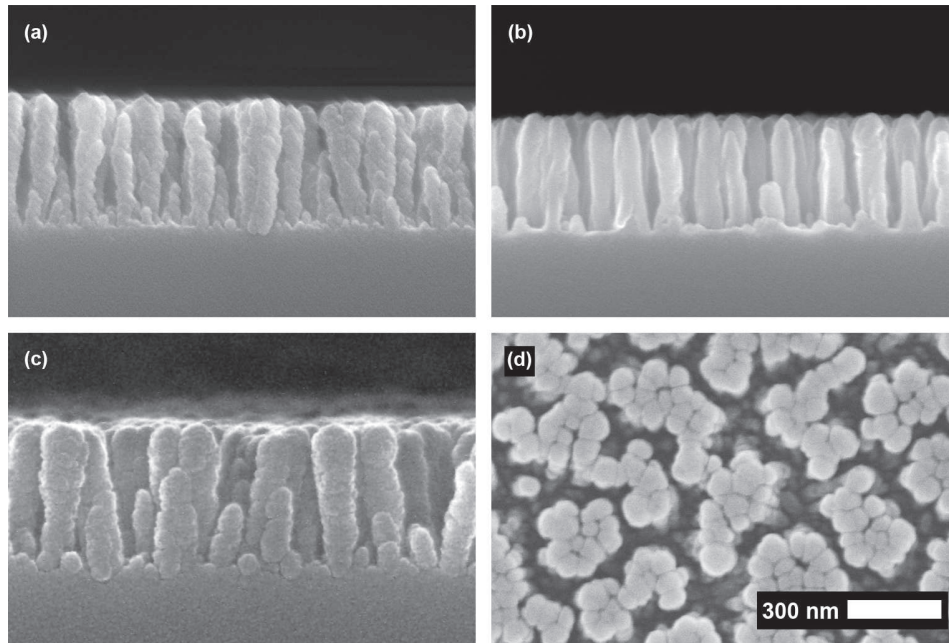


Figure 6.1: SEM images of (a) an as deposited GLAD film, followed by (b) ion-milling, or (c) clustering. (d) is a top-down SEM image of (c). Scale bar is applicable to all images. Reproduced from [156] with permission from Elsevier.

6.2.2 Measurement setup

Characteristics of the SAW devices before and after film deposition, and after film modification (ion-milling or clustering) were measured using the network analyzer and procedure outlined in Sec. 4.2.2. Measurements were made immediately after each process step.

The Love wave devices were placed in the oscillating circuit (Sec. 3.4.2) for liquid sensing experiments. Sensitivity to viscous loading was investigated by flowing varying mixtures of DI water/glycerol (Fisher Scientific) over the active area of the devices with a custom flow cell with a Viton o-ring seal, which was used for simplicity. The film on top of the IDTs and on the contact area between the o-ring and the device was carefully removed using a cotton-tipped applicator. The flow cell was attached to the sample holder via screws,

and the screws were tightened to the point where the IL of the device increased by ≈ 4.7 dB, as monitored on the network analyzer. This increase in IL is attributed to the relatively large area covered by the o-ring. This magnitude of increase was initially chosen because it was close to the minimum amount of pressure required to provide a complete seal on the device. Experiments were also reproducible with this value, so it was continually used for subsequent tests. A NE-4000 double syringe pump (New Era Pump Systems, Inc.) was used to withdraw mixtures over the active area at a rate of 0.5 mL/min. The fluid under test was held in place for 10 min during each measurement, which allowed signals to settle. Temperature was kept at 25 °C using an Octagon 20 Advance incubator (Brinsea).

6.3 Results and discussion

There have been few studies involving the use of ordered nanostructures on SAW devices, which has resulted in limited understanding of the interactions between them and the propagating acoustic wave. Thus, the effect of the addition of the nanostructures on the native response of the Love wave devices was studied first. Figs. 6.2 and 6.3 show the changes in IL and frequency shifts, respectively, for devices with varying film thicknesses, relative to the native Love wave devices. The change in IL initially increases in magnitude, in agreement with the study by Huang *et al.* [159], but then decreases for film thickness above 350 nm. Regardless of film thickness, the increasing IL indicates that the film is acting as a viscoelastic layer, since a purely mass-loading layer should not affect the IL [46, 120]. This may be the result of the nanostructures not being rigidly attached to the surface, and are therefore damping

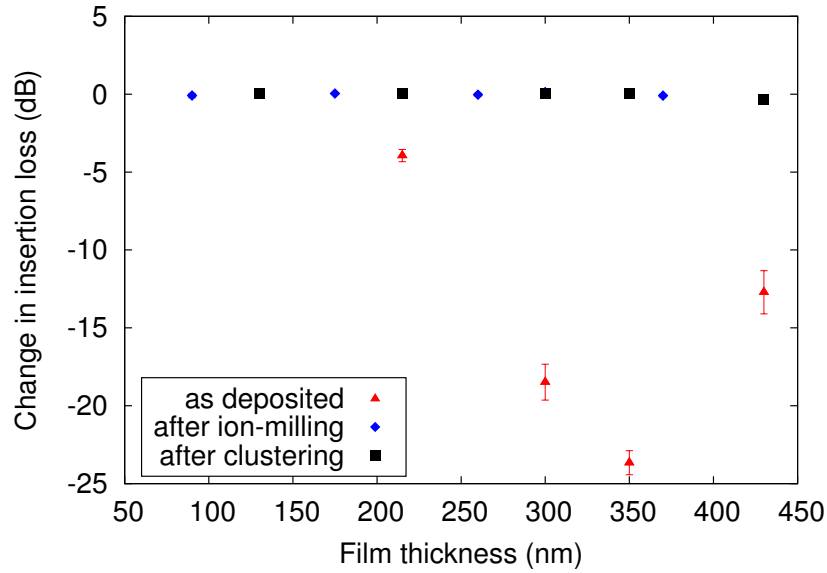


Figure 6.2: Relationship between GLAD film thickness and insertion loss, as-deposited, after ion-milling, and after clustering. Error bars are the standard deviations of the changes over several devices. Reproduced from [156] with permission from Elsevier.

the response by oscillating out of phase with and/or at a different frequency than the propagating wave. The magnitude of the frequency shifts follow a similar trend, increasing with film thickness initially, but then decreasing for film thickness above 300 nm. The trends in these results also differ from what was observed in Chapter 4, which used GLAD films deposited at a much lower angle of 70° compared to 86° here. For those films, the IL and frequency shift continually increased with film thickness.

The effect of ion-milling and clustering of the GLAD films on the Love wave devices were then investigated. The changes in IL and frequency shifts relative to the native Love wave devices after ion-milling and clustering are also shown in Figs. 6.2 and 6.3 respectively. For the ion-milled films, all of the points in both graphs are shifted to the left because ion-milling also reduces film thickness. Responses of the devices were also unchanged after DI water

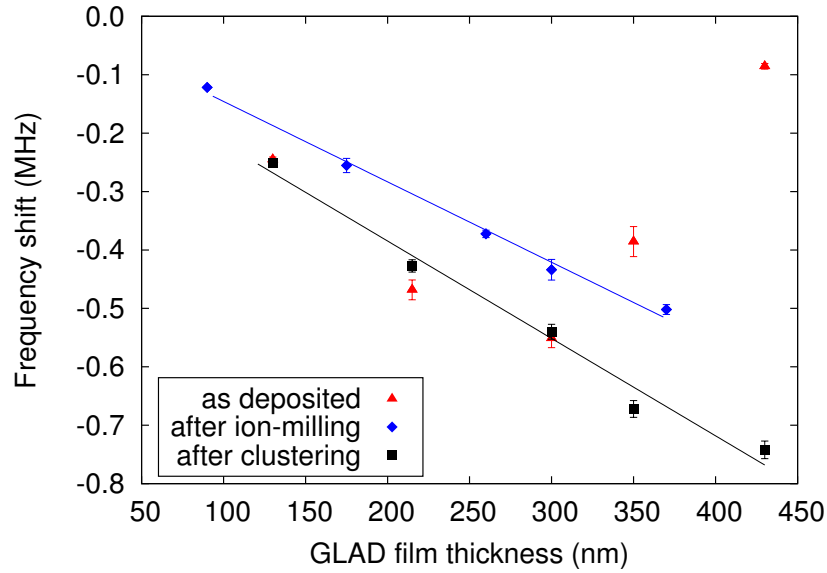


Figure 6.3: Relationship between GLAD film thickness and frequency shift, as deposited, after ion-milling, and after clustering. Error bars are the standard deviations of the shifts over several devices. Linear fits are shown for the ion-milled and clustered films. Reproduced from [156] with permission from Elsevier.

was dropped on the surface and allowed to dry, indicating that clustering is not an issue for the ion-milled structures and that further changes do not occur for the already clustered films. Contrary to what was seen with the as-deposited films, the change in IL for both sets of modified films is flat at 0 dB, showing that they are behaving like ideal mass-loading layers (rigidly attached) on top of the waveguide, with no dependence on film thickness. This is also supported by the linear relationship between frequency shifts and film thickness (increasing mass). The ion-milled films have a smaller frequency shift and corresponding slope compared to the clustered films, which can be attributed to the removal of material and thinning of the waveguide layer caused by the ion-milling process.

To test the feasibility of these nanostructures for use in sensing applications,

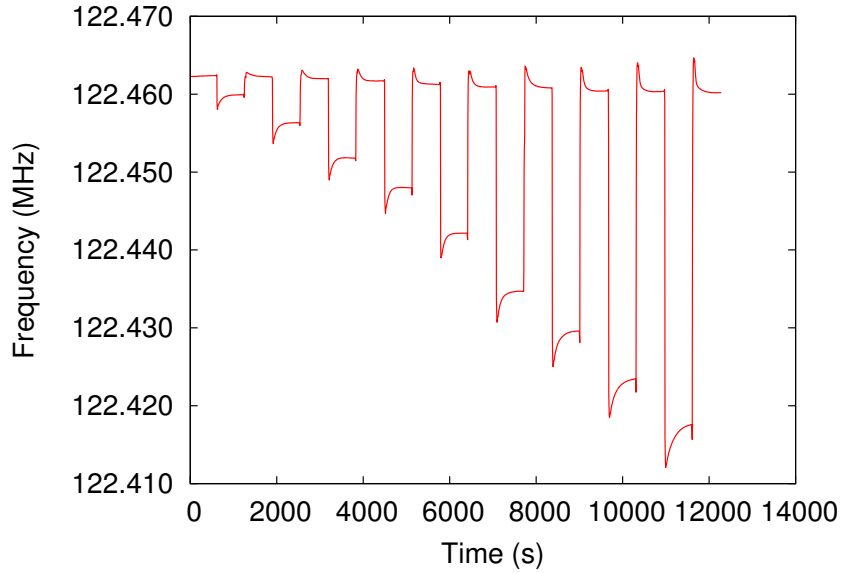


Figure 6.4: Frequency response of a Love-wave device with an ion-milled film to varying glycerol-water mixtures exchanged over the surface: 5.0, 10.0, 15.4, 20.0, 25.6, 32.9, 37.3, 42.3, 46.7 %.

the responses of the devices to viscous loading were investigated. Newtonian (low viscosity) liquid samples were used for this loading because of the known linear relation between frequency shift and $(\rho\eta)^{1/2}$, where ρ and η are, respectively, the density and viscosity of the liquid [51]. Different mixtures of glycerol and DI water were produced, and the viscosity and density of the resulting mixtures were extrapolated from published data [160]. Fig. 6.4 shows the time-resolved frequency response of a device with an ion-milled film. The sort of response observed, namely the decay to a shifted value and back to baseline, was observed for all tested devices. Exponential functions were fit to the decays to extract baseline and shifted frequency values. In the early stages of testing, some devices would continually decrease in frequency and never settle after a mixture of glycerol/water was exchanged into the flowcell. This was found to be linked with GLAD film that was not removed from the area where

the o-ring of the flow cell makes contact with the device. By carefully cleaning the area again with the cotton-tipped applicator, this problem was rectified. While not a serious issue in the present work, this presents a complication that must be addressed when designing future devices with GLAD. In particular, patterning or a more precise method of removing the film must be considered. At the same time, less contact of the flowcell walls with the SAW device would reduce signal loss, which may be achieved by making custom gaskets with thinner walls rather than using an o-ring.

A small problem that was encountered in this setup was that after returning to the baseline after each loading of glycerol/water, the baseline value was shifted down slightly. This was observed in all the tests, suggesting that this is a characteristic of the physical setup or the procedure and not of the individual devices. To test if this downward shift was correlated with the procedure, which always had increasing viscosity with successive loadings, two sets of trials with varying loading procedures were run:

1. increasing viscosity, then decreasing viscosity,
2. decreasing viscosity, then increasing viscosity.

The time-resolved frequency response of case 1 is shown in Fig. 6.5, and the baseline frequency following each loading is shown in Fig. 6.6. While the overall response does not appear to be adversely affected, Fig. 6.6 shows that there is a clear downward trend in the baseline frequency, particularly with the first half of the loadings. In addition to the decrease in the baseline values, the frequency shifts of the second half of the loadings are also shifted downwards slightly relative to the first half. Similarly, the same data for case 2 is shown in Figs. 6.7 and 6.8. It can be seen that once again the overall response is

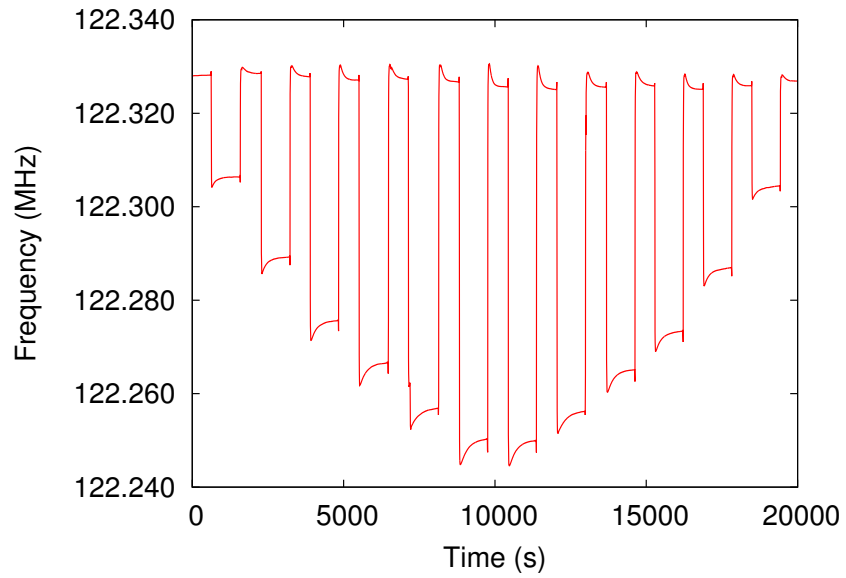


Figure 6.5: Frequency response of a Love wave device to increasing viscosity of glycerol/water mixtures exchanged over the surface, then reversing the order: 15.4, 25.6, 32.9, 37.3, 42.3, 46.7%.

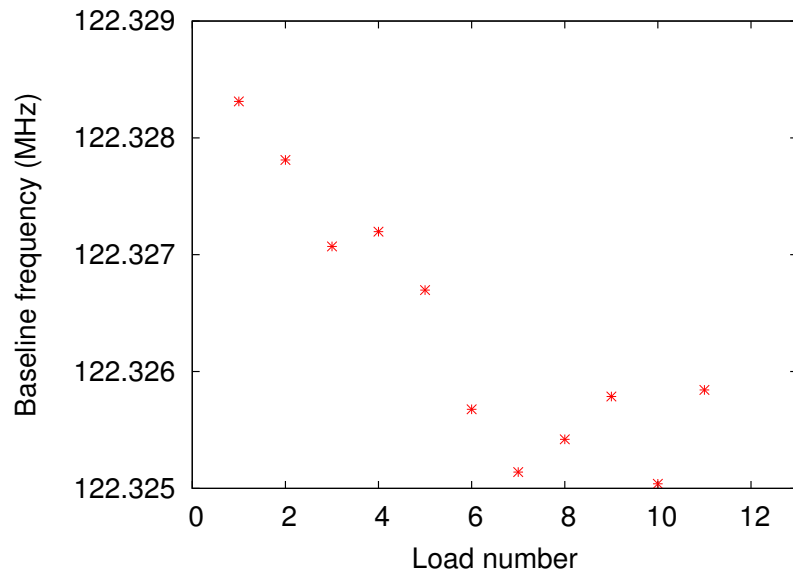


Figure 6.6: Baseline frequency values for successive viscous loadings in Fig. 6.5.

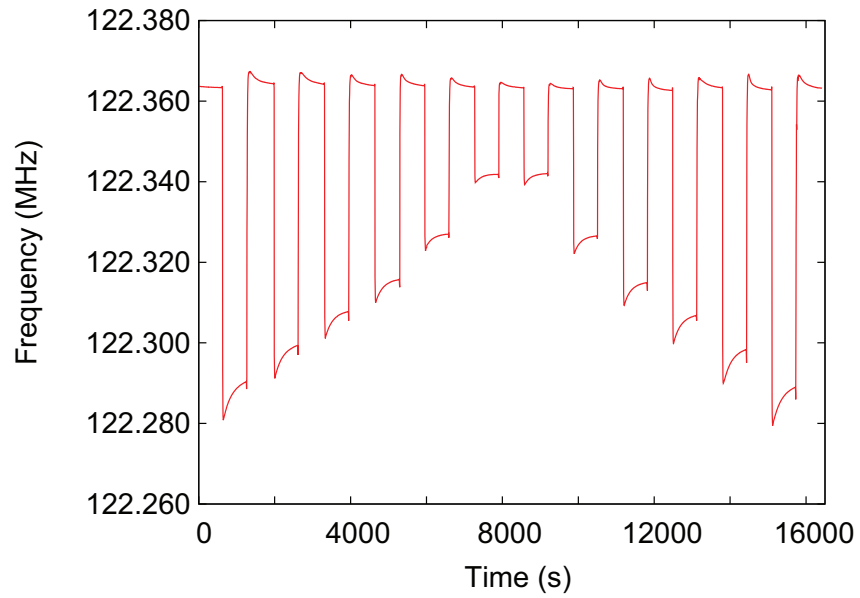


Figure 6.7: Frequency response of a Love wave device to decreasing viscosity of glycerol/water mixtures exchanged over the surface, then reversing the order: 46.7, 42.3, 37.3, 32.9, 25.6, 15.4 %.

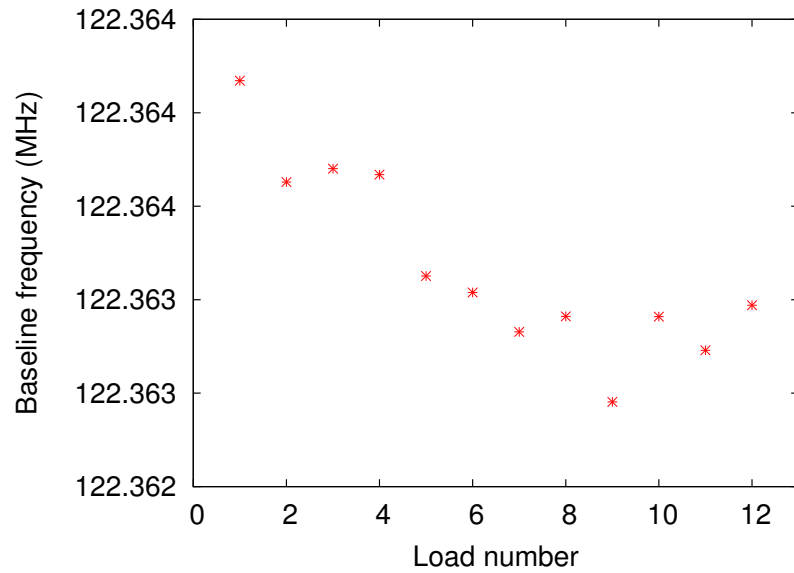


Figure 6.8: Baseline frequency values for successive viscous loadings in Fig. 6.7.

not significantly affected, and the trend with the baseline values is very similar to that seen in Fig. 6.6 for case 1. Thus, the order of viscosity loading was shown not to be the cause of the shift in baseline frequency values and the effect is most likely characteristic of the physical setup. A potential cause for this downward shift is from the use of a removable o-ring with the flowcell. It is possible that glycerol is being irreversibly trapped around the seal area after each loading due to the round shape of the o-ring, which creates very small pockets around the seal. However, due to the relatively small magnitude of the shift, and its reproducibility, this was not investigated further.

From the above results, it appeared that the frequency shifts for each loading shifted down the same amount as the baseline frequency value. To confirm that this was the case, a device with GLAD was loaded with the same glycerol/water mixture several times. The result of this experiment is shown in Fig. 6.9, clearly showing that the shifted operating frequency due to viscous loading follows the same downward trend with the baseline value. The frequency shifts for this trial were obtained by taking the difference between the shifted operating frequency (due to the loading), and the baseline operating frequency immediately prior to that loading. The average shift over the four loadings was 4577 Hz with a standard deviation of 205 Hz, which equates to a small percentage of the average shift. This confirmed the original assumption, and demonstrated that even though the operation frequency slightly changes with each successive loading, the frequency shift, and thus sensitivity, remains constant. As a result, this method of obtaining the frequency shift for a given viscous loading was applied to all trials.

Fig. 6.10 shows the frequency shifts with respect to $(\rho\eta)^{1/2}$ for a bare Love wave device and those employing ion-milled and clustered GLAD films. It can

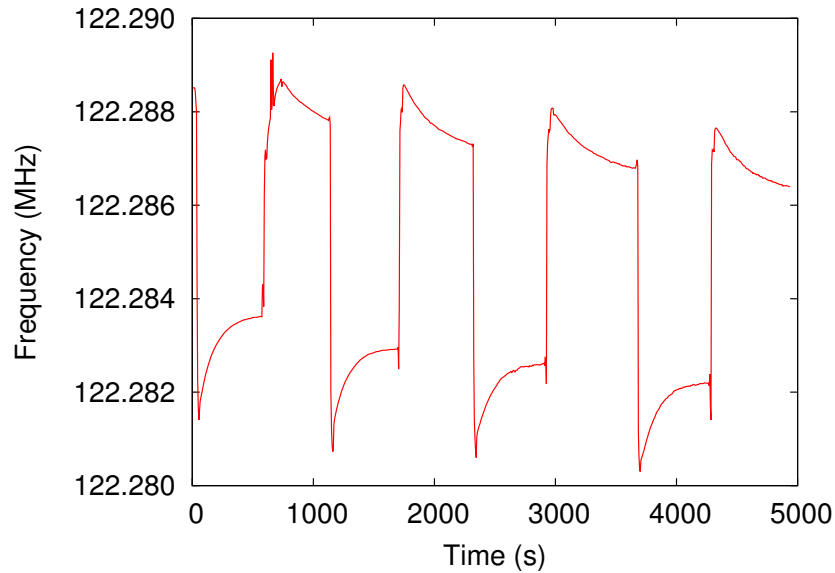


Figure 6.9: Frequency reponse of a Love wave device to the several loadings of the same glycerol/water mixture.

be seen that the magnitude of the shifts for a given mixture increases with film thickness, showing increased interaction between the nanostructures and the liquid. However, with a film thickness of 430 nm that was clustered, and the corresponding film with a thickness of 370 nm after ion-milling, the oscillation signals were lost when only water was flowed in. Looking at the signals for these devices with the network analyzer revealed that they were completely damped. While there are no apparent losses in air, there are considerable losses in a liquid environment, particularly with thicker films. The thicker films (taller posts) have larger radiative losses to the surrounding liquid environment. This puts an upper limit on the thickness of ion-milled GLAD that can be practically used with SAW liquid sensors. Furthermore, the viscosity and density of the liquid environment puts further constraints on the thickness of the film that can be used, since viscous loading also affects the amplitude of the signal in addition to the operating frequency [48]. This was particularly

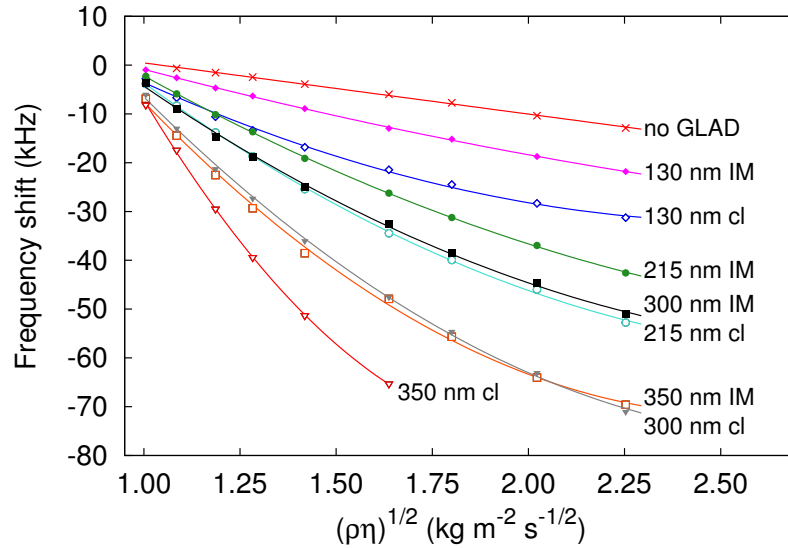


Figure 6.10: Frequency shifts with respect to the square root of density-viscosity product for varying thicknesses of GLAD thin films, with fits for each data set. Reproduced from [156] with permission from Elsevier.

apparent with the device that had a 350 nm thick film that was clustered, where the oscillation signal was lost during testing after flowing in a mixture with $(\rho\eta)^{1/2} = 1.80 \text{ kg m}^{-2} \text{ s}^{-1/2}$. The corresponding film with an ion-milled thickness of 300 nm did not have its signal damp out for any of the tested glycerol/water mixtures.

The bare Love wave device showed a linear relationship as expected, but all devices with modified GLAD films exhibited a non-linearity that becomes more pronounced with increasing film thickness. This is not surprising, as the nanostructured films, ion-milled or clustered, have an increased interaction with the liquid medium, as demonstrated above and in agreement with the findings of Water and Chen [81]. The shifts in Fig. 6.10 were thus fit with exponentials, which fit the data more accurately. Because the frequency shifts were taken with respect to water, the fitted lines of Fig. 6.10 will not intersect

0 Hz at $(\rho\eta)^{1/2} = 0 \text{ kg m}^{-2} \text{ s}^{-1/2}$, and instead should intersect 0 Hz at a value of $(\rho\eta)^{1/2} = 0.94 \text{ kg m}^{-2} \text{ s}^{-1/2}$ (value for water at 25 °C). In all cases, at $(\rho\eta)^{1/2} \approx 0.94$, $\Delta f \approx 0$,

The sensitivity, which is taken as the slope of the curves, is non-linear rather than a constant, as with the bare Love wave device. The sensitivity curves are shown in Fig. 6.11, which also shows that the highest increases in sensitivity occur at low values of $(\rho\eta)^{1/2}$. While sensitivity curves based on an exponential fit imply that the sensitivity will drop to zero for high values of $(\rho\eta)^{1/2}$, we hypothesize that the signal will be damped out before that point is reached. Furthermore, the behavior for native Love wave devices at high viscosities (Maxwellian region) is much different than in the Newtonian region, so it is probable that this is also the case with devices with nanostructured films on them.

The sensitivity of devices with clustered films is shown to be consistently higher than their ion-milled counterparts. This is likely due to the clustered films having significantly higher surface area than the ion-milled films as a result of the taller structures and the rougher surface of the nanostructures, despite having reduced surface area due to clustering of the individual structures. These results disaffirm the suggestion by Rao and Zhang that nanostructures grown by GLAD are not suitable for use in liquid sensors because of the clustering effect [14]. Because the initial clustering of the nanostructures is irreversible and the clusters become rigid with the device surface, then accuracy and reproducibility are no longer issues. As the results here demonstrate, these clustered films still exhibit a high surface area that is mostly accessible for viscosity sensing. However, certain applications may require an ordered structure (such as that provided by ion-milled films) for fluid flow reasons, or

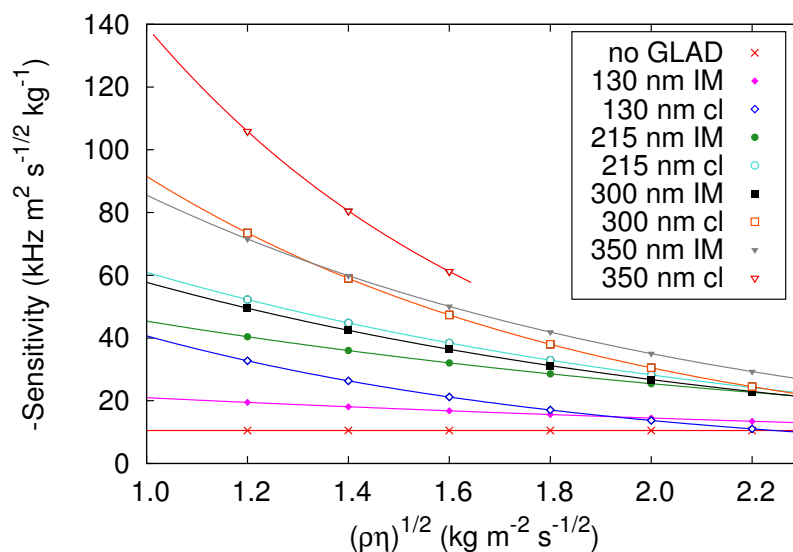


Figure 6.11: Sensitivity curves with respect to $(\rho\eta)^{1/2}$ for devices with varying GLAD film thicknesses. The curve for the 350 nm clustered film is truncated past $(\rho\eta)^{1/2} = 1.6$ because there was no data collected for these values of $(\rho\eta)^{1/2}$. Points for each curve are included for clarity. Reproduced from [156] with permission from Elsevier.

the application may not fully take advantage of the nanoscale roughness of as-deposited GLAD films, such as immobilization of larger molecules, so that the useful surface area provided by ion-milled films is actually higher than clustered films.

With either case, clustered or ion-milled, even though the sensitivity does decrease with increasing values of $(\rho\eta)^{1/2}$, the sensitivity is in general still significantly higher than a bare device, as expected due to the increased surface area. The sensitivity increase from an ion-milled 300 nm thick film at $(\rho\eta)^{1/2} = 1.2 \text{ kg m}^{-2} \text{ s}^{-1/2}$ relative to a bare device was approximately 4.7x, a result comparable to that seen by Water *et al.* based on only shifts due to water [81]. In their study, they concluded that the sensitivity was dependent on the ratio of nanorod length to device wavelength. Their maximum sensitivity was achieved

at a ratio of 0.014, with 280 nm tall nanorods on a device with $\lambda = 20 \mu\text{m}$. The results of our study here gave a comparable sensitivity gain (based on the ion-milled 300 nm thick film) at a ratio of 0.0075 ($h = 300 \text{ nm}$, $\lambda = 40 \mu\text{m}$) and the signal was completely lost by a ratio of 0.0093. This suggests that the sensitivity is not entirely dependent on this ratio, but possibly a combination of other factors, more notably the absolute thickness of the film (or height of the nanostructures), the density of the nanostructures, and the material of the nanostructures. The taller nanostructures, for example, have increased interaction with the liquid since each nanostructure has to oscillate through more liquid. This interaction may have considerably more impact on the losses and/or sensitivity than shorter nanostructures in larger numbers. Such factors motivate future studies in this area.

6.4 Summary

This study has demonstrated the feasibility of using nanostructured vertical posts fabricated by GLAD with Love wave SAW devices for liquid sensing. High-alpha deposited GLAD films were grown on the SAW devices and studied. As-deposited nanostructures were shown to have a significant impact on the response of the device, particularly the increase in signal loss. This signal loss disappeared after the nanostructures were ion-milled or clustered, which were used to enable the films for use in a liquid environment. The resulting devices had shifted operation frequencies, and the lack of signal loss implied the presence of rigidly coupled films on the devices. Devices with varying thicknesses of ion-milled and clustered GLAD films were shown to increase sensitivity through viscous loading. Viscous loading sensitivity increased with

film thickness, but non-linear behavior was exhibited by both ion-milled and clustered films. Devices were rendered unusable by an ion-milled thickness of 370 nm or a clustered film thickness of 430 nm due to significant signal loss through the film to the liquid environment. Clustered films were also shown to provide a higher sensitivity than their ion-milled counter-parts. The ability of clustered and ion-milled GLAD films to enhance SAW viscosity sensors encourages further studies to extend this enhancement to more critical applications, such as biosensors for public health purposes.

Chapter 7

Conclusion

7.1 Concluding remarks

Sensors continue to play a dominant role in today's society by helping increase our standard of living. Consequently, there is a continual effort to develop faster, cheaper, more accurate, and more reliable sensors. This has resulted in the development of new technologies or even the extension of existing ones, to achieve these goals. The application of SAW technology to sensors is an example of the latter case, and the past two decades have seen a significant increase in the study of SAW devices for sensing applications. Concurrently, the advent of nanotechnology has enabled the miniaturization and improvement of many technologies, and continues to be promising for new technologies in a wide range of fields. In particular, the fabrication and utilization of nanomaterials for sensors have become hot topics because of the unique characteristics exhibited by these materials, such as extremely high surface area. GLAD is an advanced PVD technique that can fabricate nanostructured thin films with high porosity and surface area. It is a very flexible technique that can utilize

many different materials and produce a wide variety of morphologies. These characteristics make the GLAD process extremely attractive for integration with existing sensor technologies to further enhance their performance. The work presented here thus investigated the use of nanostructured thin films fabricated by GLAD to enhance the performance of SAW sensors.

Dense, high surface area GLAD thin films were integrated with SAW devices for the first time, as reported in Chapter 4. The films were shown to have an impact on signal loss, which increased with film thickness. However, the increase in sensitivity to humidity was greatly improved, even with a very thin GLAD film. The initial long term stability of the sensors was also shown to be quite good. Comparing this work to performance values reported in the literature showed that these GLAD films are much better at enhancing the performance of the SAW sensors. This encourages further work to better understand the effect of GLAD films on the native SAW response and optimize the sensitivity that can be achieved with GLAD.

The clustering of the nanostructures grown by GLAD has been studied in the literature, and has been one of the main reasons why GLAD has not been extensively studied for applications in liquid environments. In order to use GLAD thin films with SAW sensors that operate in liquids, it was deemed necessary to develop a method of retaining the structure and accessibility provided by as-deposited GLAD thin films. Chapter 5 focused on this challenge, and it was shown that post-deposition ion-milling was an effective method of creating more rigid vertical post structures that would not cluster together after being exposed to liquids. Ion-milling had the effect of smoothing the sides of the structures, as well as widening the base, both effects contributing to the overall effect of eliminating clustering. The accessibility of the surface

area was also retained, which was demonstrated by chemical functionalization of the surface of the film followed by immobilization of gold nanoparticles for visual confirmation.

Subsequently, these ion-mill-modified structures were integrated with SAW sensors and investigated for their effects on the native response and sensing performance in Chapter 6. Clustered structures were also studied because there have been no reports that actually show that these structures are unsuitable for use. Unlike in Chapter 4, well separated nanostructures were fabricated by using a high deposition angle, and these were shown to increase signal loss. Ion-milling and clustering were shown to remove any signal loss originally introduced with the addition of the GLAD film, demonstrating that both modifications cause the film to become rigidly attached to the surface. Enhanced sensitivity to viscosity, albeit non-linear, was achieved by both types of modified films, with clustered films having larger enhancements than their ion-milled counterparts. This was attributed to the reduced height and smoothed surface of the ion-milled structures, which reduced the usable surface area for viscosity sensing.

In summary, the conclusions of this work are listed below.

- Dense, vertical post, SiO₂ films were fabricated by GLAD onto Love wave SAW devices for the first time.
- Increasing film thickness of these dense films caused a decrease in operating frequency and increase in the IL
- Sensitivity to humidity of SAW devices with GLAD films exponentially increased with thickness, despite relatively linear increase in surface area.

- GLAD-enhanced SAW humidity sensors showed promising long term stability and increased response times.
- Ion-milling was shown to be an effective method to eliminate the clustering effect experienced in liquids, by widening the base of the structures and reducing the capillary forces acting on the nanostructures by smoothing the surface.
- Thicker films require longer milling times to eliminate clustering.
- Chemical functionalization of ion-milled films was successfully demonstrated, and verified by uniformly dispersed immobilization of gold nanoparticles on the structures.
- Patterning of the surface chemistry of the ion-milled films using a masked sample in a UV/ozone cleaner was shown.
- Ion-milled or intentionally clustered high-deposition-angle GLAD films on Love wave SAW devices behaved like rigid mass-loading layers (shifted operating frequency with no signal loss).
- Ion-milled and clustered films exhibited non-linear frequency shifts from viscous loading of glycerol/water mixtures, contrary to the linear behavior of bare Love wave devices.
- Devices became unusable in liquid by an ion-milled thickness of 360 nm or a clustered film thickness of 430 nm due to significant signal loss through the film to the liquid environment.
- Sensitivity to viscous loading was increased by ion-milled and clustered films, with clustered films having larger enhancements compared to their

ion-milled counterparts.

7.2 Future work

Following the new results presented in this thesis, there are many opportunities available for future research. An improved theoretical understanding of the interaction of GLAD and the SAW would be a major benefit. To date, studies involving nanomaterials and SAW sensors have been solely experimental, with little understanding of how those nanomaterials actually interact with the SAW. For example, both dense and well-separated structures grown by GLAD were studied in this thesis, and both had somewhat different effects on the response of the device. An increase in modeling studies would also benefit alongside the improved theory, as this would allow for a more accurate prediction of device response to allow for better design of films and devices prior to fabrication.

As already alluded to in Chapter 4, an extension of the results there would be to chemically functionalize the GLAD films to enable specificity for other gases. While the chemistry used in Chapter 5 was on ion-milled films, there have been studies showing successful functionalization of as-deposited GLAD films [116, 161]. By carefully choosing the right precursor, the films can be tailored to respond more strongly to certain gases. Since the footprint of the SAW devices is also quite small, an array of devices with different surface chemistries can be made to create a differential sensor [162, 163], similar to the human nose. This sort of sensor would be very advantageous since it would not be limited to sensing a single type of gas.

The viscosity sensor developed in Chapter 6 was the first step to demon-

strating the viability of GLAD films for use in a liquid application. Development of biosensors using GLAD would be the next logical step towards the ultimate goal of enhancing public health. This would include testing the sensitivity to mass-loading in a liquid environment. Like above, functionalization of the films is a necessary step to provide the proper surface chemistry. Protein adsorptions onto modified SAW devices have been commonly used as standard test for biosensitivity [50, 164, 165], and would provide a good starting point for comparison. It would also provide further insight on the non-linear response observed in this work.

The demonstration of enhanced SAW sensors by utilizing GLAD thin films also opens many paths for optimization. For example the effect of deposition angle on sensitivity enhancement for a particular application (such as gas sensing), was not looked at. Similarly, performance of the sensors was also only compared by increasing film thickness over a fixed planar surface area. It would be interesting to study the response and performance of SAW sensors by varying the overall surface area by changing both the nanostructure height and lateral coverage of the nanostructures, rather than just the nanostructure height. It is possible that the performance enhancement is greater for thinner films over a larger area than the converse. This may also be cocurrently linked with optimizing the SAW device features (*e.g.*, waveguide thickness, delay-line length, *etc.*). Future work in these areas would benefit the field, pushing further towards commercialization.

7.3 Final remarks

SAW sensors, though extremely promising, are still in their early stages of development, with much yet to be learned and studied before becoming an established sensor technology. By fabricating nanostructured thin films using GLAD that are able to function with SAW sensors, and demonstrating that they increase sensitivity in liquid and gas environments, this thesis has opened the doors for the development of a new generation of SAW sensors with increased capabilities. The sensitivity enhancement of SAW sensors provided by GLAD is not only encouraging for future development of GLAD-enhanced SAW sensors, but also for the potential integration of GLAD with other sensing platforms. In particular, the films engineered in this thesis allow for the application to other technologies that function in liquid environments, which had previously been avoided.

Bibliography

- [1] D. Patranabis. *Sensors and Transducers*. 2nd. Prentice-Hall of India, 2004.
- [2] P. R. Wiederhold. *Water Vapor Measurement: Methods and Instrumentation*. Taylor & Francis, 1997.
- [3] C. M. van 't Land. *Drying in the Process Industry*. Wiley, 2011.
- [4] G. Gautschi. *Piezoelectric Sensorics: Force, Strain, Pressure, Acceleration and Acoustic Emission Sensors, Materials and Amplifiers*. Engineering Online Library. Springer, 2006.
- [5] B. McCollum and O. S. Peters. *A new electrical telemeter*. Technologic papers of the Bureau of Standards. Govt. Print. Off., 1924.
- [6] Bosch. <http://www.bosch-sensortec.com/content/language1/html/4377.htm>.
- [7] M. Bally, M. Halter, J. Vörös, and H. Grandin. “SPR for molecular interaction analysis: a review”. *Surface and interface analysis* **38**(11), 2006, pp. 1442–1458.
- [8] S. Schlücker. “SERS microscopy: nanoparticle probes and biomedical applications.” *Chemphyschem : a European journal of chemical physics and physical chemistry* **10**(9-10), 2009, pp. 1344–54.

- [9] R. Karlsson. “SPR for molecular interaction analysis: a review of emerging application areas.” *Journal of molecular recognition : JMR* **17**(3), 2004, pp. 151–61.
- [10] K. Länge, B. E. Rapp, and M. Rapp. “Surface acoustic wave biosensors: a review.” *Analytical and bioanalytical chemistry* **391**(5), 2008, pp. 1509–19.
- [11] S. Sheikh, C. Blaszykowski, and M. Thompson. “Acoustic Wave-Based Detection in Bioanalytical Chemistry: Competition for Surface Plasmon Resonance?” *Analytical Letters* **41**(14), 2008, pp. 2525–2538.
- [12] B. Drafts. “Acoustic wave technology sensors”. *IEEE Transactions on Microwave Theory and Techniques* **49**(4), 2001, pp. 795–802.
- [13] H. Wohltjen and R. Dessy. “Surface acoustic wave probe for chemical analysis. I. Introduction and instrument description”. *Analytical Chemistry* **51**(9), 1979, pp. 1458–1464.
- [14] Y. L. Rao and G. Zhang. “Enhancing Sensitivity of SAW Devices with Nanostructures”. *Current Nanoscience* **2**, 2006, pp. 311–318.
- [15] M. T. Taschuk, M. M. Hawkeye, and M. Brett. “Glancing angle deposition”. *Handbook of Deposition Technologies for Films and Coatings*. 3rd. Elsevier, 2010.
- [16] K. Zhu, T. B. Vinzant, N. R. Neale, and A. J. Frank. “Removing Structural Disorder from Oriented TiO₂ Nanotube Arrays: Reducing the Dimensionality of Transport and Recombination in Dye-Sensitized Solar Cells”. *Nano Letters* **7**(12), 2007, pp. 3739–3746.

- [17] K. K. S. Lau, J. Bico, K. B. K. Teo, M. Chhowalla, G. A. J. Amaratunga, W. I. Milne, G. H. McKinley, and K. K. Gleason. “Superhydrophobic Carbon Nanotube Forests”. *Nano Letters* **3**(12), 2003, pp. 1701–1705.
- [18] C. Journet, S. Moulinet, C. Ybert, S. T. Purcell, and L. Bocquet. “Contact angle measurements on superhydrophobic carbon nanotube forests: Effect of fluid pressure”. *Europhysics Letters (EPL)* **71**(1), 2005, pp. 104–109.
- [19] V. Anandan, Y. L. Rao, and G. Zhang. “Nanopillar array structures for enhancing biosensing performance.” *International Journal of Nanomedicine* **1**(1), 2006, pp. 73–9.
- [20] J.-G. Fan, D. Dyer, G. Zhang, and Y.-P. Zhao. “Nanocarpets Effect: Pattern Formation during the Wetting of Vertically Aligned Nanorod Arrays”. *Nano Letters* **4**(11), 2004, pp. 2133–2138.
- [21] J.-G. Fan, J.-X. Fu, A. Collins, and Y.-P. Zhao. “The effect of the shape of nanorod arrays on the nanocarpets effect”. *Nanotechnology* **19**(4), 2008, p. 045713.
- [22] E. Dieulesaint and D. Royer. *Elastic waves in solids: applications to signal processing*. J. Wiley, 1980, p. 511.
- [23] B. A. Auld. *Acoustic fields and waves in solids*. Acoustic Fields and Waves in Solids v. 1. Wiley, 1973.
- [24] W. G. Cady. *Piezoelectricity, Vol. 1*. New York: Dover Publications Inc., 1964, p. 405.
- [25] J. W. Gardner, V. K. Varadan, and O. O. Awadelkarim. *Microsensors, MEMS, and Smart Devices*.

- [26] C. Campbell. *Surface acoustic wave devices and their signal processing applications*. Academic Press, 1989.
- [27] L. Rayleigh. “On Waves Propagated along the Plane Surface of an Elastic Solid”. *Proceedings of the London Mathematical Society* **s1-17**(1), 1885, pp. 4–11.
- [28] J. L. Bleustein. “A New Surface Wave in Piezoelectric Materials”. *Applied Physics Letters* **13**(12), 1968, p. 412.
- [29] Y. V. Gulyaev. “Electroacoustic surface waves in solids”. *JETP Letters* **9**(1), 1969, pp. 37–38.
- [30] M. Thompson and D. C. Stone. *Surface-launched acoustic wave sensors: chemical sensing and thin-film characterization*. Chemical analysis. Wiley, 1997.
- [31] A. E. H. Love. *Some Problems of Geodynamics: Being an Essay to which the Adams Prize in the University of Cambridge was Adjudged in 1911*. Dover books on geology, geography, meteorology. Dover Publications, 1967.
- [32] J. Du, G. L. Harding, A. F. Collings, and P. R. Dencher. “An experimental study of Love-wave acoustic sensors operating in liquids”. *Sensors and Actuators A: Physical* **60**(1-3), 1997, pp. 54–61.
- [33] J. Freudenberg, M. von Schickfus, and S. Hunklinger. “A SAW immunosensor for operation in liquid using a SiO₂ protective layer”. *Sensors and Actuators B: Chemical* **76**(1-3), 2001, pp. 147–151.
- [34] G. L. Harding and J. Du. “Design and properties of quartz-based Love wave acoustic sensors incorporating silicon dioxide and PMMA guiding layers”. *Smart Materials and Structures* **6**(6), 1997, pp. 716–720.

- [35] E. Gizeli. “Design considerations for the acoustic waveguide biosensor”. *Smart Materials and Structures* **6**, 1997, p. 700.
- [36] G. McHale, M. I. Newton, F. Martin, E. Gizeli, and K. a. Melzak. “Resonant conditions for Love wave guiding layer thickness”. *Applied Physics Letters* **79**(21), 2001, p. 3542.
- [37] M. I. Newton, G. McHale, and P. Roach. “ST Quartz Acoustic Wave Sensors with Sectional Guiding Layers”. *Sensors* **8**(7), 2008, pp. 4384–4391.
- [38] J. Grate and S. Martin. “Acoustic wave microsensors”. *Analytical Chemistry* **65**(21), 1993, 940A–948A.
- [39] S. Datta. *Surface acoustic wave devices*. Prentice-Hall, 1986.
- [40] H. Wohltjen and R. Dessy. “Surface acoustic wave probes for chemical analysis. II. Gas chromatography detector”. *Analytical Chemistry* **51**(9), 1979, pp. 1465–1470.
- [41] H. Wohltjen and R. Dessy. “Surface acoustic wave probes for chemical analysis. III. Thermomechanical polymer analyzer”. *Analytical Chemistry* **51**(9), 1979, pp. 1470–1475.
- [42] C. Caliendo, P. Verardi, E. Verona, A. D’Amico, C. D. Natale, G. Saggio, M. Serafini, R. Paolesse, and S. E. Huq. “Advances in SAW-based gas sensors”. *Smart Materials and Structures* **6**(6), 1997, pp. 689–699.
- [43] M. Penza, F. Antolini, and M. Antisari. “Carbon nanotubes as SAW chemical sensors materials”. *Sensors and Actuators B: Chemical* **100**(1-2), 2004, pp. 47–59.

- [44] C. Mah and K. B. Thurbide. “Acoustic methods of detection in gas chromatography”. *Journal of Separation Science* **29**(12), 2006, pp. 1922–1930.
- [45] G. S. Calabrese, H. Wohltjen, and M. K. Roy. “Surface acoustic wave devices as chemical sensors in liquids. Evidence disputing the importance of Rayleigh wave propagation”. *Analytical Chemistry* **59**(6), 1987, pp. 833–837.
- [46] G. Kovacs, M. Vellekoop, R. Haueis, G. Lubking, and a. Venema. “A love wave sensor for (bio)chemical sensing in liquids”. *Sensors and Actuators A: Physical* **43**(1-3), 1994, pp. 38–43.
- [47] G. Kovacs and A. Venema. “Theoretical comparison of sensitivities of acoustic shear-wave modes for (bio)chemical sensing in liquids”. *Appl. Phys. Lett* **61**, 1992, pp. 639–641.
- [48] F. Herrmann, M. Weihnacht, and S. Buttgenbach. “Properties of shear-horizontal surface acoustic waves in different layered quartz-SiO₂ structures”. *Ultrasonics* **37**(5), 1999, pp. 335–341.
- [49] G. Harding. “Mass sensitivity of Love-mode acoustic sensors incorporating silicon dioxide and silicon-oxy-fluoride guiding layers”. *Sensors and Actuators A: Physical* **88**(1), 2001, pp. 20–28.
- [50] P. Roach, S. Atherton, N. Doy, G. Mchale, and M. I. Newton. “SU-8 Guiding Layer for Love Wave Devices”. *Sensors (Peterborough, NH)* **7**(11), 2007, pp. 2539–2547.
- [51] K. Mitsakakis, a. Tsortos, J. Kondoh, and E. Gizeli. “Parametric study of SH-SAW device response to various types of surface perturbations”. *Sensors and Actuators B: Chemical* **138**(2), 2009, pp. 408–416.

- [52] K. Keiji Kanazawa and J. G. Gordon. “The oscillation frequency of a quartz resonator in contact with liquid”. *Analytica Chimica Acta* **175**, 1985, pp. 99–105.
- [53] F. Josse. “Effects of liquid relaxation time on SH surface waves liquid sensors”. *The Journal of the Acoustical Society of America* **85**(4), 1989, p. 1556.
- [54] S. I. Shah, G. H. Jaffari, E. Yassitepe, and B. Ali. “Evaporation: Processes, Bulk Microstructures, and Mechanical Properties”. *Handbook of Deposition Technologies for Films and Coatings: Science, Applications and Technology*. Ed. by P. M. Martin. 3rd. Elsevier, 2010.
- [55] M. Ohring. *Materials Science of Thin Films: Deposition and Structure*. 2nd. Oxford, UK: Academic Press, 2002.
- [56] J. A. Thornton. “High Rate Thick Film Growth”. *Annual Review of Materials Science* **7**(1), 1977, pp. 239–260.
- [57] E. Bauer. “Phänomenologische Theorie der Kristallabscheidung an Oberflächen. I”. *Zeitschrift für Kristallographie* **110**(1-6), 1958, pp. 372–394.
- [58] J. Venables, G. Spiller, and M. Hanbucken. “Nucleation and growth of thin films”. *Reports on Progress in Physics* **47**, 1984, p. 399.
- [59] A. Dirks and H. Leamy. “Columnar microstructure in vapor-deposited thin films”. *Thin Solid Films* **47**(3), 1977, pp. 219–233.
- [60] Y. D. Fan, X. P. Li, J. Yang, and J. P. Li. “Microscopic Model for Columnar Growth of Thin Films”. *Physica Status Solidi (a)* **134**(1), 1992, pp. 157–166.

- [61] L. Abelmann and C. Lodder. “Oblique evaporation and surface diffusion”. *Thin Solid Films* **305**(1-2), 1997, pp. 1–21.
- [62] K. Robbie and M. J. Brett. “Sculptured thin films and glancing angle deposition: Growth mechanics and applications”. *Journal of Vacuum Science & Technology A: Vacuum, Surfaces, and Films* **15**(3), 1997, pp. 1460–1465.
- [63] T. Karabacak, C. R. Picu, J. J. Senkevich, G.-C. Wang, and T.-M. Lu. “Stress reduction in tungsten films using nanostructured compliant layers”. *Journal of Applied Physics* **96**(10), 2004, p. 5740.
- [64] M. Jensen and M. Brett. “Porosity engineering in glancing angle deposition thin films”. *Applied Physics A* **80**(4), 2005, pp. 763–768.
- [65] S. R. Kennedy and M. J. Brett. “Porous broadband antireflection coating by glancing angle deposition.” *Applied optics* **42**(22), 2003, pp. 4573–9.
- [66] K. Sobahan, Y. J. Park, J. J. Kim, and C. K. Hwangbo. “Nanostructured porous SiO₂ films for antireflection coatings”. *Optics Communications* **284**(3), 2011, pp. 873–876.
- [67] A. C. van Popta, M. M. Hawkeye, J. C. Sit, and M. J. Brett. “Gradient-index narrow-bandpass filter fabricated with glancing-angle deposition.” *Optics letters* **29**(21), 2004, pp. 2545–7.
- [68] M. M. Hawkeye and M. J. Brett. “Narrow bandpass optical filters fabricated with one-dimensionally periodic inhomogeneous thin films”. *Journal of Applied Physics* **100**(4), 2006, p. 044322.

- [69] M. Summers, K. Tabunshchyk, A. Kovalenko, and M. J. Brett. “Fabrication of 2D-3D photonic crystal heterostructures by glancing angle deposition”. *Photonics and Nanostructures - Fundamentals and Applications* **7**(2), 2009, pp. 76–84.
- [70] M. M. Hawkeye and M. J. Brett. “Optimized Colorimetric Photonic-Crystal Humidity Sensor Fabricated Using Glancing Angle Deposition”. *Advanced Functional Materials* **21**, 2011, pp. 3652–3658.
- [71] Y. J. Liu, J. Shi, F. Zhang, H. Liang, J. Xu, A. Lakhtakia, S. J. Fonash, and T. J. Huang. “High-speed optical humidity sensors based on chiral sculptured thin films”. *Sensors and Actuators B: Chemical* **156**(2), 2011, pp. 593–598.
- [72] G. Kiema, M. Colgan, and M. J. Brett. “Dye sensitized solar cells incorporating obliquely deposited titanium oxide layers”. *Solar Energy Materials and Solar Cells* **85**(3), 2005, pp. 321–331.
- [73] Z. Xie, B. Henry, K. Kirov, H. Smith, A. Barkhouse, C. Grovenor, H. Assender, G. Briggs, G. Webster, and P. Burn. “Study of the effect of changing the microstructure of titania layers on composite solar cell performance”. *Thin Solid Films* **511-512**, 2006, pp. 523–528.
- [74] D. a. Rider, R. T. Tucker, B. J. Worfolk, K. M. Krause, A. Lalany, M. J. Brett, J. M. Buriak, and K. D. Harris. “Indium tin oxide nanopillar electrodes in polymer/fullerene solar cells.” *Nanotechnology* **22**(8), 2011, p. 085706.
- [75] K. Harris, D. Vick, E. Gonzalez, T. Smy, K. Robbie, and M. Brett. “Porous thin films for thermal barrier coatings”. *Surface and Coatings Technology* **138**(2-3), 2001, pp. 185–191.

- [76] J. J. Steele, G. a. Fitzpatrick, and M. J. Brett. “Capacitive Humidity Sensors With High Sensitivity and Subsecond Response Times”. *IEEE Sensors Journal* **7**(6), 2007, pp. 955–956.
- [77] M. Taschuk and J. Steele. “Performance and Modeling of a Nanostructured Relative Humidity Sensor”. *MRS Proceedings* **1054**, 2007, pp. 29–33.
- [78] Y.-J. Jen, M.-J. Lin, and J.-H. Chao. “Single dielectric columnar thin film as a humidity sensor”. *Sensors and Actuators B: Chemical* **149**(1), 2010, pp. 67–70.
- [79] S. R. Jim, a. J. Oko, M. T. Taschuk, and M. J. Brett. “Morphological modification of nanostructured ultrathin-layer chromatography stationary phases.” *Journal of chromatography. A* **1218**(40), 2011, pp. 7203–10.
- [80] J. Chen, J. Abell, Y.-w. Huang, and Y. Zhao. “On-chip ultra-thin layer chromatography and surface enhanced Raman spectroscopy.” *Lab on a chip* **12**(17), 2012, pp. 3096–102.
- [81] W. Water and S.-E. Chen. “Using ZnO nanorods to enhance sensitivity of liquid sensor”. *Sensors and Actuators B: Chemical* **136**(2), 2009, pp. 371–375.
- [82] M. Newton. “Experimental study of Love wave devices with thick guiding layers”. *Sensors and Actuators A: Physical* **109**(3), 2004, pp. 180–185.
- [83] A. C. Turton, D. Bhattacharyya, and D. Wood. “High sensitivity Love-mode liquid density sensors”. *Sensors and Actuators A: Physical* **123-124**(December 2004), 2005, pp. 267–273.

- [84] E. Gizeli, a. C. Stevenson, N. J. Goddard, and C. R. Lowe. “A novel Love-plate acoustic sensor utilizing polymer overlayers.” *IEEE transactions on ultrasonics, ferroelectrics, and frequency control* **39**(5), 1992, pp. 657–9.
- [85] J. Du, G. Harding, J. Ogilvy, P. Dencher, and M. Lake. “A study of Love-wave acoustic sensors”. *Sensors and Actuators A: Physical* **56**(3), 1996, pp. 211–219.
- [86] S. Franssila. *Introduction to Microfabrication*. John Wiley & Sons, 2010.
- [87] T. R. Hsu. *MEMS and microsystems: design and manufacture*. Mechanical engineering series. McGraw-Hill, 2002.
- [88] F. Herrmann, M. Weihnacht, and S. Buttgenbach. “Properties of sensors based on shear-horizontal surface acoustic waves in LiTaO₃/SiO₂ and quartz/SiO₂ structures”. *IEEE Transactions on Ultrasonics, Ferroelectrics and Frequency Control* **48**(1), 2001, pp. 268–273.
- [89] S. Onclin, B. J. Ravoo, and D. N. Reinhoudt. “Engineering silicon oxide surfaces using self-assembled monolayers.” *Angewandte Chemie (International ed. in English)* **44**(39), 2005, pp. 6282–304.
- [90] N. Crivillers, M. Mas-Torrent, S. Perruchas, N. Roques, J. Vidal-Gancedo, J. Veciana, C. Rovira, L. Basabe-Desmonts, B. J. Ravoo, M. Crego-Calama, and D. N. Reinhoudt. “Self-assembled monolayers of a multifunctional organic radical.” *Angewandte Chemie (International ed. in English)* **46**(13), 2007, pp. 2215–9.
- [91] A. C. Stevenson, E. Gizeli, N. J. Goddard, and C. R. Lowe. “Acoustic Love plate sensors: a theoretical model for the optimization of the

- surface mass sensitivity”. *Sensors and Actuators B: Chemical* **14**(1-3), 1993, pp. 635–637.
- [92] D. Vick, T. Smy, and M. J. Brett. “Growth behavior of evaporated porous thin films”. *Journal of Materials Research* **17**(11), 2002, pp. 2904–2911.
- [93] B. Dick, M. J. Brett, and T. Smy. “Investigation of substrate rotation at glancing incidence on thin-film morphology”. *Journal of Vacuum Science & Technology B: Microelectronics and Nanometer Structures* **21**(6), 2003, p. 2569.
- [94] K. M. Krause, M. T. Taschuk, K. D. Harris, D. a. Rider, N. G. Wakefield, J. C. Sit, J. M. Buriak, M. Thommes, and M. J. Brett. “Surface area characterization of obliquely deposited metal oxide nanostructured thin films.” *Langmuir : the ACS journal of surfaces and colloids* **26**(6), 2010, pp. 4368–76.
- [95] J. K. Kwan and J. C. Sit. “High sensitivity Love-wave humidity sensors using glancing angle deposited thin films”. *Sensors and Actuators B: Chemical* **173**, 2012, pp. 164–168.
- [96] P. Bruno, G. Cicala, F. Corsi, a. Dragone, and a.M. Losacco. “High relative humidity range sensor based on polymer-coated STW resonant device”. *Sensors and Actuators B: Chemical* **100**(1-2), 2004, pp. 126–130.
- [97] M. Penza and G. Cassano. “Relative humidity sensing by PVA-coated dual resonator SAW oscillator”. *Sensors and Actuators B: Chemical* **68**(1-3), 2000, pp. 300–306.

- [98] A. Buvailo, Y. Xing, J. Hines, and E. Borguet. “Thin polymer film based rapid surface acoustic wave humidity sensors”. *Sensors and Actuators B: Chemical* **156**(1), 2011, pp. 444–449.
- [99] T.-T. Wu, Y.-Y. Chen, and T.-H. Chou. “A high sensitivity nanomaterial based SAW humidity sensor”. *Journal of Physics D: Applied Physics* **41**(8), 2008, p. 085101.
- [100] Y. Chen and H. Kao. “Humidity sensors made on polyvinyl-alcohol film coated SAW devices”. *Electronics Letters* **42**(16), 2006, p. 948.
- [101] M. Penza, P. Aversa, G. Cassano, W. Wlodarski, and K. Kalantarzadeh. “Layered SAW gas sensor with single-walled carbon nanotube-based nanocomposite coating”. *Sensors and Actuators B: Chemical* **127**(1), 2007, pp. 168–178.
- [102] C. Viespe and C. Grigoriu. “Surface acoustic wave sensors with carbon nanotubes and SiO₂/Si nanoparticles based nanocomposites for VOC detection”. *Sensors and Actuators B: Chemical* **147**(1), 2010, pp. 43–47.
- [103] I. Sayago, M. Fernández, J. Fontecha, M. Horrillo, C. Vera, I. Obieta, and I. Bustero. “Surface acoustic wave gas sensors based on polyisobutylene and carbon nanotube composites”. *Sensors and Actuators B: Chemical* **156**(1), 2011, pp. 1–5.
- [104] E. Gizeli. “Sensitivity of the acoustic waveguide biosensor to protein binding as a function of the waveguide properties”. *Biosensors and Bioelectronics* **18**(11), 2003, pp. 1399–1406.

- [105] J. Andrä, A. Böhling, T. M. a. Gronewold, U. Schlecht, M. Perpeet, and T. Gutschmann. “Surface acoustic wave biosensor as a tool to study the interaction of antimicrobial peptides with phospholipid and lipopolysaccharide model membranes.” *Langmuir : the ACS journal of surfaces and colloids* **24**(16), 2008, pp. 9148–53.
- [106] D. H. Dinh, bibinitperiod Pascal, L. Vellutini, B. Bennetau, D. Rebière, C. Dejous, D. Moynet, C. Belin, and J.-P. Pillot. “Novel optimized biofunctional surfaces for Love mode surface acoustic wave based immunosensors”. *Sensors and Actuators B: Chemical* **146**(1), 2010, pp. 289–296.
- [107] Y. Li, P. Li, M. Yang, S. Lei, Y. Chen, and X. Guo. “A surface acoustic wave humidity sensor based on electrosprayed silicon-containing polyelectrolyte”. *Sensors and Actuators B: Chemical* **145**(1), 2010, pp. 516–520.
- [108] R. Rimeika, D. Čiplys, V. Poderys, R. Rotomskis, and M. Shur. “Fast-response surface acoustic wave humidity sensor based on hematoporphyrin film”. *Sensors and Actuators B: Chemical* **137**(2), 2009, pp. 592–596.
- [109] C. Caliendo, G. Contini, I. Fratoddi, S. Irrera, P. Pertici, G. Scavia, and M. V. Russo. “Nanostructured organometallic polymer and palladium/polymer hybrid: surface investigation and sensitivity to relative humidity and hydrogen in surface acoustic wave sensors”. *Nanotechnology* **18**(12), 2007, p. 125504.
- [110] Y. Liu, C. Wang, and Y. Li. “BCB film based SAW humidity sensor”. *Electronics Letters* **47**(18), 2011, p. 1012.

- [111] H.-S. Hong and G.-S. Chung. “Humidity sensing characteristics of Ga-doped zinc oxide film grown on a polycrystalline AlN thin film based on a surface acoustic wave”. *Sensors and Actuators B: Chemical* **150**(2), 2010, pp. 681–685.
- [112] A. Sadek, W. Wlodarski, Y. Li, W. Yu, X. Li, X. Yu, and K. Kalantarzadeh. “A ZnO nanorod based layered ZnO/64Å° YX LiNbO3 SAW hydrogen gas sensor”. *Thin Solid Films* **515**(24), 2007, pp. 8705–8708.
- [113] Y.-S. Huang, Y.-Y. Chen, and T.-T. Wu. “A passive wireless hydrogen surface acoustic wave sensor based on Pt-coated ZnO nanorods.” *Nanotechnology* **21**(9), 2010, p. 095503.
- [114] R. Arsat, X. Yu, Y. Li, W. Wlodarski, and K. Kalantar-zadeh. “Hydrogen gas sensor based on highly ordered polyaniline nanofibers”. *Sensors and Actuators B: Chemical* **137**(2), 2009, pp. 529–532.
- [115] X. Yu, Y. Li, and K. Kalantarzadeh. “Synthesis and electrochemical properties of template-based polyaniline nanowires and template-free nanofibril arrays: Two potential nanostructures for gas sensors”. *Sensors and Actuators B: Chemical* **136**(1), 2009, pp. 1–7.
- [116] S. Tsoi, E. Fok, J. C. Sit, and J. G. C. Veinot. “Surface Functionalization of Porous Nanostructured Metal Oxide Thin Films Fabricated by Glancing Angle Deposition”. *Chemistry of Materials* **18**(22), 2006, pp. 5260–5266.
- [117] F. Josse, F. Bender, and R. W. Cernosek. “A love-wave gas sensor coated with functionalized polysiloxane for sensing organophosphorus compounds”. *Sensors and Actuators B: Chemical* **76**(1-3), 2001, pp. 86–94.

- [118] J. J. Steele, A. C. van Popta, M. M. Hawkeye, J. C. Sit, and M. J. Brett. “Nanostructured gradient index optical filter for high-speed humidity sensing”. *Sensors and Actuators B: Chemical* **120**(1), 2006, pp. 213–219.
- [119] J. Steele. “Nanostructured thin films for humidity sensing”. PhD thesis. University of Alberta, 2007, p. 191.
- [120] M. Weiss, W. Welsch, and M. Schickfus. “Viscoelastic behavior of antibody films on a shear horizontal acoustic surface wave sensor”. *Analytical* **70**(14), 1998, pp. 2881–2887.
- [121] G. Zhang. “Nanostructure-Enhanced Surface Acoustic Waves Biosensor and Its Computational Modeling”. *Journal of Sensors* **2009**, 2009, pp. 1–11.
- [122] K. S. W. Sing. “Reporting physisorption data for gas/solid systems with special reference to the determination of surface area and porosity (Recommendations 1984)”. *Pure and Applied Chemistry* **57**(4), 1985, pp. 603–619.
- [123] G. McHale, M. I. Newton, and F. Martin. “Theoretical mass sensitivity of Love wave and layer guided acoustic plate mode sensors”. *Journal of Applied Physics* **91**(12), 2002, p. 9701.
- [124] J. K. Kwan and J. C. Sit. “The use of ion-milling to control clustering of nanostructured, columnar thin films.” *Nanotechnology* **21**(29), 2010, p. 295301.
- [125] H.-Y. Yang, M.-F. Lee, C.-H. Huang, Y.-S. Lo, Y.-J. Chen, and M.-S. Wong. “Glancing angle deposited titania films for dye-sensitized solar cells”. *Thin Solid Films* **518**(5), 2009, pp. 1590–1594.

- [126] G. K. Kiema, M. J. Colgan, and M. J. Brett. “Dye sensitized solar cells incorporating obliquely deposited titanium oxide layers”. *Solar Energy Materials and Solar Cells* **85**(3), 2005, pp. 321–331.
- [127] G. K. Kannarpady, R. Sharma, B. Liu, S. Trigwell, C. Ryerson, and A. S. Biris. “Silane decorated metallic nanorods for hydrophobic applications”. *Applied Surface Science* **256**(6), 2010, pp. 1679–1682.
- [128] A. Yu, Z. Liang, J. Cho, and F. Caruso. “Nanostructured Electrochemical Sensor Based on Dense Gold Nanoparticle Films”. *Nano Letters* **3**(9), 2003, pp. 1203–1207.
- [129] J. R. Siqueira, L. Caseli, F. N. Crespilho, V. Zucolotto, and O. N. Oliveira. “Immobilization of biomolecules on nanostructured films for biosensing.” *Biosensors & bioelectronics* **25**(6), 2010, pp. 1254–63.
- [130] J. F. Fernandez-Sanchez, T. Nezel, R. Steiger, and U. E. Spichiger-Keller. “Novel optical NO₂-selective sensor based on phthalocyaninato-iron(II) incorporated into a nanostructured matrix”. *Sensors and Actuators B: Chemical* **113**(2), 2006, pp. 630–638.
- [131] J.-G. Fan and Y.-P. Zhao. “Characterization of watermarks formed in nano-carpet effect.” *Langmuir : the ACS journal of surfaces and colloids* **22**(8), 2006, pp. 3662–71.
- [132] Y.-P. Zhao and J.-G. Fan. “Clusters of bundled nanorods in nanocarpet effect”. *Applied Physics Letters* **88**(10), 2006, p. 103123.
- [133] E. B. Corrochano. *Geometric Computing for Perception Action Systems: Concepts, Algorithms, and Scientific Applications*. Springer, 2001.

- [134] M. Seul, L. O’Gorman, and M. J. Sammon. *Practical Algorithms for Image Analysis with CD-ROM: Description, Examples, and Code*. Practical Algorithms for Image Analysis: Description, Examples, and Code. Cambridge University Press, 2000.
- [135] C. Buzea, G. Beydaghyan, C. Elliott, and K. Robbie. “Control of power law scaling in the growth of silicon nanocolumn pseudo-regular arrays deposited by glancing angle deposition”. *Nanotechnology* **16**(10), 2005, pp. 1986–1992.
- [136] L. Netzer and J. Sagiv. “A new approach to construction of artificial monolayer assemblies”. *Journal of the American Chemical Society* **105**(3), 1983, pp. 674–676.
- [137] A. T. Almeida, M. C. Salvadori, and D. F. S. Petri. “Enolase Adsorption onto Hydrophobic and Hydrophilic Solid Substrates”. *Langmuir* **18**(18), 2002, pp. 6914–6920.
- [138] M. Tanigawa and T. Okada. “Atomic force microscopy of supercoiled DNA structure on mica”. *Analytica Chimica Acta* **365**(1-3), 1998, pp. 19–25.
- [139] W. Ashurst, C. Carraro, and R. Maboudian. “Vapor phase anti-stiction coatings for MEMS”. *IEEE Transactions on Device and Materials Reliability* **3**(4), 2003, pp. 173–178.
- [140] A. Ulman. *An Introduction to Ultrathin Organic Films: From Langmuir-Blodgett to Self-Assembly*. Academic Press, 1991.
- [141] M. Wang, K. M. Liechti, Q. Wang, and J. M. White. “Self-assembled silane monolayers: fabrication with nanoscale uniformity.” *Langmuir : the ACS journal of surfaces and colloids* **21**(5), 2005, pp. 1848–57.

- [142] K. C. Grabar, R. G. Freeman, M. B. Hommer, and M. J. Natan. “Preparation and Characterization of Au Colloid Monolayers”. *Analytical Chemistry* **67**(4), 1995, pp. 735–743.
- [143] Y. Y. Xu, C. Bian, S. Chen, and S. Xia. “A microelectronic technology based amperometric immunosensor for α -fetoprotein using mixed self-assembled monolayers and gold nanoparticles”. *Analytica Chimica Acta* **561**(1-2), 2006, pp. 48–54.
- [144] B. Ballarin, M. C. Cassani, E. Scavetta, and D. Tonelli. “Self-assembled gold nanoparticles modified ITO electrodes: The monolayer binder molecule effect”. *Electrochimica Acta* **53**(27), 2008, pp. 8034–8044.
- [145] F. Xie, M. S. Baker, and E. M. Goldys. “Enhanced Fluorescence Detection on Homogeneous Gold Colloid Self-Assembled Monolayer Substrates”. *Chemistry of Materials* **20**(5), 2008, pp. 1788–1797.
- [146] J. R. Banerjee and F. W. Williams. “Exact Bernoulli-Euler static stiffness matrix for a range of tapered beam-columns”. *International Journal for Numerical Methods in Engineering* **23**(9), 1986, pp. 1615–1628.
- [147] K. K. Mon. “Elastic properties of inverted frustums”. *Journal of Applied Physics* **100**(7), 2006, p. 074311.
- [148] T. Karabacak, J. Singh, Y.-P. Zhao, G.-C. Wang, and T.-M. Lu. “Scaling during shadowing growth of isolated nanocolumns”. *Physical Review B* **68**(12), 2003, pp. 1–5.
- [149] M. T. Taschuk, K. M. Krause, J. J. Steele, M. A. Summers, and M. J. Brett. “Growth scaling of metal oxide columnar thin films deposited by glancing angle depositions”. *Journal of Vacuum Science & Technology B: Microelectronics and Nanometer Structures* **27**(5), 2009, p. 2106.

- [150] P. A. Kralchevsky and K. Nagayama. “Capillary interactions between particles bound to interfaces, liquid films and biomembranes.” *Advances in colloid and interface science* **85**(2-3), 2000, pp. 145–92.
- [151] O. Milton. *Materials Science of Thin Films*. Second. San Diego, CA: Academic Press, 2002.
- [152] R. N. Wenzel. “Resistance of solid surfaces to wetting by water”. *Industrial & Engineering Chemistry* **28**(8), 1936, pp. 988–994.
- [153] J. J. Steele, M. T. Taschuk, and M. J. Brett. “Nanostructured Metal Oxide Thin Films for Humidity Sensors”. *IEEE Sensors Journal* **8**(8), 2008, pp. 1422–1429.
- [154] D. Chandra and S. Yang. “Capillary-force-induced clustering of micropillar arrays: is it caused by isolated capillary bridges or by the lateral capillary meniscus interaction force?” *Langmuir : the ACS journal of surfaces and colloids* **25**(18), 2009, pp. 10430–4.
- [155] J. J. Cuomo, S. M. Rosnagel, and H. R. Kaufman. *Handbook of Ion Beam Processing Technology*. Westwood, NJ: Noyes Publications, 1989.
- [156] J. K. Kwan and J. C. Sit. “Acoustic wave liquid sensors enhanced with glancing angle-deposited thin films”. *Sensors and Actuators B: Chemical* **181**, 2013, pp. 715–719.
- [157] W. Water and Y. Yang. “The influence of calcium doped ZnO films on Love wave sensor characteristics”. *Sensors and Actuators A: Physical* **127**(2), 2006, pp. 360–365.
- [158] W. Water, S.-E. Chen, T.-H. Meen, and L.-W. Ji. “ZnO thin film with nanorod arrays applied to fluid sensor.” *Ultrasonics* **52**(6), 2012, pp. 747–52.

- [159] F.-C. Huang, Y.-Y. Chen, and T.-T. Wu. “A room temperature surface acoustic wave hydrogen sensor with Pt coated ZnO nanorods.” *Nanotechnology* **20**(6), 2009, p. 65501.
- [160] P. D. W. M. Haynes, P. D. David R. Lide, and P. D. Thomas J. Bruno. *CRC Handbook of Chemistry and Physics 2012-2013*. CRC Handbook of Chemistry & Physics. Taylor & Francis Group, 2012.
- [161] S. Tsoi, E. Fok, J. C. Sit, and J. G. C. Veinot. “Superhydrophobic, high surface area, 3-D SiO₂ nanostructures through siloxane-based surface functionalization.” *Langmuir : the ACS journal of surfaces and colloids* **20**(24), 2004, pp. 10771–4.
- [162] H. Hao, K. Tang, P. Ku, J. Chao, C. Li, C. Yang, and D. Yao. “Development of a portable electronic nose based on chemical surface acoustic wave array with multiplexed oscillator and readout electronics”. *Sensors and Actuators B: Chemical* **146**(2), 2010, pp. 545–553.
- [163] D. Matatagui, J. Martí, M. Fernández, J. Fontecha, J. Gutiérrez, I. Gràcia, C. Cané, and M. Horrillo. “Chemical warfare agents simulants detection with an optimized SAW sensor array”. *Sensors and Actuators B: Chemical* **154**, 2010, pp. 199–205.
- [164] T. M. a. Gronewold, A. Baumgartner, A. Weckmann, J. Knekties, and C. Egler. “Selection process generating peptide aptamers and analysis of their binding to the TiO₂ surface of a surface acoustic wave sensor.” *Acta biomaterialia* **5**(2), 2009, pp. 794–800.
- [165] H. J. Lee, K. Namkoong, E. C. Cho, C. Ko, J. C. Park, and S. S. Lee. “Surface acoustic wave immunosensor for real-time detection of

hepatitis B surface antibodies in whole blood samples.” *Biosensors & bioelectronics* **24**(10), 2009, pp. 3120–5.